



STUDIA UNIVERSITATIS
BABEȘ-BOLYAI

Volume 65, No. 1 (2020)

Engineering



UNIVERSITATEA BABEȘ-BOLYAI

TRADIȚIE ȘI EXCELENȚĂ



STUDIA UNIVERSITATIS
BABEȘ-BOLYAI

www.studia.ubbcluj.ro

51 B.P. Hasdeu Street, 400371
Cluj-Napoca, ROMANIA

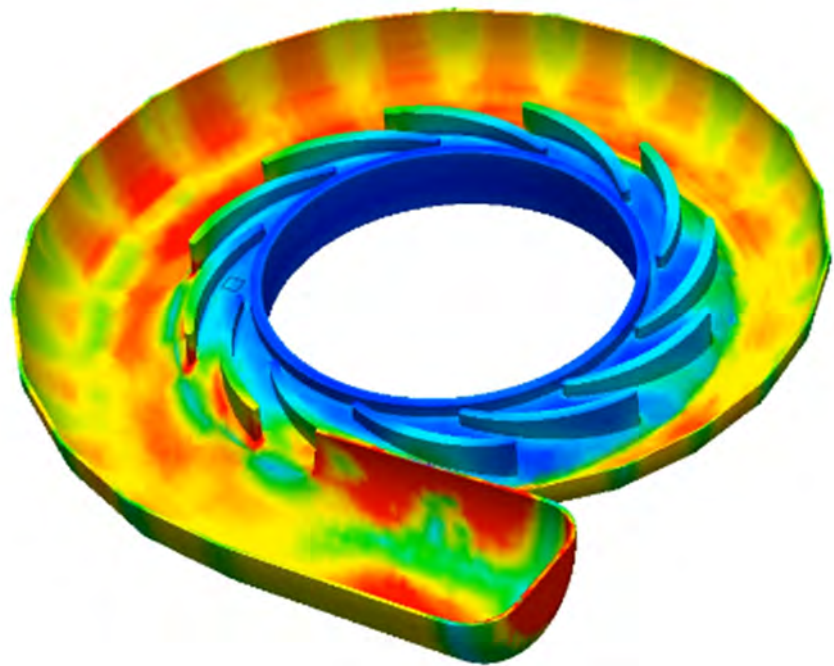


CLUJ UNIVERSITY PRESS

www.editura.ubbcluj.ro

ISSN: 2734-7680

ISSN-L: 2734-7680





STUDIA UNIVERSITATIS
BABEȘ-BOLYAI

Engineering

The Journal of the Faculty of Engineering at Reșița
Babeș-Bolyai University from Cluj-Napoca

Volume 65, No. 1, 2020

doi:10.24193/subbeng.2020.1

Published Online: 2020-11-23

ISSN:2734-7680

EDITORIAL OFFICE:

Piața Traian Vuia, Nr. 1-4, 320085, Reșița,
Caraș-Severin, România
http://studia.ubbcluj.ro/serii/engineering/index_en.html

EDITOR-IN-CHIEF:

Nicoleta GILLICH

BBU University Center in Reșița – Romania
Faculty of Engineering
nicoleta.gillich@ubbcluj.ro

© Studia Universitatis Babeș-Bolyai, Babeș-Bolyai University
B.P. Hasdeu str. no. 51, 400371 Cluj-Napoca, Romania
Phone: +40-264-405300 *6452; Fax: +40-264-591906
e-mail: office@studia.ubbcluj.ro

EDITORIAL BOARD

EDITOR-IN-CHIEF:

Nicoleta GILLICH, BBU University Center in Reșița – Romania

ASSOCIATE EDITORS:

Codruta Oana HAMAT, BBU University Center in Reșița – Romania

Peter LORENZ, Hochschule für Technik und Wirtschaft des Saarlandes,
Saarbrücken – Germany

Azree Othuman MYDIN, Universiti Sains Malaysia, Penang – Malaysia

Dorian NEDELICU, BBU University Center in Reșița – Romania

Horațiu O. PILSAN, Fachhochschule Vorarlberg, Dornbirn – Austria

Laslo SIKOLYA, University College of Nyiregyhaza – Hungary

Ovidiu VASILE, Politehnica University, Bucharest – Romania

SCIENTIFIC COMITEE:

Tudor AMBROS, Technical University of Moldova, Chișinău – Moldova

Polidor BRATU, „Dunărea de Jos” University of Galați – Romania

Istvan BIRO, University of Szeged – Ungaria

Florin BREABĂN, Université d'Artois, IUT Bethune – Franța

Konstantin DIMITROV, Macedonian Center for Energy Efficiency Skopje –
Republic of Macedonia

Toma-Leonida DRAGOMIR, Politehnica University of Timișoara – România

Branislav DRAGOVIĆ, University of Montenegro, Kotor – Montenegro

Waleed Fekry FARIS, International Islamic University Malaysia, Kuala Lumpur – Malaysia

Gilbert-Rainer GILLICH, BBU University Center in Reșița – Romania

Michel F. KHOURI, The Lebanese University, El-Maten – Lebanon

Zoltan-Iosif KORKA, BBU University Center in Reșița – Romania

Siniša KUZMANOVIĆ, University of Novi Sad – Serbia

Tiberiu-Ștefan MĂNESCU, BBU University Center in Reșița – Romania

Horățiu O. PILSAN, Fachhochschule Vorarlberg, Dornbirn – Austria

Sorin VLASE, Transilvania University of Brașov – Romania

Nenad ZRNIĆ, University of Belgrad – Serbia

Table of content

Olga-Ioana Amariei, Codruța-Oana Hamat

Simulation of a waiting system 9

Lenuța Cîndea, Vasile Iancu

Research on the quality of welded joints of P265GH heat-resistant steel pipes for electron beam mechanized welding 21

Cornel Hațiegan, Mihaela Dorica Stroia, Cristian Muscai

Simulating an improved algorithm for propagation of transverse oscillations through a string 29

Draghița Ianici, Sava Ianici

Contributions to the synthesis and modeling of gear wheels geometry of a double harmonic transmission 37

Sava Ianici, Draghița Ianici

Study of the influence of intermittent motion on the orientation kinematic precision of a double harmonic transmission 45

Sava Ianici, Draghița Ianici

The study of the elastic deformation of a flexible wheel by a cam wave generator 51

Hope Iyawe

Sacredness to desecration: ‘Languaging’ and ‘othering’ of peoples and places through dumping of domestic waste in Uroora, Benin City, Nigeria 59

Hope Iyawe, Obas John Ebohon

Opportunities to tackle apathy in solid waste management in rural integrated urban environment: The case of the Uroora community in Benin City, Nigeria 69

Gaurav Kumar, S.M.K. Rizvi, Amresh Kumar

Heat absorption and hall current effects on unsteady MHD flow past an inclined plate 79

Tatian-Cristian Mălin, Dorian Nedelcu,

Gilbert-Rainer Gillich

A Python application to generate digital signals 96

Tiberiu Ștefan Mănescu, Nicușor Laurențiu Zaharia,

Constantin Ioan Barbința

Static and dynamic tests at a railway tank wagon 105

Andrea Amalia Minda, David Lupu,

Gilbert-Rainer Gillich

Improvement of Jain’s algorithm for frequency estimation 115

Mihaela Molnar, Eugen Răduca

Study for monitoring of the insulation stator winding of the hydro generators using a data acquisition system 123

Cristian-Mircea Muscai, Ion-Cornel Mituletu,

Tiberiu Manescu, Liviu-Bogdan Protea

Three-Axis Level with WiFi Connection 129

Marius-Vasile Pop, Gilbert-Rainer Gillich,

Cristian Tufisi, Zeno-Iosif Praisach, Lucian Păun

Estimation of the severity of damage produced by a transverse crack 137

Marius-Vasile Pop, Zeno-Iosif Praisach,

Gilbert-Rainer Gillich, Lucian Păun

Deflection of a beam with a transverse crack under dead load 145

Marius Florian Preduț, Elisabeta Spunei, Monica Roșu

Prediction of power cables failures using a software application 153

Eugen Răduca, Mihaela Molnar,

Nicolae Titu Fara

Model of microprocessor centrifugal equipment for honey extraction 163

Elisabeta Spunei, Ion Piroi, Florina Piroi

Technical performance analysis of a 40 kW photovoltaic installation **171**

Mihaela Dorica Stroia, Cornel Hațiegan,

Cristinel Popescu

Virtual instrument designed for data acquisition **179**

Simulation of a waiting system

Olga-Ioana Amariei, Codruța-Oana Hamat

This paper analyzes an existing production system in an industrial hall, consisting of 11 machines (service stations) and 13 intermediate stocks (queues), where 4 types of parts are processed and assembled, with the aim of increasing production volume. The Queuing System Simulation module of the WinQSB software is used, which allows the simulation of waiting systems.

Keywords: *queues, serving stations, average processing time, average waiting time, average stationary time, standard deviation*

1. Introduction

Probability theory and mathematical statistics are inevitable in the analysis of simple or complex waiting systems, because there are constantly situations of uncertainty both in terms of time of arrival and duration of services [2].

Waiting, forming a "waiting line" or a "queue" is a common phenomenon in the activity of an organization [9].

The design of a "waiting" model implies the knowledge of some characteristics of the studied phenomenon regarding the average number of: units in the system, of the units about to be served, of units in the queue, of unoccupied stations, of units arriving in a given time as well as the average time: serving, waiting in the system and waiting in a line [8].

The basic process in models for waiting phenomena consists of units generated over time by an input source, which require to be served by one or more serving stations. Units that cannot be served immediately will form waiting lines or queues. The most commonly used serving discipline is FIFO (first come, first served) [1].

2. Illustrative example

The production system (fig.2) required to be analyzed consists of 11 machines (serving stations or servers) on which 4 types of parts are processed and assembled (R1 ÷ R4).

Part R1 is processed on machines M1 and M5, and part R2 on machines M2 and M6, then a piece of each part type is assembled on machine M8 (Subassembly 1). Parts R3 and R4 are processed on machines M3 and M4, and then a piece of each part is assembled on machine M7 (Subassembly 2). On the M9 machine, the two subassemblies are assembled, which are then processed on the M10 and M11 machines, both machines being identical.

If a machine from the first six (M1 ÷ M6) is occupied, the parts wait for the release of that machine in the container corresponding to that machine, the so-called queues (intermediate stocks) between different jobs. There are also queues after the machines where the subassemblies are made and the assembly, more precisely, the M7, M8 and M9 machines. In the case of M10 and M11 machines, processing is carried out on any of them which are available.

It is considered that all parts are processed and assembled according to the FIFO serving discipline, and the storage space for the parts to be processed and assembled is limited and therefore the maximum capacity for each queue, which is equal to 200, is specified.

The duration of the time intervals between two consecutive arrivals of parts R1 to machine M1 is a uniformly distributed probabilistic quantity between 0.5 and 0.6 hours. The duration of the time intervals between two consecutive arrivals of parts R2 to the machine M2 is a probabilistic quantity with normal distribution with an average of 0.6 hours and the standard deviation 0.2 hours. The duration of the time intervals between two consecutive arrivals of parts R3 at machine M3 is a uniformly distributed probabilistic quantity between 0.5 and 0.6 hours. The duration of the time intervals between two consecutive arrivals of parts R4 to the machine M4 is a probabilistic quantity with normal distribution with an average of 0.6 hours and the standard deviation 0.2 hours.

The machining time on the M1 machine is a probabilistic quantity with normal distribution with an average of 0.6 hours/part and the standard deviation 0.04 hours/part, for the M2 machine it is a probabilistic quantity with a normal distribution with an average of 0.4 hours/part and standard deviation 0.03 hour/part, for the M3 machine is a probabilistic size with normal distribution with an average of 0.3 hours/part and standard deviation 0.02 hours/part, for the M4 machine is a probabilistic size with normal distribution with an average of 0.5 hours/part and standard deviation 0.05 hours part, for the M5 machine is a probabilistic quantity with normal distribution with an average of 0.3 hours/part and the standard deviation 0.02 hours/part and for the M6 machine is a

probabilistic quantity with normal distribution averaging 0.25 hours/part and standard deviation 0.02 hours/part. The assembly time on M7 for subassembly 1 is a constant of 0.7 hours, for subassembly 2 (machine M8) is a constant of 0.8 hours, and for the assembly (machine M9) is 0.2 hours. Finally, the assembly is processed on M10 and M11 machines, and the processing time is a probabilistic quantity with normal distribution, with an average of 0.3 hours/part and the standard deviation 0.02 hours/part. The transfer time of subassembly 1 from machine M7 to queue 11 and that of subassembly 2 from machine M8 to queue 12 is 0.03 hours, and that of assembly from M9 to queue 13 is 0.02 hours.

Component Name	Type (C/S/Q)	Immediate Endless (Queue / Transfer time, argument) (h)	Input Rate	Queue Discipline	Queue Capacity	Interarrival Time Distribution	Service Time Distribution
H1	C		Queue1			Uniform/0.5/0.5	
H2	C		Queue2			Normal/0.8/0.2	
H3	C		Queue4			Uniform/0.5/0.6	
H4	C		Queue5			Normal/0.6/0.2	
Machine1	S		Queue5				R1/Normal/0.6/0.04
Machine2	S		Queue5				R2/Normal/0.4/0.03
Machine3	S		Queue7				R3/Normal/0.3/0.02
Machine4	S		Queue8				R4/Normal/0.5/0.05
Machine5	S		Queue9				R1/Normal/0.3/0.02
Machine6	S		Queue10				R2/Normal/0.25/0.02
Machine7	S	Queue11/0.70	Assembly				R3/Constant/0.2/R4/Constant/0.7
Machine8	S	Queue12/0.80	Assembly				R1/Constant/0.8/R2/Constant/0.8
Machine9	S	Queue13/0.80	Assembly				R1/Constant/0.2/R2/Constant/0.2/R3/Constant/0.3/R4/Constant/0.2
Machine10	S						Normal/0.3/0.02/R2/Normal/0.3/0.02/R3/Normal/0.3/0.02/R4/Normal/0.3/0.02
Machine11	S						Normal/0.3/0.02/R2/Normal/0.3/0.02/R3/Normal/0.3/0.02/R4/Normal/0.3/0.02
Queue1	Q		Machine1	FIFO	200		
Queue2	Q		Machine2	FIFO	200		
Queue3	Q		Machine3	FIFO	200		
Queue4	Q		Machine4	FIFO	200		
Queue5	Q		Machine5	FIFO	200		
Queue6	Q		Machine6	FIFO	200		
Queue7	Q		Machine7	FIFO	200		
Queue8	Q		Machine7	FIFO	200		
Queue9	Q		Machine8	FIFO	200		
Queue10	Q		Machine8	FIFO	200		
Queue11	Q		Machine9	FIFO	200		
Queue12	Q		Machine9	FIFO	200		
Queue13	Q		Machine10, Machine11	FIFO	200		

Figure 1. Input data of the problem

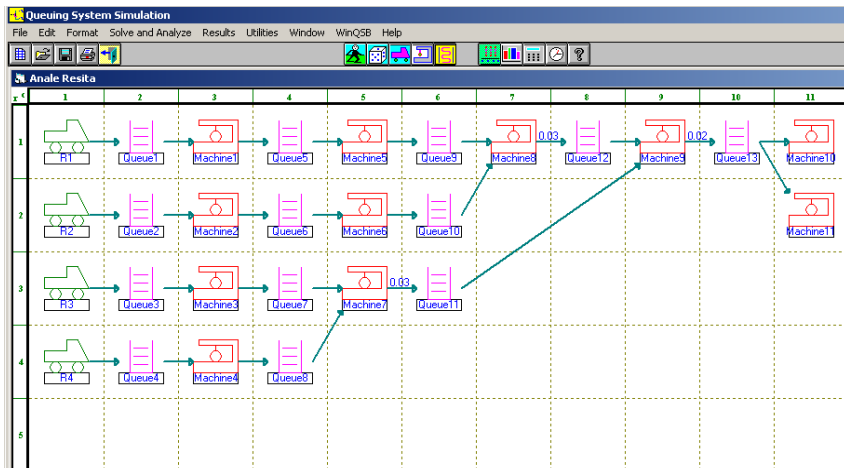


Figure 2. Graphic representation of the production system

After entering the problem data (fig.1) the simulation of 100 hours is specified. The results are collected starting with the 20th hour of operation, in order to remove the influence of the initial conditions, when the intermediate stocks are zero [2],[5].

2.1. Solving the problem

The program provides results for three types of analysis: analysis of customers who have entered the system (fig.3), analysis of the use of service stations (fig.4) and queue analysis (fig.5).

3-10-202	Result	R1	R2	R3	R4	Overall
1	Total Number of Arrival	146	134	146	134	560
2	Total Number of Balking	0	0	0	0	0
3	Average Number in the System (L)	36.7813	27.3391	35.1105	12.2735	111.5043
4	Maximum Number in the System	60	43	58	24	185
5	Current Number in the System	60	42	58	23	183
6	Number Finished	100	0	0	0	100
7	Average Process Time	4.3316	0	0	0	4.3316
8	Std. Dev. of Process Time	0.0766	0	0	0	0.0766
9	Average Waiting Time (Wq)	56.5872	0	0	0	56.5872
10	Std. Dev. of Waiting Time	23.4452	0	0	0	23.4452
11	Average Transfer Time	0	0	0	0	0
12	Std. Dev. of Transfer Time	0	0	0	0	0
13	Average Flow Time (W)	20.1584	0	0	0	20.1584
14	Std. Dev. of Flow Time	7.3957	0	0	0	7.3957
15	Maximum Flow Time	32.9214	0	0	0	32.9214
	Data Collection: 20 to	100 hours				
	CPU Seconds =	22.7500				

Figure 3. Show Customer Analysis. Current situation

After simulating the 100 hours, it is found that during the 80 hours taken into account, 146 parts R1 and R3 enter the system, and also 134 parts R2 and R4. On average per hour there are 36.78 R1 parts in the system; 27.34 - R2; 35.11 - R3 and 12.27 - R4. The total number of products obtained by processing and assembly is 100 finished products.

The average processing time of a finished product is 4.3316 hours, with a standard deviation of 0.0766 hours. The average waiting time for a finished product is 56.5872 hours, with a standard deviation of 23.4452 hours. The average time spent in the system by a finished product is 20.1584 hours, with a standard deviation of 7.3957 hours, and the total time spent in the system by a finished product is 32.9214 hours.

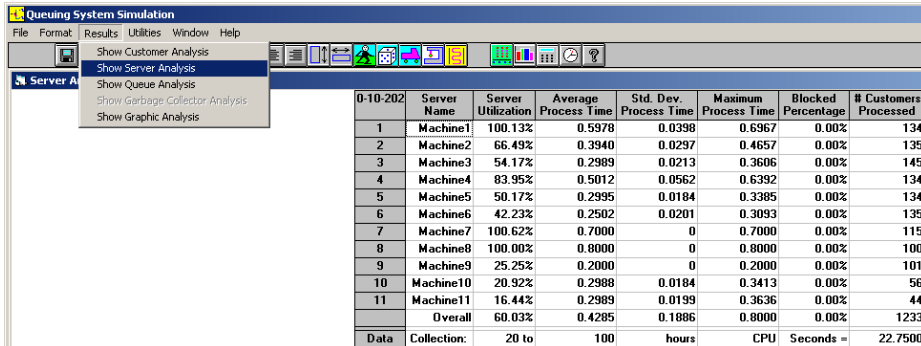


Figure 4. Show Server Analysis. Current situation

From the analysis related to the use of machines (fig.4) it is observed that the M10 and M11 machines have the lowest degree of loading, namely: 20.92% and 16.44%, and the number of products processed on each of these two machines is of 56 and 44 pieces. In this case, the solution would be to remove the M11 machine, which would increase the load of the M10 machine.

Also in the table with the analysis of service stations a load of over 100% can be observed on the M1 and M7 machines, machines that can be considered “narrow place”. This can be remedied by supplementing with another machine of each type.

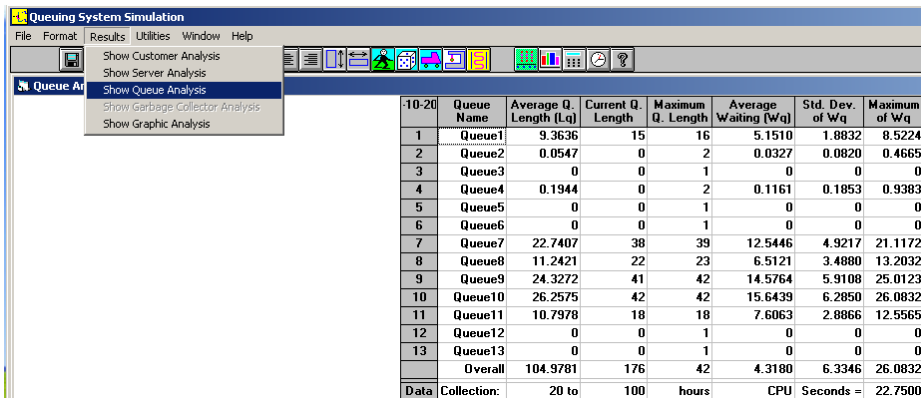


Figure 5. Show Queue Analysis. Current situation

From the analysis of intermediate stocks (fig.5) it can be seen that queue 10 has the longest average length, of 26.2575 products, as well as the longest average waiting time of 15.6439 hours. Queue 10 consists of parts R2 waiting to be assembled with parts R1 on the machine M8. The possible causes of the wait are: either the machine M8 is fully occupied, or in queue 9 there are no parts R1 to be

assembled with the parts R2 on the machine M8. The Show Server Analysis table shows that the M8 machine has a load rate of 100%, so this is the cause of the wait in the system and not the one related to queue 9, which has the second largest average length equal to 24.3272 products. To fix the problem, another M8 machine will be introduced into the system.

Following the three analyzes performed, three solutions are proposed:

1. disposal of the M11 machine;
2. additional M1 and M7 machines;
3. supplementing the M8 machine.

2.2. Supplementation with service stations

The production system is supplemented with three more machines (M1b, M7b and M8b) and we obtain the three analyzes presented in the section 2.1. (fig. 6, 7 and 8).

10-11-2020	Result	R1	R2	R3	R4	Overall
1	Total Number of Arrival	145	133	145	133	556
2	Total Number of Balking	0	0	0	0	0
3	Average Number in the System [L]	14.4917	1.1616	14.8868	0.9167	31.4568
4	Maximum Number in the System	21	3	21	3	48
5	Current Number in the System	20	1	21	1	43
6	Number Finished	133	0	0	0	133
7	Average Process Time	4.3435	0	0	0	4.3435
8	Std. Dev. of Process Time	0.0785	0	0	0	0.0785
9	Average Waiting Time [Wq]	13.1894	0	0	0	13.1894
10	Std. Dev. of Waiting Time	4.3592	0	0	0	4.3592
11	Average Transfer Time	0	0	0	0	0
12	Std. Dev. of Transfer Time	0	0	0	0	0
13	Average Flow Time [W]	8.7134	0	0	0	8.7134
14	Std. Dev. of Flow Time	2.2582	0	0	0	2.2582
15	Maximum Flow Time	11.8860	0	0	0	11.8860
	Data Collection: 20 to	100 hours				
	CPU Seconds =	23.9220				

Figure 6. Show Customer Analysis. Modified system 1

10-11-2020	Server Name	Server Utilization	Average Process Time	Std. Dev. Process Time	Maximum Process Time	Blocked Percentage	# Customers Processed
1	Machine1a	54.60%	0.5983	0.0383	0.7106	0.00%	73
2	Machine1b	53.64%	0.5960	0.0442	0.7311	0.00%	72
3	Machine2	66.89%	0.4024	0.0311	0.4835	0.00%	133
4	Machine3	54.63%	0.2994	0.0203	0.3368	0.00%	146
5	Machine4	82.25%	0.4947	0.0506	0.6223	0.00%	133
6	Machine5	53.87%	0.2993	0.0212	0.3414	0.00%	144
7	Machine6	41.53%	0.2517	0.0209	0.3112	0.00%	132
8	Machine7a	56.87%	0.7000	0.0003	0.7000	0.00%	65
9	Machine7b	58.62%	0.7000	0.0001	0.7000	0.00%	67
10	Machine8a	69.00%	0.8000	0	0.8000	0.00%	69
11	Machine8b	63.00%	0.8000	0	0.8000	0.00%	63
12	Machine9	33.00%	0.2000	0.0002	0.2000	0.00%	132
13	Machine10	30.47%	0.3010	0.0192	0.3593	0.00%	81
14	Machine11	19.20%	0.2954	0.0211	0.3359	0.00%	52
	Overall	52.68%	0.4332	0.1950	0.8000	0.00%	1362
Data	Collection:	20 to	100	hours	CPU	Seconds =	23.9220

Figure 7. Show Server Analysis. Modified system 1

Following the three analyzes made on the new production system, the following conclusions can be drawn:

- the number of finished products obtained increased by 33 pieces;
- on average, there are fewer parts of each type per hour and also the maximum number of parts decreased from 60 to 21 for part R1, from 43 to 3 for part R2, 58 to 21 for the R3 part and 24 to 3 for the R4 part,
- the total time spent by a finished product decreased from 32.9214 hours to 11.886 hours;
- the average time spent on a finished product decreased from 20.1854 hours to 8.7134 hours;
- the loading of the machines is not very good, especially for the M11 machine, being 19.20%, which again leads to the elimination of the M11 machine (the first solution proposed in section 2.1)

10-11-2020	Queue Name	Average Q. Length (Lq)	Current Q. Length	Maximum Q. Length	Average Waiting (Wq)	Std. Dev. of Wq	Maximum of Wq
1	Queue1	0	0	1	0	0	0
2	Queue2	0.0748	0	1	0.0450	0.0895	0.3932
3	Queue3	0	0	1	0	0	0
4	Queue4	0.0991	0	2	0.0596	0.0977	0.5852
5	Queue5	0	0	1	0	0	0
6	Queue6	0	0	1	0	0	0
7	Queue7	13.0546	19	20	7.2418	2.2249	10.3671
8	Queue8	0	0	1	0	0	0
9	Queue9	9.3878	15	17	5.2479	1.8171	8.9457
10	Queue10	0.0053	0	1	0.0032	0.0148	0.1077
11	Queue11	0.1331	0	2	0.0807	0.1765	0.7094
12	Queue12	1.3301	1	5	0.8093	0.9587	2.8988
13	Queue13	0	0	1	0	0	0
	Overall	24.0848	35	20	1.0157	2.3961	10.3671
Data	Collection:	20 to	100	hours	CPU	Seconds =	23.9220

Figure 8. Show Queue Analysis. Modified system 1

2.3. Removing a service station

One of the solutions proposed in section 2.1 was the elimination of the M11 machine, which was also reached following the analyzes performed in section 2.2. The results obtained are almost identical to those obtained in section 2.2. The only change appears in Show Server Analysis, where the M10 machine increased the loading degree from 30.47% to 49.68%, meaning it also took over the loading degree of the removed machine (fig.9).

10-11-2020	Server Name	Server Utilization	Average Process Time	Std. Dev. Process Time	Maximum Process Time	Blocked Percentage	# Customers Processed
1	Machine1a	54.60%	0.5983	0.0383	0.7106	0.00%	73
2	Machine1b	53.64%	0.5960	0.0442	0.7311	0.00%	72
3	Machine2	66.89%	0.4024	0.0311	0.4835	0.00%	133
4	Machine3	54.63%	0.2994	0.0203	0.3368	0.00%	146
5	Machine4	82.25%	0.4947	0.0506	0.6223	0.00%	133
6	Machine5	53.87%	0.2993	0.0212	0.3414	0.00%	144
7	Machine6	41.53%	0.2517	0.0209	0.3112	0.00%	132
8	Machine7a	56.87%	0.7000	0.0003	0.7000	0.00%	65
9	Machine7b	58.62%	0.7000	0.0001	0.7000	0.00%	67
10	Machine8a	69.00%	0.8000	0	0.8000	0.00%	69
11	Machine8b	63.00%	0.8000	0	0.8000	0.00%	63
12	Machine9	33.00%	0.2000	0.0002	0.2000	0.00%	132
13	Machine10	49.68%	0.2988	0.0201	0.3593	0.00%	133
	Overall	56.74%	0.4332	0.1950	0.8000	0.00%	1362
Data	Collection:	20 to	100	hours	CPU	Seconds =	24.0160

Figure 9. Show Server Analysis. Modified system 2

A comparative graphical representation of the average and maximum processing times on the 13 machines is illustrated in Figure 10.

Server Performance

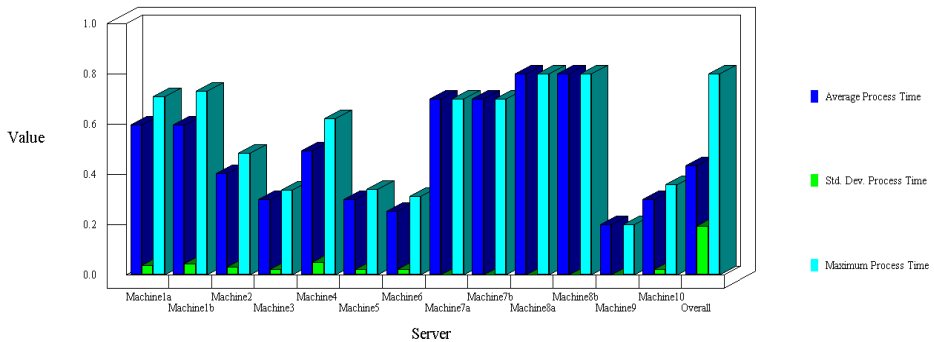


Figure 10. Graphical representation of the average and maximum processing times. Modified system 2

2.4. Removal of an additional service station

In section 2.2, the production system was supplemented with three machines, namely: M1b, M7b and M8b. Following the Show Server Analysis performed in section 2.1, the M1 machine was considered a “narrow place”, just like the M7 machine, although due to the fact that the number of products processed on the M1 machine is 134, identical to that of the other machines, it would not have been appropriate to supplement with another machine in this case.

10-11-2020	Result	R1	R2	R3	R4	Overall
1	Total Number of Arrival	146	129	146	145	566
2	Total Number of Balking	0	0	0	0	0
3	Average Number in the System (L)	14.1330	1.5430	13.2576	1.8888	30.8225
4	Maximum Number in the System	23	4	23	5	55
5	Current Number in the System	22	1	21	0	44
6	Number Finished	131	0	0	0	131
7	Average Process Time	4.3515	0	0	0	4.3515
8	Std. Dev. of Process Time	0.0821	0	0	0	0.0821
9	Average Waiting Time (Wq)	12.6417	0	0	0	12.6417
10	Std. Dev. of Waiting Time	4.5193	0	0	0	4.5193
11	Average Transfer Time	0	0	0	0	0
12	Std. Dev. of Transfer Time	0	0	0	0	0
13	Average Flow Time (W)	8.0077	0	0	0	8.0077
14	Std. Dev. of Flow Time	2.5197	0	0	0	2.5197
15	Maximum Flow Time	12.5426	0	0	0	12.5426
	Data Collection: 20 to	100 hours				
	CPU Seconds =	24.4380				

Figure 11. Show Customer Analysis. Modified system 3

10-11-2020	Server Name	Server Utilization	Average Process Time	Std. Dev. Process Time	Maximum Process Time	Blocked Percentage	# Customers Processed
1	Machine1	99.70%	0.5997	0.0404	0.7225	0.00%	133
2	Machine2	64.79%	0.3987	0.0336	0.4818	0.00%	130
3	Machine3	54.23%	0.2971	0.0181	0.3553	0.00%	146
4	Machine4	91.43%	0.5010	0.0484	0.6363	0.00%	146
5	Machine5	50.28%	0.3002	0.0191	0.3428	0.00%	134
6	Machine6	40.44%	0.2508	0.0166	0.2821	0.00%	129
7	Machine7a	63.97%	0.7000	0	0.7000	0.00%	73
8	Machine7b	63.00%	0.7000	0	0.7000	0.00%	72
9	Machine8a	68.00%	0.8000	0	0.8000	0.00%	68
10	Machine8b	63.00%	0.8000	0	0.8000	0.00%	63
11	Machine9	32.50%	0.2000	0.0002	0.2000	0.00%	130
12	Machine10	49.38%	0.3016	0.0203	0.3656	0.00%	131
	Overall	61.72%	0.4373	0.1960	0.8000	0.00%	1355
Data	Collection:	20 to	100	hours	CPU	Seconds =	24.4380

Figure 12. Show Server Analysis. Modified system 3

In this section the machine M1b is eliminated and the results are obtained, shown in figures 11, 12 and 13.

10-11-2020	Queue Name	Average Q. Length (Lq)	Current Q. Length	Maximum Q. Length	Average Waiting (Wq)	Std. Dev. of Wq	Maximum of Wq
1	Queue1	9.4093	16	16	5.1892	1.9953	8.3575
2	Queue2	0.0275	0	1	0.0170	0.0441	0.2329
3	Queue3	0	0	1	0	0	0
4	Queue4	0.9055	0	4	0.4996	0.5041	1.6847
5	Queue5	0	0	1	0	0	0
6	Queue6	0	0	1	0	0	0
7	Queue7	2.5076	5	6	1.3699	1.0190	2.9940
8	Queue8	0.0738	0	2	0.0404	0.1125	0.5614
9	Queue9	1.0720	3	4	0.6403	0.6987	2.1803
10	Queue10	0.4677	0	3	0.2948	0.3731	1.2650
11	Queue11	8.9183	14	16	5.0259	2.7902	8.9297
12	Queue12	0.0252	0	1	0.0154	0.0672	0.4968
13	Queue13	0.0000	0	1	0.0000	0.0003	0.0035
	Overall	23.4068	38	16	0.9952	2.0415	8.9297
Data	Collection:	20 to	100	hours	CPU	Seconds =	24.4380

Figure 13. Show Queue Analysis. Modified system 3

A comparative graphic image of the average and maximum processing times on the 12 machines is presented in fig.14. Also, in fig.15 are represented graphically the average and maximum values of the intermediate stocks, respectively of the average and maximum lengths of the queues in the system.

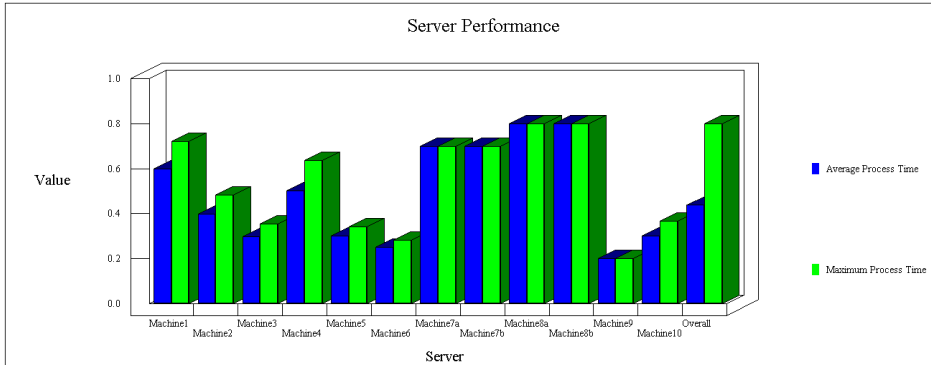


Figure 14. Graphical representation of average and maximum processing times. Modified system 3

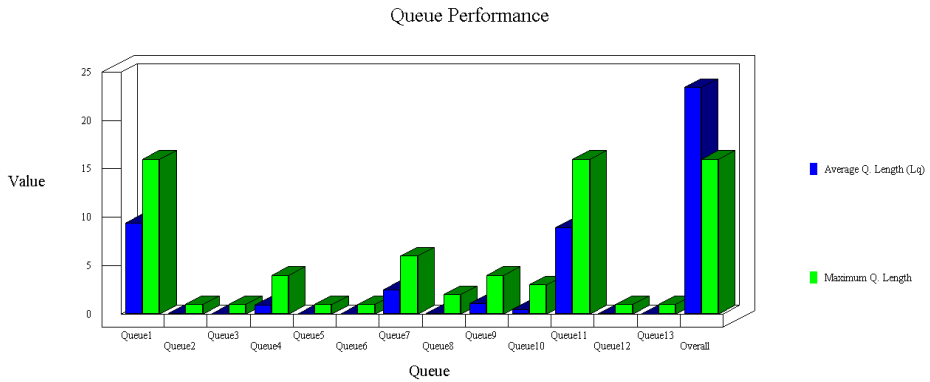


Figure 15. Graphical representation of average and maximum Q lengths. Modified system 3

In the table with comparative results in Figure 16, with the elimination of the M1b machine, the total number of finished products decreased from 133 to 131.

	The current system	Modified system 1	Modified system 2	Modified system 3
Show Customer Analysis				
Number Finished	100	133	133	131
Average Process Time	4.3316	4.3435	4.3435	4.3515
Average Waiting Time	56.5872	13.1894	13.1894	12.6417
Average Flow Time	20.1584	8.7134	8.7134	8.0077
Show Server Analysis				
M1a-Server Utilization/Customers Processed	100.13/134	54.6/73	54.6/73	99.7/133
M1b-Server Utilization/Customers Processed	-	53.64/72	53.64/72	-
M2-Server Utilization/Customers Processed	66.49/135	66.89/133	66.89/133	64.79/130
M3-Server Utilization/Customers Processed	54.17/145	54.63/146	54.63/146	54.23/146
M4-Server Utilization/Customers Processed	83.95/134	82.25/133	82.25/133	91.43/146
M5-Server Utilization/Customers Processed	50.17/134	53.87/144	53.87/144	50.28/134
M6-Server Utilization/Customers Processed	42.23/135	41.53/132	41.53/132	40.44/129
M7a-Server Utilization/Customers Processed	100.62/115	56.87/65	56.87/65	63.87/73
M7b-Server Utilization/Customers Processed	-	58.62/67	58.62/67	63/72
M8a-Server Utilization/Customers Processed	100/100	69/69	69/69	68/68
M8b-Server Utilization/Customers Processed	-	63/63	63/63	63/63
M9-Server Utilization/Customers Processed	25.25/101	33/132	33/132	32.5/130
M10-Server Utilization/Customers Processed	20.92/56	30.47/81	49.68/133	49.38/131
M11-Server Utilization/Customers Processed	16.44/44	19.2/52	-	-

Figure 16. Comparative results

3. Conclusion

The waiting theory shows us that the average time spent by a consumer in the system consists of the average time spent in the queue and the time needed to serve. In this case, where the consumer in the waiting system is a finished product, the average time spent in the system is obtained by following the path taken by the part to achieve the finished product.

In the present paper we started from a production system consisting of 11 machines (servers), on which 100 finished products were processed and assembled. Following the supplementation of the system with 3 machines, it was observed that as the loading degree of the machines decreases (server utilization coefficient), the average downtime of the finished products in the system decreases, as well as the average waiting time and the number of finished products increases. But this decrease in the degree of loading of the machines also led to the situation where most of the queues are non-existent, in which case no intermediate stocks are needed due to the processing times of the parts or not enough parts enter the system.

References

- [1] Amariei O.I., *Contribuții privind modelarea, simularea și optimizarea fluxurilor de producție utilizând programe dedicate*, Editura Politehnica Timișoara, 2014.
- [2] Amariei O.I., *Aplicații ale programului WinQSB în simularea sistemelor de producție*, Editura Eftimie Murgu, Reșița, 2009.
- [3] Amariei O.I., Dumitrescu D.C., Fourmaux D., Analysis and Behaviour Understanding of a Production System, *Analele Universitatii „Eftimie Murgu“ Resita, Fascicula de Inginerie*, 16(1), 2009, pp. 21-28.
- [4] Amariei O.I., Frunzăverde D., Popovici Gh., Hamat C.O., WinQSB simulation software—a tool for professional development, *Procedia-Social and Behavioral Sciences*, 1(1), 2009, pp. 2786-2790.
- [5] Blăjină, O.A., *Decizii optime în management cu WinQSB 2.0, Vol.1*, Editura Albastră, Cluj-Napoca, 2011.
- [6] Gorunescu F., Prodan A., *Modelare stohastică și simulare*, Editura Albastră, Cluj-Napoca, 2001.
- [7] Kikolsk M., Study of Production Scenarios with the Use of Simulation Models, *7th International Conference on Engineering, Project, and Production Management*, Procedia Engineering 182, 2017, 321 – 328.
- [8] Rațiu-Suciu C., Luban F., Hîncu D., Ciocoiu N., *Modelare economică*. Ediția a doua, Editura ASE București, 2009.
- [9] Rațiu-Suciu C., *Modelarea & simularea proceselor economice. Teorie și practică*. Ediția a treia, Editura Economică, 2003.

Addresses:

- Lect. Dr. Eng. Olga-Ioana Amariei, Babeș-Bolyai University, Faculty of Engineering, Piața Traian Vuia, nr. 1-4, 320085, Reșița, o.amariei@uem.ro
- Prof. Dr. Eng. Codruța-Oana Hamat, Babeș-Bolyai University, Faculty of Engineering, Piața Traian Vuia, nr. 1-4, 320085, Reșița, c.hamat@uem.ro
(* corresponding author)

Research on the quality of welded joints of P265GH heat-resistant steel pipes at electron beam mechanized welding

Lenuța Cîndea, Vasile Iancu*

This paper analyzes the quality of welded joints of high temperature resistant steel pipe at electron beam welding, knowing that the mechanical properties of these types of steels are influenced by the interaction of different processes specific to physical and mechanical metallurgy. Analyzing the values of the local hardening estimator ΔHV_{10} calculated between the characteristic areas of welded joints, it is observed that it has a decreasing tendency at thermally de-stressed joints, in all areas of the welded joints, especially in the welded seam.

Keywords: pipes, heat-resistant steel, quality, creeping strength.

1. Introduction

These steels must ensure high temperature resistance characteristics (creep), respectively ductility, especially elongation and necking, at high values, stable during the use of the metal structure [1]. In this sense, it is necessary to optimize the relationship between microstructure, microscopic deformation and macroscopic creep behaviour [2], [3].

An important mechanical characteristic is the strength of the steel, considered to be the property of the structure to oppose certain displacements of dislocations due to the applied stresses. Thus, the strength of the steel depends on the type and number of obstacles that hinder the displacement of the dislocations through the matrix [4].

These obstacles can consist of dislocation networks, loops of marginal dislocations, individual atoms and agglomerations of atoms, precipitates, cavities etc.

Under specific conditions, the strength of steel can be controlled or at least influenced by some of these obstacles, depending on the chemical composition and microstructure of the steel [5], [6], [7].

2. Experimental program

In the experimental program on mechanized electron beam welding of P265GH non-alloy heat-resistant steel pipes, the samples F1 and F1T were made of P265GH heat-resistant steel pipes, Φ 60.3 x 6.0 mm, 75 mm in length.

Following the preliminary experiments ($U_a = 60$ kV, $I_s = 25\text{...}30$ mA, $D_t = 130\text{...}150$ mm, $F_o = 700\text{...}750$ mA, $v_s = 40$ cm/min), the optimal parameters were established for the electron beam welding process (511), namely: welding current $I_s = 28$ mA, arc voltage $U_a = 60$ KV, firing distance $D_t = 150$ mm, focusing $F_o = 740$ mA, welding speed $v_s = 40$ cm / min.

After cooling, each electron beam welded butt sample was examined visually (with the naked eye and a 5X magnifying glass), the welded joints being of a suitable quality and without external defects [8], [9].

2.1. Post-welding heat treatment

The butt welded sample made of non-alloy heat-resistant steel type P265GH, Φ 60.3 x 6.0 mm (F1T) was subjected to a strain relief treatment according to Table 1. Figure 1 and Figure 2, show the visual aspects of the mechanized electron beam butt welded samples F1 and F1T. The joints did not show welding defects on the outer surfaces.



Figure 1. F1 butt welded sample, not heat treated.



Figure 2. F1T butt welded sample, heat treated.

Table 1. Stress relief treatment regimes parameters

Local stress-relief heat-treatment	Stress relief treatment regimes parameters							Steel type
	Temp min, [°C]	Temp max, [°C]	Rate of heating, [°C/h]	Rate of cooling, [°C/h]	Heating-up time, [h]	Holding time, [h]	Cooling time, [h]	
Welded sample heat treated	20	600	150	200	3,86	0,50	2,90	P265GH

2.2. Results of mechanical laboratory tests

a. The results of tensile tests on flat test pieces with calibrated area no. 1 and 2 taken from the mechanized welded buttocks with the F1 and F1T electron beam are centralized in Table 2. Figure 3 and Figure 4 show the specimens after the tensile tests.

Table 2. Results of tensile tests on flat specimens with the calibrated portion

Nr. sample	Nr. test	Test dimens. (S ₀ x B ₀), mm	F _{max} , N	R _m , N/mm ²	The place of rupture
F1	F1.1	5,9 x 12,1	34150	478	BM
	F1.2	5,9 x 12,0	32900	465	WELD
F1T	F1.1T	5,8 x 12,0	28600	411	WELD
	F1.2T	5,8 x 12,1	32300	460	WELD



Figure 3. Broken test piece F1



Figure 4. Broken test piece F1T

b. The macroscopic examination of the cross sections of the welded joints did not reveal macro cracks (Figure 5 and Figure 6) both on the welded samples without heat treatment and on those with heat treatment (TD1).

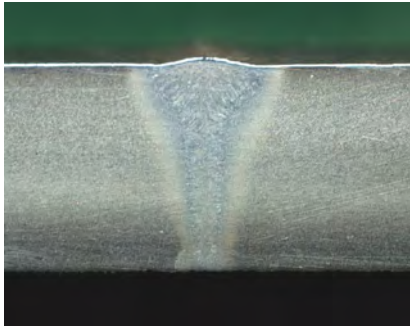


Figure 5. Sample F1, Nital 10%

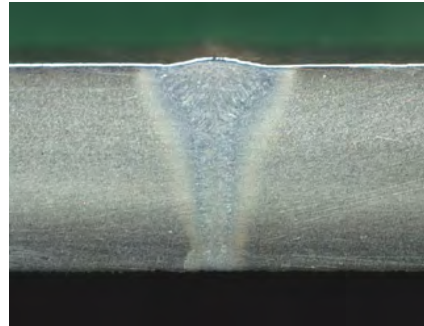


Figure 6. Sample FIT, Nital 10%

c. The microscopic examination revealed specific microstructures, namely: in the base material (BM_{right} and BM_{left}), ferrite-pearlite granular structures in rows, with alternating ferrite and pearlite bands, whose granulation is between scores 7-8, according to SR ISO 643: 2003 (Figure 7 and Figure 8).

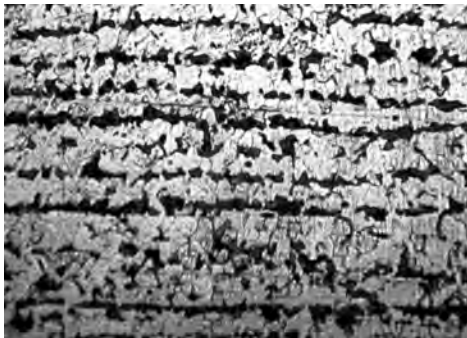


Figure 7. Sample F1, BM, Nital 2%,
100X



Figure 8. Sample FIT, BM, Nital 2%,
100X

In the WELD), pearlite-ferrite structures with inferior bainite and acicular ferrite, according to SR ISO 643: 2003 (Figure 9 and Figure 10).



Figure 9. Sample F1, WELD, Nital 2%, 100X



Figure 10. Sample F1T, WELD, Nital 2%, 100X

In thermally influenced areas (TIZ_{right} , TIZ_{left}), pearlite-ferrite granular structures with granulations point 4-5 and areas with acicular ferrite, according to SR ISO 643: 2003 (Figure 11 and Figure 12).

The presence of acicular ferrite is greatly diminished in the heat-treated sample (Figure 12) attesting that the structural modification of the lower bainite is beneficial to the welding of non-alloy steel in reducing its hardness.

The microscopically examined areas did not show micro cracks.



Figure 11. Sample F1, TIZ, Nital 2%, 100X

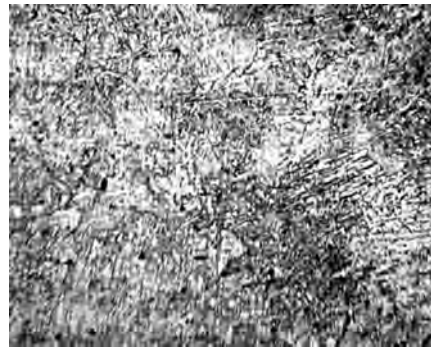


Figure 12. Sample F1T, TIZ, Nital 2%, 100X

d. The mechanical Vickers HV10 hardness tests on test specimens no. 3, taken from mechanized butt welded samples with electron beam F1 and F1T, were performed according to SR EN ISO 6507 - 1: 2006 and SR EN 1043 - 1: 1997 in the characteristic areas of the welded joints (BM_{left} , BM_{right} , TIZ_{left} , TIZ_{right} , WELD)

respecting the location of the hardness fingerprints. The experimentally determined Vickers HV10 hardness values are centralized in Table 3.

Table 3. Results of Vickers HV10 mechanical hardness tests

Point	Tried area	Sample F1	Sample F1T
1	BM _{left}	160	143
2		145	138
3	BM _{right}	162	141
4		144	150
5	TIZ _{left}	239	201
6		247	214
7		240	202
8	TIZ _{right}	263	228
9		233	225
10		241	238
11	WELD	325	251
12		326	247

Table 4 shows the values of the estimator $\Delta HV10$ calculated between the characteristic areas of the welded joints made by the welding procedure 511.

Table 4. Values of the $\Delta HV10$ estimator calculated between the characteristic areas of welded joints made by the welding process 111

Weld sample mark	Local hardening estimator $\Delta HV10$, %			
	WELD – TIZ _{left}	WELD – TIZ _{right}	TIZ _{rt} – BM _{lt}	TIZ _{lt} – BM _{rt}
F1	25,46	28,52	45,24	41,29
F1T	9,16	10,36	40,76	35,51

The variations of the maximum Vickers HV10 hardness on the characteristic areas of the welded joints made of non-alloy heat-resistant steel pipes type P265GH are shown in Figure 13.

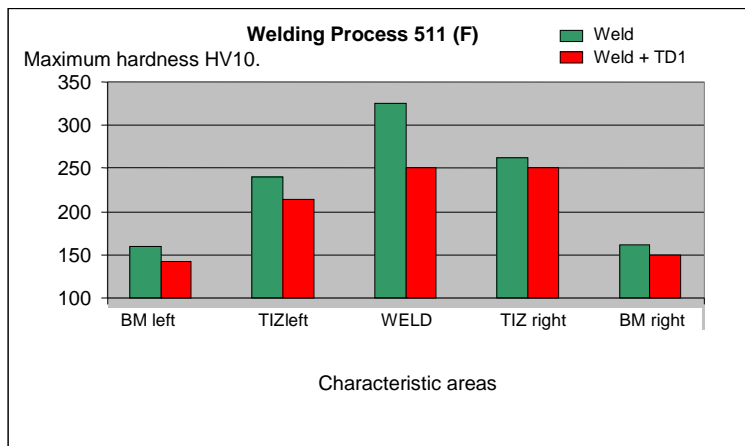


Figure 13. Variation $HV10_{max} = f(\text{Characteristic areas})$ at welded F1 și FIT joints made by the process 511.

Conclusion

Following the tensile tests at 20° C, the macroscopic and microscopic analyzes and the Vickers HV10 hardness tests, the following conclusions can be drawn on the specimens taken from the F1 and FIT welded samples made of non-alloy heat-resistant steel P265GH:

The joints did not show welding defects on the outer surfaces.

Analyzing the variation of tensile strengths, we observe that they are higher than the value 410 N/mm² imposed by the norm EN 10216: 2 + A2 - 2007 for the analyzed steel.

In addition, even if three specimens broke in the weld, the determined tensile strengths are above the lower limit of the required tensile strength range (410... 570 N / mm²) for the heat-resistant non-alloy steel.

The microscopically examined areas did not show micro cracks.

Maximum Vickers HV10 hardness's occur in the welds of welded joints (326 HV10 and 251 HV10), the application of thermal stress relief in the welded sample heat treated significantly reduces the hardness peaks of the characteristic areas and in the weld of the stressed area there is a decrease of Vickers HV10 hardness by 23.1% compared to undistensioned welding.

References

- [1] Voiculescu I., Rontescu C., Dondea L.I., *Metalografia îmbinărilor sudate*, Editura Sudura, Timișoara, 2010, pp. 11-20.

- [2] Adam W., Mischok W., Welnitz G., Zeshav M., Niederhoff K., *Experiența acumulată la sudarea oțelurilor CrMoVNb termorezistente cu 9 %Cr - Stadiul de dezvoltare a elaborării noilor generații de materiale termorezistente*, Conferința A.S.R. - 2004, Constanța, sept. 15 – 17, 2004, pp. 255 – 266.
- [3] Sammons M., *How to Cup Walk - An Interesting Pipe Welding Technique Provides Arc Stability and More Operator Comfort Than traditional GTA Methods*, Welding Journal, June 2005, pp. 42 - 43.
- [4] Martinec J., Plihal A., *Materiale de sudare adecvate lucrului la temperaturi înalte*, ESAB News, Nr. 1, 2007, pp. 6 – 7.
- [5] Pascu D.R., ș.a., *Cercetări experimentale pentru evaluarea degradării structurale a echipamentelor industriale ce lucrează la presiuni și temperaturi ridicate, folosind tehnica replicilor metalografice conform ISO 3057*, Raport de cercetare, 2005, ISIM Timișoara.
- [6] Luca R., *Method for the Measurement of the Temperature During the Stress Relieving Thermal treatment*, Sudura, Nr. 2, 2000, pp. 40 - 44.
- [7] Irimia I., *Considerații asupra sudabilității oțelurilor carbon și slab aliate, folosite în centralele electrice de termoficare - CET-uri*, Conferința Internațională ASR Realizări și perspective în fabricarea structurilor sudate pentru medii urbane, București, sept. 28 – 30, 2003, pp. 288 - 296.
- [8] Mateiu H.Șt., Fleșer T., *Experimental Researches for the Crack Propagation Under Creep of the Thermoresistant Steels*, Sudura, Nr. 4, 2002, pp. 11 - 16.
- [9] Pascu D.R., ș.a., *Cercetări experimentale pentru evaluarea degradării structurale a echipamentelor industriale ce lucrează la presiuni și temperaturi ridicate, folosind tehnica replicilor metalografice conform ISO 3057*, Raport de cercetare, 2005, ISIM Timișoara.

Addresses:

- Lect. Dr. Eng. Lenuța Cîndea, Babeș-Bolyai University, Faculty of Engineering, Piața Traian Vuia, nr. 1-4, 320085, Reșița, l.cindea@uem.ro
- Lect. Dr. Eng. Vasile Iancu, Babeș-Bolyai University, Faculty of Engineering, Piața Traian Vuia, nr. 1-4, 320085, Reșița, v.iancu@uem.ro.
(* *coresponding autor*)

Simulating an improved algorithm for propagation of transverse oscillations through a string.

Cornel Hațiegan, Mihaela Dorica Stroia*, Cristian Muscai

In present paper we bring under discussion a mathematical algorithm for determining oscillations through an elastic string. We have noticed that the algorithm has a flaw which can be solved by introducing an approximation into the system. For improved algorithm we have developed a program in order to obtain a simulator for propagation of transverse oscillations through a string, which allow us to obtain graphical representations for n-order harmonics.

Keywords: transverse oscillation, string, algorithm, simulator

1. Theoretical background

A perfectly elastic string has the ends fixed in two points located at the same level and at a distance L from each other. Strain F is applied at ends of string in order to keep it taut. Mass of length unit is $\mu = \rho \cdot S$, where ρ is material density and S is string cross-section. At the initial moment, the string is pulled out of the equilibrium state, displacements of points being expressed by a given function, $u(x,0) = f(x)$. At any later time, displacements are solutions of the equation [1,2]:

$$\frac{\partial^2 u}{\partial t^2} = c_t^2 \frac{\partial^2 u}{\partial x^2}, \quad 0 \leq x \leq L, \quad t > 0 \quad (1)$$

which describes the propagation of transverse oscillations along the elastic string with speed $c_t = \sqrt{\frac{F}{\mu}}$. Relation (1) is a differential equation with second order partial derivatives, with boundary conditions:

$$u(0,t) = 0, \quad u(L,t) = 0, \quad t \geq 0 \quad (2)$$

and initial conditions:

$$u(x,0) = f(x) , \quad \frac{\partial u}{\partial t} \Big|_{(x,0)} = 0, \quad 0 \leq x \leq L \quad (3)$$

which means that at time $t = 0$ the string is at rest, its initial shape being given by function $f(x)$, with $f(0) = f(L) = 0$. Solution of such an equation is given by d'Alembert's formula, used to graphically illustrate the phenomenon of transverse oscillations propagation and phase changes with π at reflection on fixed ends:

$$u(x,t) = \frac{1}{2} [f(x - c_t t) + f(x + c_t t)] \quad (4)$$

Using variable separation method, general solution of equation (1) can be easily deduced, under the established initial conditions and to the mentioned limits [3]:

$$u(x,t) = \sum_{n=1}^{\infty} u_n(x,t) = \sum_{n=1}^{\infty} a_n \cos \omega_n t \cdot \sin \frac{n\pi}{L} x , \quad 0 \leq x \leq L , \quad t > 0 \quad (5)$$

where $\omega_n = c_t \frac{n\pi}{L}$, $n = 1, 2, 3, \dots$ are pulsations of eigenmodes of string. As it can be noticed, propagation occurs in an infinite field, from known initial conditions, on an open border. If:

$$f(x) = u_n(x,0) = a_n \sin \frac{n\pi}{L} x , \quad n = 1, 2, 3, \dots \quad (6)$$

then stationary waves corresponding to the n -order harmonics can be highlighted, having nodes in points $x_m = \frac{n}{m} L$ and loops in points

$x_m = \frac{2m+1}{2n} L$, ($m = 1, 2, \dots, n-1$). All string points, except the ends and those located in nodes, will perform oscillating movements having amplitude given by envelope (6) and period of:

$$T_n = \frac{1}{n} \frac{2L}{c_t} = \frac{1}{n} T_1 , \quad n = 1, 2, 3, \dots \quad (7)$$

For numerical integration of (6) finite difference calculus can be used for rectangular type network nodes, step along the Ox axis being denoted by h , and the one along time axis by k . If, in resulted linear equation system, we introduce notation $r = c_t^2 \frac{k^2}{h^2}$, we obtain [3-5]:

$$\begin{aligned}
u_{i,j+1} &= r(u_{i-1,j} + u_{i+1,j}) + 2(1-r)u_{i,j} - u_{i,j-1} , \\
i &= 1, 2, 3, \dots, n_x - 1 \\
j &= 1, 2, 3, \dots
\end{aligned} \tag{8}$$

Of course, initial conditions, as well as discrete boundary conditions will change, values of displacements in nodes located on the line immediately above the axis $t = 0$ being determined taking into account the new initial conditions.

2. Improving and implementing algorithm

It can be shown that algorithm (8) leads to a stable solution only for $r \leq 1$. For $r = 1$ we obtain discrete form of solution (4), however, as r value decreases, solution precision decreases. Using for r values close to 1 implies relatively small step values on time axis because, in this situation, algorithm (8) gives unsatisfactory results for large values of time due to accumulation of method and rounding errors.

An improvement of the initial method can be obtained if we introduce the approximation [3-6]:

$$\frac{\partial^2 u}{\partial x^2} \Big|_{(i,j)} \cong \frac{1}{2} \left[\frac{\partial^2 u}{\partial x^2} \Big|_{(i,j+1)} + \frac{\partial^2 u}{\partial x^2} \Big|_{(i,j-1)} \right] \cong \frac{1}{2} \left[\frac{u_{i-1,j+1} - 2u_{i,j+1} + u_{i+1,j+1}}{h^2} + \frac{u_{i-1,j-1} - 2u_{i,j-1} + u_{i+1,j-1}}{h^2} \right] \tag{9}$$

The resulted algorithm is:

$$\begin{aligned}
-\frac{r}{2}u_{i-1,j+1} + (1+r)u_{i,j+1} - \frac{r}{2}u_{i+1,j+1} &= p_i , \\
i &= 1, 2, 3, \dots, n_x - 1 \\
j &= 1, 2, 3, \dots,
\end{aligned} \tag{10}$$

where:

$$p_i = \frac{2}{r}u_{i-1,j-1} - (1+r)u_{i,j-1} + \frac{r}{2}u_{i+1,j-1} + 2u_{i,j} , \quad i = 1, 2, 3, \dots, n_x - 1 \tag{11}$$

solution being stable for any r value greater or equal to 0.

For a given j , system of linear algebraic equations (10) has a tridiagonal matrix, which can easily be solved using the Gaussian elimination method. For evaluating the solution on a given line, results calculated on two previous lines are used. Case “ $j=0$ ” constitutes an exception to the rule.

The program developed for improved algorithm calculates and displays displacements $n_x = 200$ uniform points, for $n_t = 400$ successive time values. If the value set with the scroll bar is zero, the initial displacements are given by a

Gaussian function which ensures a maximum in the middle of the string and a width at half height of one sixth of the total length. For the other values, forming of stationary waves corresponding to the first six harmonics is studied.

Following code lines are used for determining r values:

```
n = Harmonic.Value
If n = 0 Then
    r = (2 * nx / nt) ^ 2 ' r value for Gaussian straining
Else
    r = (2 * nx / nt / n) ^ 2 ' r value for n harmonic
End If
```

After calculating r values we can determine elements of system matrix:

```
r1 = 1 + r
r2 = r / 2
For i = 1 To nx1
    a(i) = -r2 'non-diagonal elements of system matrix
    b(i) = r1 ' diagonal elements of system matrix
Next i
```

3. Tests and results

After compiling the program, we obtain the Main screen from figure 1. By pressing START button the program will calculate and generate a graphical representation of displacements in the string. There are also available “HELP” button, if there is need of information about program functioning, and “EXIT” button which interrupts program execution.

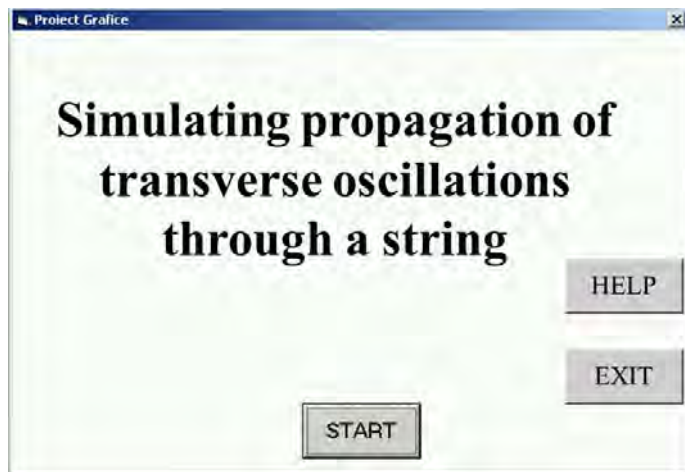


Figure 1. Program Main window

After pressing START button from figure 1 a new window will open, containing graphical representation which displays, as earlier mentioned, displacements in the string, as it can be noticed in figure 2. We again have a START button that allows us to simulate for different harmonic orders, specific number being introduced in the “Valoare” field as a number or by moving the progress bar visible on the right of window from figure 2.

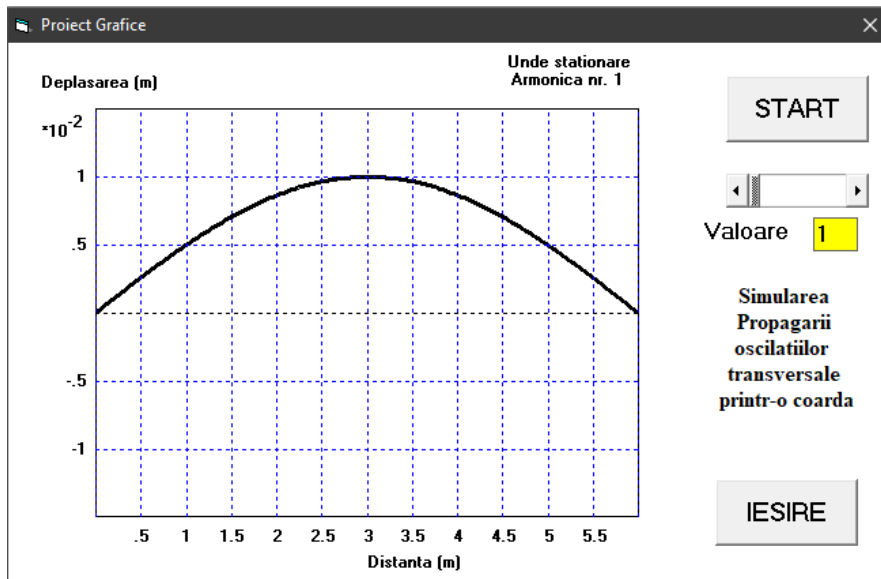


Figure 2. Graphical representation for first order harmonic

In cases corresponding to formation of stationary waves, individual oscillations of points on string can be observed.

For $n = 1$ we obtain the natural frequency, ν_1 , which corresponds to the natural vibration mode (fundamental harmonic), and for other values of n higher harmonics are obtained which are equal to an integer multiple of the natural frequency, as it results from figures 3 to 6.

The frequencies values for which the string vibrates in stationary state constitutes the discrete spectrum as eigenvalue of vibration, or resonances, of the string.

Further on, we present in figures 3 to 6 graphical representations of higher harmonics of 3, 5, 10 and 20 order, with the purpose in demonstrating program functionality. By means of simulator we build up, we can obtain graphical representation of n -order harmonics.

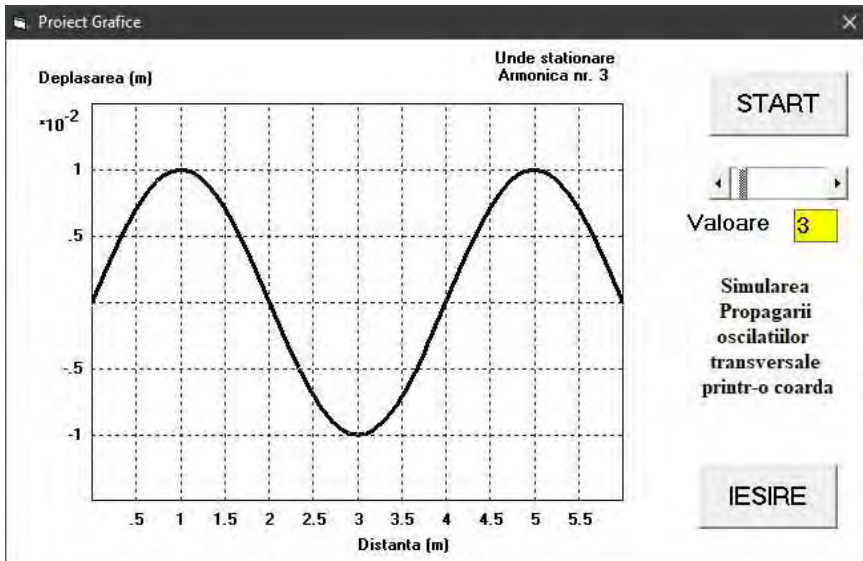


Figure 3. Graphical representation for third order harmonic

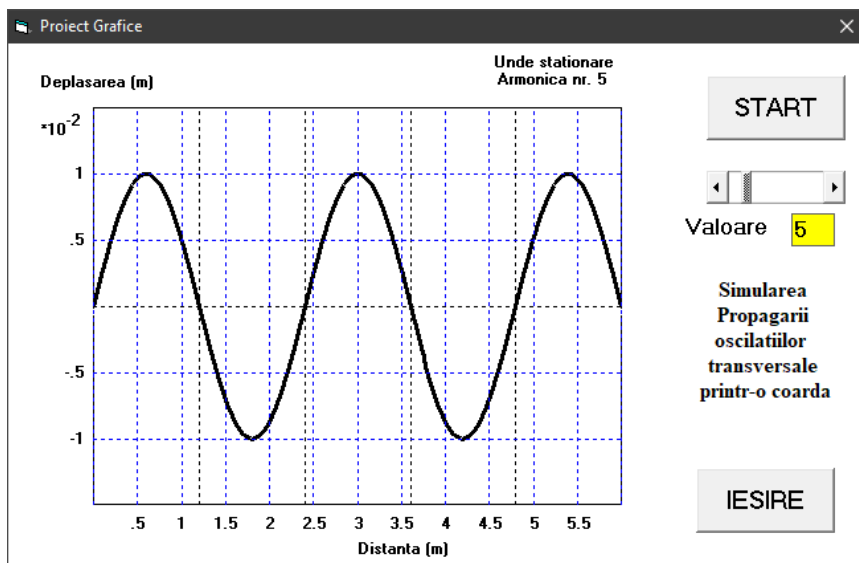


Figure 4. Graphical representation for fifth order harmonic

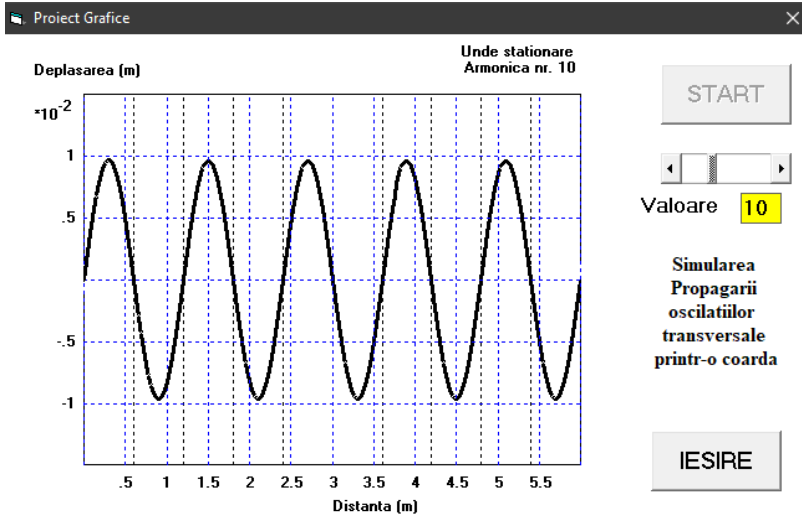


Figure 5. Graphical representation for tenth order harmonic

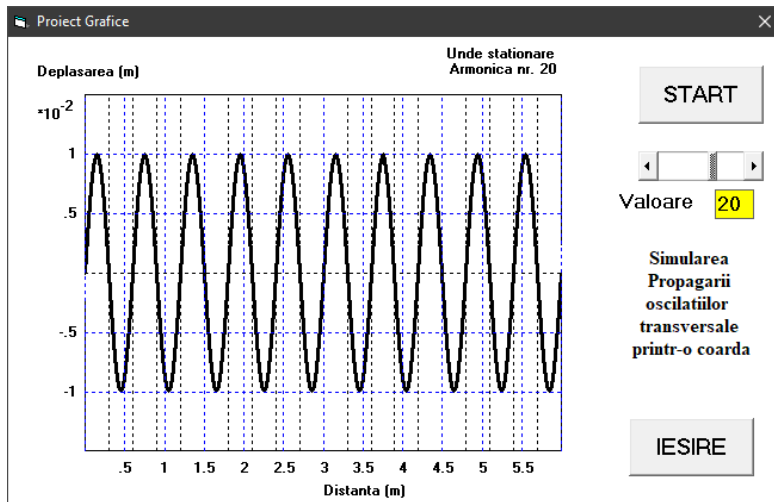


Figure 6. Graphical representation for twentieth order harmonic

4. Conclusion

By means of numerical programming, using improved mathematical algorithm, we implemented a simulator using Visual Basic software. The purpose of program

we have developed for improved, briefly described in this article was to show a solution for simulating eigenmodes of a string, in arbitrary units (1, 3, 5, 10, 20 harmonics). By means of simulator we build up, we can obtain graphical representation of n order harmonics.

Acknowledgement

The work has been funded by the Operational Programme Human Capital of the Ministry of European Funds through the Financial Agreement 51675/09.07.2019, SMIS code 125125.

References

- [1] Hațiegan C., Suciu L., *Fizică Tehnologică. Teorie și aplicații*, Editura Eftimie Murgu Resita, 2010
- [2] Hațiegan C., Gillich G.R., Răduca E., Nedeloni M.D., Cîndea L., *Equation of Motion and Determining the Vibration Mode Shapes of a Rectangular Thin Plate Simply Supported on Contour Using MATLAB*, *Analele Universitatii „Eftimie Murgu“ Resita, Fascicula de Inginerie*, 20(1), Reșița, 2013, pp. 127-138.
- [3] Demsoreanu B., *Metode numerice cu aplicații in fizică*, Editura Academiei Române, 2005.
- [4] Kubilay I.A., Alpkocak A., *Simulation and Visualization of String Vibration using Finite Difference Approximation*, 18th International Congress on Sound and Vibration, Jul.10–14, 2011, Rio de Janeiro, Brazil.
- [5] Chen L.Q., Analysis and Control of Transverse Vibrations of Axially Moving Strings, *Appl. Mech. Rev.*, 58(2), 2005, pp. 91-116.
- [6] Ashdhir P., Goyal N., Tyagi M., *Simulating Boundary Behaviour of Transverse Waves in Strings using SCILAB*, Physics Education, 2020.

Addresses:

- Lect. Dr. Fiz. Cornel Hațiegan, Babeș-Bolyai University, Faculty of Engineering, Piața Traian Vuia, nr. 1-4, 320085, Reșița, c.hatiegan@uem.ro
- Lect. Dr. Eng. Mihaela Dorica Stroia, Babeș-Bolyai University, Faculty of Engineering, Piața Traian Vuia, nr. 1-4, 320085, Reșița, , m.stroia@uem.ro, (*corresponding author)
- Drd. Eng. Muscai Cristian, Polytechnic University of Bucharest, Faculty of Electrical Engineering, Splaiul Independentei nr.313, sector 6, Bucuresti, 060042, Babeș-Bolyai University, Faculty of Engineering, Piața Traian Vuia, nr. 1-4, 320085, Reșița, c.muscai@uem.ro

Contributions to the synthesis and modeling of gear wheels geometry of a double harmonic transmission

Draghița Ianici, Sava Ianici*

The paper presents the geometric synthesis and modeling of the geometry of the three gear wheels (flexible, fixed rigid and mobile rigid) of a double harmonic transmission. The geometric design of the wheels and their teeth was made by using particular relationships that resulted by imposing the specific conditions of harmonic engagement that exist between these wheels. Modeling of the 3D geometry of the wheel gears of the considered double harmonic transmission was performed in the SolidWorks CAD program, based on the geometric parameters resulting from performing the geometric synthesis.

Keywords: *synthesis, modeling, geometry, gear wheel, double harmonic transmission*

1. Introduction

In the literature, numerous works have highlighted, graphically or analytically, the fact that the gearing conditions between the wheel gears of harmonic transmissions are determined mainly by two factors, namely: teeth geometry and deformation curve shape of the flexible wheels. (which also changes depending on the transmission torque and the existing clearances between the transmission elements) [1-6].

In general, the teeth of the flexible wheels of the toothed harmonic transmissions materialize with small modules, so that the teeth have very small dimensions in relation to the dimensions of the wheel and can be considered non-deformable and embedded in its body, and the wheel deforms [7-9].

Geometric synthesis and modeling was performed for the case of a double harmonic transmission (figure 1) which has as a whole the following four elements:

wave generator with cam (1) - as input element, toothed flexible wheel (2) - as intermediate element, fixed rigid wheel (3) and mobile rigid wheel (4) - as output element [10].

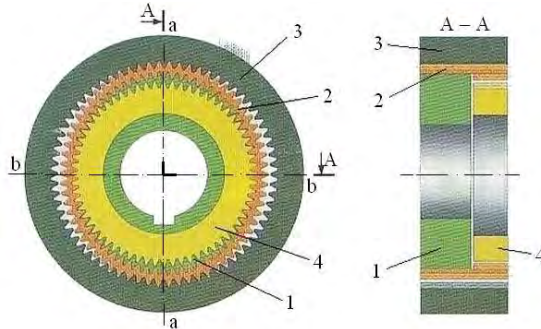


Figure 1. Scheme of the double harmonic transmission

In this transmission, the flexible toothed wheel (2) has the shape of a short, thin-walled flexible circular tube, which is open at both ends and is provided at one end with outer teeth (z_2) and at the other with inner teeth (z'_2).

After assembling the transmission, the cam wave generator (1) is in sliding contact on the entire periphery of the flexible wheel (2), which it deforms elliptically, so that it will have four areas of harmonic engagement, equidistant, two opposite with fixed rigid wheel (first stage of harmonic gear - in direction a-a), respectively two with mobile rigid wheel (second stage of harmonic gear - in direction b-b).

2. Geometric synthesis of double harmonic transmission

The geometric synthesis of the double harmonic transmission aimed at the dimensional-geometric definition of the wheels and their teeth, so as to ensure the imposed functional conditions.

Namely, that the rotational motion is transmitted, with a constant transmission ratio, by the propagation of some elastic deformations on the periphery of the flexible wheel, in the form of harmonic waves.

From the study of the kinematic conditions of the double harmonic transmission, presented in [11-13], it resulted that the optimal profile of the wheels teeth is the rectilinear one, and the teeth in cross section will have a triangular shape (figure 2).

Within the geometric synthesis of the double harmonic transmission with 2-wave deformation generator and with the rectilinear profile of the wheel teeth, the characteristic geometric elements of the wheels and their teeth were determined

according to the tooth modulus (m), by using particular relations which are shown in Table 1.

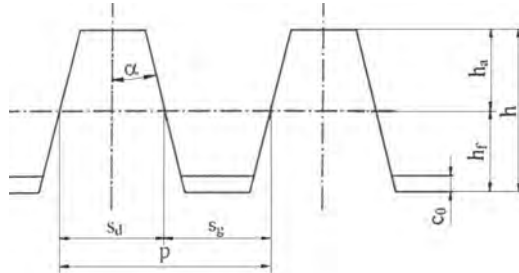


Figure 2. The rectilinear profile of the teeth

Table 1. Geometric synthesis algorithm

Geometric parameter	Calculation relationship
Tooth pitch	$p = \pi \cdot m$
Addendum	$h_a = 7/8 \cdot m$
Dedendum	$h_f = 9/8 \cdot m$
Tooth height/total depth	$h = 2 \cdot m$
Maximum radial clearance	$c_0 = 0,3 \cdot m$
Tooth thickness on the pitch circle	$s_d = 7/16 \cdot \pi m$
Width of the space on the pitch circle	$s_g = 9/16 \cdot \pi m$
Half-angle of the tooth profile	$\alpha = \text{arctg } \pi / 5,76$
Half-angle of the space between the teeth	$\alpha + \Delta\alpha = \alpha + \text{arctg } (3,6693 \cdot m/d_3)$ d_3 - pitch diameter of fixed wheel
Tooth width/face width	$b = (0,1 \dots 0,3) \cdot d_i$; d_i - inner diameter of flexible wheel
Pitch diameter	$d = m \cdot z$
Outside diameter	$d_a = d \pm 2h_a$
Inside diameter	$d_f = d \mp 2h_f$
Wall thickness of flexible wheel in the toothless area	$s = (0,01 \dots 0,02) \cdot d_i$
Length of flexible wheel	$l = s / (0,02 \dots 0,03)$

In table 1, in relations where two signs appear simultaneously, the upper sign for the outer gear wheel is accepted, respectively the lower sign for the inner gear wheel.

Following the application of the proposed algorithm, in the case of the double harmonic transmission with a transmission ratio = 48.47, the values given in table 2 and table 3 were obtained for the main geometric parameters of the gear wheels.

Table 2. Geometric parameters of the gear wheels in the first engagement

Geometric parameter	Value
Teeth module	$m = 0.3 \text{ mm}$
Tooth pitch	$p = 0.9424 \text{ mm}$
Maximum radial deformation	$w_0 = 0.3 \text{ mm}$
Number of teeth of the wheel: fixed/flexible	$z_3 = 202 / z_2 = 200$
Difference in wheel tooth numbers	$n_u = z_3 - z_2 = 2 \text{ dinți}$
Pitch diameter of the wheel: fixed/flexible	$d_3 = 60.6 \text{ mm} / d_2 = 60 \text{ mm}$
Outside diameter of the wheel: fixed/flexible	$d_{a3} = 60.075 \text{ mm} / d_{a2} = 60.525 \text{ mm}$
Inside diameter of the wheel: fixed/flexible	$d_{f3} = 61.275 \text{ mm} / d_{f2} = 59.325 \text{ mm}$
Inner diameter of the flexible wheel	$d = 58.125 \text{ mm}$
Total depth	$h = 0.6 \text{ mm}$
Addendum	$h_a = 0.2625 \text{ mm}$
Dedendum	$h_f = 0.3375 \text{ mm}$
Maximum radial clearance	$c_0 = 0.06 \text{ mm}$
Half-angle of the tooth profile	$\alpha_2 = 28^\circ 36' 31''$
Half-angle of the space between the teeth	$\alpha_2 + \Delta\alpha_2 = 29^\circ 38' 51''$
Tooth thickness on the pitch circle	$s_d = 0.4123 \text{ mm}$
Width of the space on the pitch circle	$s_g = 0.5301 \text{ mm}$
Tooth width of the wheel: fixed/flexible	$b_3 = 12 \text{ mm}; b_2 = 12 \text{ mm}$
Length of the wheel: fixed/flexible	$l_3 = 16 \text{ mm}; l_2 = 30 \text{ mm}$
Wall thickness of flexible wheel	$s = 0,6 \text{ mm}$

Table 3. Geometric parameters of the gear wheels in the 2nd engagement

Geometric parameter	Value
Teeth module	$m = 0.3 \text{ mm}$
Tooth pitch	$p = 0.9424 \text{ mm}$
Maximum radial deformation	$w'_0 = 0.27 \text{ mm}$
Number teeth of the wheel: flexible/mobile	$z'_2 = 192 / z_4 = 190$
Difference in wheel tooth numbers	$n_u = z'_2 - z_4 = 2 \text{ dinți}$
Pitch diameter of the wheel: flexible/mobile	$d'_2 = 57.6 \text{ mm} / d_4 = 57 \text{ mm}$
Outside diameter of wheel: flexible/mobile	$d'_{a2} = 57.075 \text{ mm} / d_{a4} = 57.525 \text{ mm}$
Inside diameter of the wheel: flexible/mobile	$d'_{f2} = 58.275 \text{ mm} / d_{f4} = 56.325 \text{ mm}$
Total depth	$h = 0.6 \text{ mm}$
Addendum	$h_a = 0.2625 \text{ mm}$
Dedendum	$h_f = 0.3375 \text{ mm}$
Tooth thickness on the pitch circle	$s_d = 0.4123 \text{ mm}$
Width of the space on the pitch circle	$s_g = 0.5301 \text{ mm}$
Tooth width of the wheel: flexible/mobile	$b'_2 = 12 \text{ mm}; b_4 = 12 \text{ mm}$
Length of the wheel: flexible/mobile	$l_2 = 30 \text{ mm}; l_4 = 12 \text{ mm}$

The demonstration of the veracity of the values of the geometric parameters of the gears of the double harmonic transmission was made by confirming the fulfillment of the conditions of existence of the harmonic gears in the 2 stages of the transmission.

Figure 3 shows the image of the harmonic engagement in the first stage of the transmission, and in figure 4 shows the image of the harmonic engagement in the second stage.

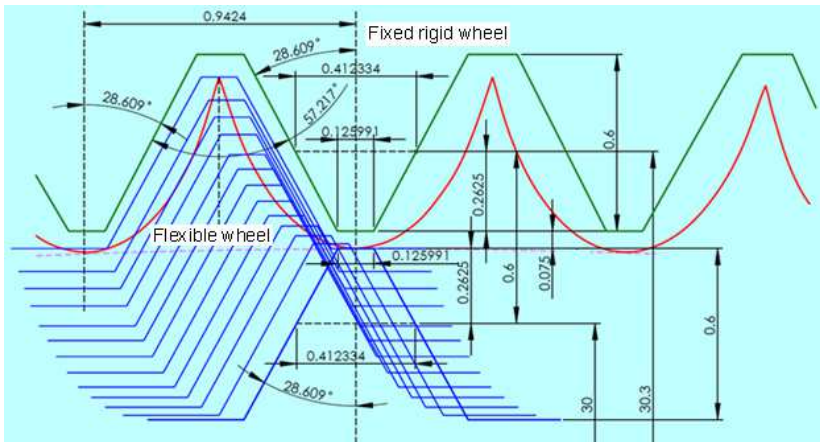


Figure 3. The image of the harmonic engagement in the first stage

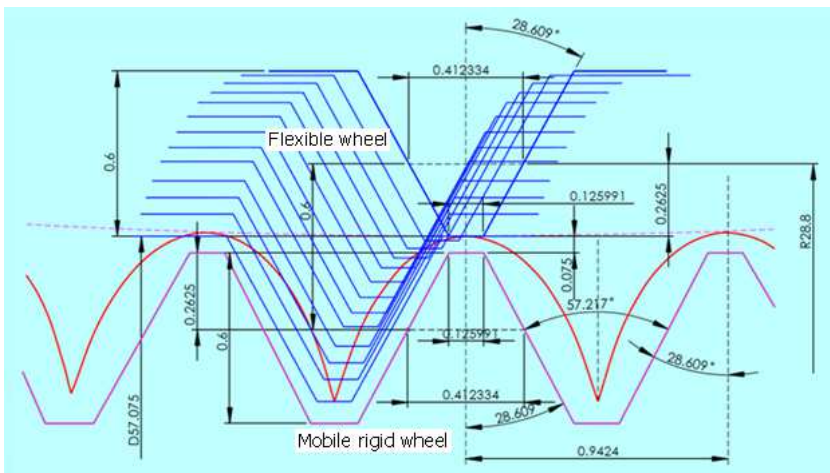


Figure 4. The image of the harmonic engagement in the second stage

The constructive shape and the geometries of the two toothings of the flexible wheel are presented in figure 5.



Figure 5. The geometry of the flexible wheel

3. Modeling the geometry of the gear wheels

The CAD module of the SolidWorks design program was used to generate the models of the three gear wheels of the double harmonic transmission (fixed rigid wheel, flexible wheel and mobile rigid wheel).

The modeling of the 3D geometry of the three gear wheels was done, in principle, by going through the same stages, namely: elaboration of the annular section and its extrusion, extrusion of the minimum diameter, extrusion of the tooth profile and its circular multiplication [14].

The geometric models of the three gear wheels of the double harmonic transmission are presented in figure 6, a – for the fixed rigid wheel, b – for the flexible wheel, c – for the mobile rigid wheel, and in figure 7 the physical constructions of these elements.

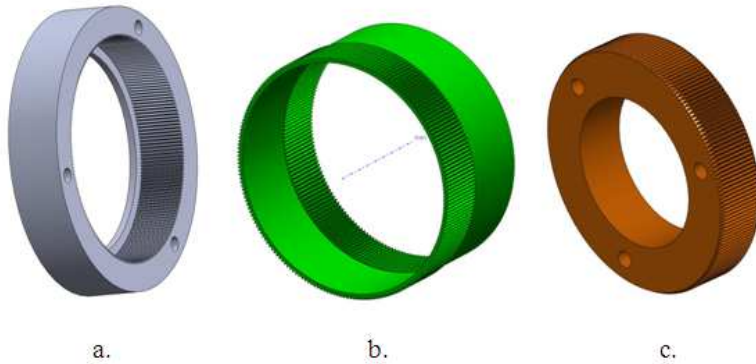


Figure 6. The geometric models of gear wheels

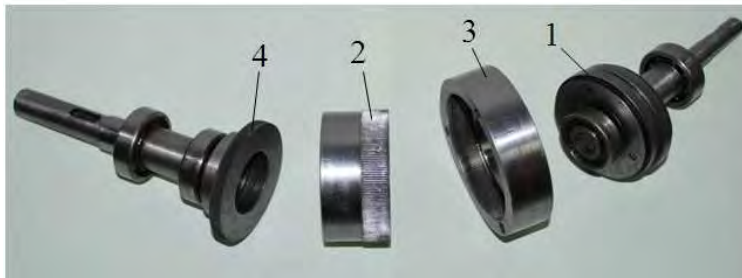


Figure 7. Construction of double harmonic transmission elements

4. Conclusion

The paper presents and proposes a unitary method of geometric synthesis of double harmonic transmissions, which aimed to determine the relations of defining the characteristic geometric parameters of the gear wheels that are part of the respective transmissions.

Based on the presented calculation relations and the computer-aided design, the basic parameters that characterize the harmonic gears from the 2 stages of the transmission were determined, namely: the tooth profile angle (α), the tooth height (h) and the maximum radial deformation size of the flexible wheel (w_0, w'_0).

The geometric models generated for the component gear wheels (fixed rigid, flexible and mobile rigid) were the basis for their physical realization and for the constitution of the double harmonic transmission assembly.

References

- [1] Miloiu G., *Transmisii mecanice moderne*, Ed. Tehnică, 1980.
- [2] Bostan I., Dulgheru V., Grigoraş S., *Transmisii planetare, precesionale și armonice*, Ed. Tehnică, 1997.
- [3] Ianici D., Nedelcu D., Ianici S., Coman L., *Dynamic analysis of the double harmonic transmission*, The 6th International Symposium about Forming and Design in Mechanical Engineering, KOD 2010, Palic, Serbia, pp. 155-158.
- [4] Volkov D.P., *Volnovîe zubciatîe peredaci*, Izd. Nauka, 1976.
- [5] Kovalev N.A., *Peredaci ghibkimi kolesami*, Izd. Maşinostroenie, 1979.
- [6] Ivanov M.N., *Volnovîe zubciatîe peredaci*, Izd. Vîşşaiia Şkola, 1981.
- [7] Ianici S., Ianici D., Constructive design and dynamic testing of the double harmonic gear transmission, *Analele Universităţii „Eftimie Murgu” Reşiţa*, 22(1), 2015, pp. 231-238.
- [8] Ianici S., Ianici D., *Numerical simulation of stress and strain state of the flexible wheel of the double harmonic transmission*, The 8th International Symposium KOD 2014, June 12-15, Balatonfüred, Hungary, pp. 135-138.
- [9] Litvin F.L., *Gear geometry and applied theory*, PTR Prentice Hall, 1994.
- [10] Rujici D., *Contribuţii la perfecţionarea constructiv – funcţională a transmisiilor armonice dinţate duble*, Teza de doctorat, „Eftimie Murgu” University of Resita, 2012.
- [11] Dong H., Zhu Z., Zhou W., Chen Z., Dynamic simulation of harmonic gear drives considering tooth profile parameters optimization, *Journal of Computers*, 7(6), 2012, pp. 1429-1436.
- [12] Ianici S., Ianici D., *Elemente de inginerie mecanică*, Lito. Universitatea Eftimie Murgu Reşiţa, 2015.
- [13] Raihman G. N., *Konstrukcija, rascet i proizvodstvo volnovih zubciatih peredaci*, Izd. Sverdlovsk. 1983.
- [14] Nedelcu D., *Proiectare și simulare numerică cu SolidWorks*, Editura Eurostampa, 2011.

Addresses:

- Lect. Dr. Eng. Draghița Ianici, Babeş-Bolyai University, Faculty of Engineering, Piața Traian Vuia, nr. 1-4, 320085, Reşița, d.ianici@uem.ro
- Prof. Dr. Eng. Sava Ianici, Babeş-Bolyai University, Faculty of Engineering, Piața Traian Vuia, nr. 1-4, 320085, Reşița, s.ianici@uem.ro
(* corresponding author)

Study of the influence of intermittent motion on the orientation kinematic precision of a double harmonic transmission

Sava Ianici, Draghița Ianici*

The paper presents a method and an experimental installation, designed by the authors, for determining the orientation kinematic precision of a double harmonic transmission (DHT). The influence of repeated stops and then continued motion on the orientation kinematic precision of the DHT was researched. The study of the orientation kinematic precision of DHT was performed by taking into account 5 torque steps of DHT, at a constant speed of the driving shaft and maintaining its same direction of rotation. Experimental investigations have shown that the instantaneous transmission ratio of the DHT does not vary significantly from its nominal value and that the orientation kinematic precision of DHT decreases with increasing transmission torque.

Keywords: *double harmonic transmission, transmission ratio, kinematic error, orientation kinematic precision*

1. Introduction

The main trend of the current stage of modernization of the technical industry is the robotization and automation of production processes, through the implementation of industrial robots and the integration of systems commanded and coordinated by computing units. The kinematic performances of the industrial robots are identified, mainly, by the precision of the mechanical movements executed by their elements [1-5].

In this context, the importance of modern gear transmissions has increased, compared to traditional ones, due to the advantages they have in ensuring a precise rotational motion. DHT is included in this category of so-called "unconventional" or "modern" transmissions. DHT it has a number of advantages over other gear

transmissions, namely: high transmission ratio, high kinematic precision of orientation and repeatability, small gauge and mass, self-balanced, low moments of inertia and extremely small clearance, compact and coaxial construction [6-11].

Starting from these aspects, within the Department of Engineering Sciences at the Faculty of Engineering and Management from Resita, a series of researches have been carried out over the years on the structure, kinematics, geometry and dynamics of double harmonic transmissions [12-14].

In the reference [15], the authors presented the results of experimental research conducted in order to determine the kinematic positioning accuracy of DHT. Thus, the influences of the variation of the transmission load, respectively of the reversal of the direction of rotation of the input shaft on the transmission ratio and of the kinematic positioning accuracy of DHT were studied.

This paper is a continuation of this research, the authors aiming to study the influence of the intermittent movement of the input shaft on the orientation kinematic precision of DHT.

2. Calculation of the orientation kinematic error of DHT

The double harmonic transmission (figure1) is used in the following constructive structure: cam wave generator (1), flexible wheel (2), fixed rigid wheel (3) and mobile rigid wheel (4).



Figure 1. The constructive structure of the DHT

The input element of the DHT is the wave generator (1) which deforms the short flexible wheel (2), so that it will have four equidistant engagement areas, two with fixed rigid wheel (3 - which is provided with the inner teeth and others two with the output element represented by the mobile rigid wheel (4 - which is provided with the outer teeth).

Presence in the structure of DHT of a deformable element (flexible wheel) leads to the appearance of a own kinematic error of the transmission. In addition to this, errors can also occur due to improper execution and incorrect mounting of the gear wheels.

The orientation kinematic precision of DHT was evaluated by the positioning error of the driven element of the transmission. The positioning kinematic error (also called orientation kinematic error) was defined as the difference between the effective and the theoretical rotation angle of the transmission output shaft.

The calculation methodology of the orientation kinematic error of DHT is based on the following successive stages:

- calculation of transmission ratio of the DHT:

$$i_{14}^{(3)} = \frac{z_2 \cdot z_4}{z_2' \cdot z_4 - z_2' \cdot z_3} \quad (1)$$

where: z_2, z_2', z_3, z_4 are the numbers of teeth of the wheels.

- calculation of the theoretical rotation angle of the driven element of the DHT:

$$\varphi_{4t} = \frac{\varphi_1}{i_{14}^{(3)}} \quad (2)$$

where: $i_{14}^{(3)}$ is the theoretical transmission ratio of the DHT, φ_1 - the rotation angle of the wave generator.

- calculation of the orientation kinematic error of DHT:

$$\Delta\varphi = \varphi_{4r} - \varphi_{4t} \quad (3)$$

where: $\Delta\varphi$ is the orientation kinematic error; $\varphi_{4r}, \varphi_{4t}$ - the effective rotation angle of the driven element, respectively the theoretical one.

3. Construction of the experimental installation

In figure 2 shows the experimental installation used to investigate the orientation kinematic precision of researched DHT.

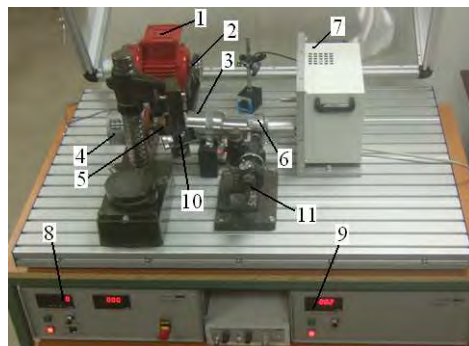


Figure 2. Construction of the experimental installation

The experimental installation consists of: 1 - the asynchronous electric motor, 2 - the transmission with narrow trapezoidal belt, 3 - the double harmonic transmission, 4 - the incremental position transducer, 5 - the elastic coupling, 6 - the divided disk, 7 - the brake with magnetic particles, 8, 9 - the diagnostic systems and 10, 11 - the optical systems for direct reading of the rotation angles of the transmission shafts.

4. Research and experimental results

The experimental research aimed to study the influence of repeated stops and starts of DHT on the transmission ratio and the orientation kinematic error of its.

Experimental research was performed on a DHT, with the following parameters: transmission ratio, $i_{14}^{(3)} = 48.2$; the number of teeth of the wheels, $z_2 = 200$ teeth, $z_3 = 202$ teeth, $z'_2 = 190$ teeth and $z_4 = 188$ teeth.

The measurements of the rotation angles of the shafts was done by considering 5 loading steps of the transmission ($M_{t4} = 0; 2; 5; 7.5; 10$ Nm) and maintaining a constant input speed ($n_1 = 500$ rpm) and the same direction of rotation.

The results obtained by recording the values of the rotation angle of the DHT output shaft and performing the related calculations are presented in Table 1.

Table 1. The orientation kinematic error

Torque M_{t4} [Nm]	Rotation angle φ_4 [°,',"]			Angle φ_1 [°]	Tran. ratio i_{14}	Mediate i_{14}	Kin. error $\Delta\varphi$ ["]
	initial	final	real				
0	0°2'12"	93°23'42"	93°21'30"	4500	48.2013	48.2015	13.335
	93°23'42"	186°45'06"	93°21'24"	9000	48.2017		
	186°45'06"	280°06'35"	93°21'29"	13500	48.2016		
	280°06'35"	373°27'57"	93°21'22"	18000	48.2018		
2	0°00'36"	93°21'12"	93°20'36"	4500	48.2091	48.2097	79.335
	93°21'12"	186°41'39"	93°20'27"	9000	48.2097		
	186°41'39"	280°01'49"	93°20'10"	13500	48.2197		
	280°01'49"	373°21'57"	93°20'08"	18000	48.2113		
5	0°01'18"	93°21'10"	93°19'52"	4500	48.2154	48.2139	132.035
	93°21'10"	186°40'32"	93°19'22"	9000	48.2175		
	186°40'32"	280°59'40"	93°19'08"	13500	48.2189		
	279°59'40"	373°19'08"	93°19'28"	18000	48.2189		
7.5	0°01'35"	93°20'25"	93°18'50"	4500	48.2243	48.2235	179.335
	93°20'25"	186°39'13"	93°18'48"	9000	48.2244		
	186°39'13"	279°57'45"	93°18'32"	13500	48.2252		
	279°57'45"	373°16'16"	93°18'31"	18000	48.2257		
10	0°00'16"	93°18'14"	93°17'58"	4500	48.2317	48.2270	209.335
	93°18'14"	186°36'24"	93°18'10"	9000	48.2309		
	186°36'24"	279°54'42"	93°18'18"	13500	48.2302		
	279°54'42"	373°12'57"	93°18'15"	18000	48.2300		

Figure 3 shows the variation diagram of the instantaneous transmission ratio, and in figure 4 is presented the orientation kinematic error diagram of the DHT.

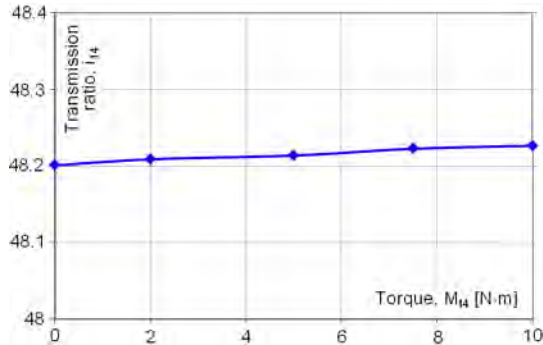


Figure 3. Transmission ratio of the DHT

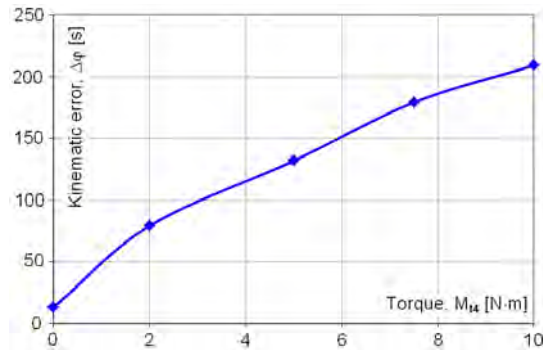


Figure 4. Kinematic error of orientation of the DHT

4. Conclusion

The paper presents a method of experimental determination of the orientation kinematic error of the DHT. The influence of repeated stops and continuations of motion on the orientation kinematic precision of DHT was studied.

The experimental tests were performed on a DHT with a short flexible wheel and consisted in measuring and recording the rotation angle of the output shaft for different angles of rotation of the input shaft.

From the analysis of the results of the experimental tests it was found that by repeated stops and starts, in the same direction, for the same torque, the transmission ratio of the DHT does not change significantly compared to the nominal value ($i_{14}^{(3)} = 48.2$). It was also found that as the DHT torque increases, there is an increase in the orientation kinematic error of the DHT output shaft, thus at $M_{14} = 0$ N·m it was obtained $\Delta\varphi = 13.3''$ and at $M_{14} = 10$ Nm it was obtained $\Delta\varphi = 209.3''$.

References

- [1] Ianici S., Ianici D., *Elemente de inginerie mecanică*, Universitatea Eftimie Murgu Reșița, 2015.
- [2] Frolov K.V., Vorobiev V.I., *Mehanika promîșlienîh robotov*, vol. 1, 2, 3, Izd. Vîșșaia Șkola, 1988/1989.
- [3] Miloiu G., *Transmisii mecanice moderne*, Ed. Tehnică, 1980.
- [4] Bostan I., Dulgheru V., Grigoraș S., *Transmisii planetare, precesionale și armonice*, Ed. Tehnică, 1997.
- [5] Kovalev N.A., *Peredaci ghibkimi kolesami*, Izd. Mașinostroenie, 1979.
- [6] Ivanov M.N., *Volnovîe zubciatîe peredaci*, Izd. Vîșșaia Șkola, 1981.
- [7] Istomin S.N., *Kinematiceskaia tocinost pribornîh volnovîh peredaci*, Izd. Mașinostroenie, 1987.
- [8] Litvin F.L., *Gear geometry and applied theory*, PTR Prentice Hall, 1994.
- [9] Ghinzburg G., *Volnovîe zubciatîe peredaci*, Izd. Mașinostroenie, 1977.
- [10] Harachová D., Solution and modification in the profile the harmonic drive, *GRANT Journal*, 2014, pp. 73-76.
- [11] Dong H., Zhu Z., Zhou W., Chen Z., Dynamic simulation of harmonic gear drives considering tooth profile parameters optimization, *Journal of Computers*, 7(6), 2012, pp. 1429-1436.
- [12] Ianici D., Ianici S., Dynamic research of the flexible wheel of a double harmonic gear transmission, *Analele Universității „Eftimie Murgu” Reșița, Fascicula de Inginerie*, 22(1), 2015, pp. 223-230.
- [13] Ianici S., *Contributions on determining the forces distributions in the toothed harmonic drive (THD)*, The 8th Symposium International Mechanisms and Mechanical Transmissions - MTM 2000, Timisoara, Romania, pp. 165-168.
- [14] Ianici S., Vela I., Ianici D., Micloșină C.O., *Double harmonic transmission used in industrial robotic drives*, Proceedings of the 2nd International Conference on Robotics, Oct. 14-16, 2004, Timișoara, Romania, pp. 89-90.
- [15] Ianici S., Ianici D., Experimental determination of kinematic precision of positioning of a double harmonic transmission, *Analele Universității „Constantin Brâncuși” din Târgu Jiu*, *Seria Inginerie*, nr. 2, 2019, pp. 139-144.

Addresses:

- Prof. Dr. Eng. Sava Ianici, Babeș-Bolyai University, Faculty of Engineering, Piața Traian Vuia, nr. 1-4, 320085, Reșița, s.ianici@uem.ro
- Lect. Dr. Eng. Draghița Ianici, Babeș-Bolyai University, Faculty of Engineering, Piața Traian Vuia, nr. 1-4, 320085, Reșița, d.ianici@uem.ro (*corresponding author)

The study of the elastic deformation of a flexible wheel by a cam wave generator

Sava Ianici, Draghița Ianici*

The paper presents the results of research on the study of the elastic deformation of a flexible wheel from a double harmonic transmission, under the action of a cam wave generator. Knowing exactly how the flexible wheel is deformed is important in correctly establishing the geometric parameters of the wheels teeth, allowing a better understanding and appreciation of the specific conditions of harmonic gearings in the two stages of the transmission. The veracity of the results of this theoretical study on the calculation of elastic deformations and displacements of points located on the average fiber of the flexible wheel was subsequently verified and confirmed by numerical simulation of the flexible wheel, in the elastic field, using the finite element method from SolidWorks Simulation.

Keywords: *deformation, displacement, flexible wheel, cam wave generator, double harmonic transmission*

1. Introduction

Toothed harmonic transmissions are widely used in the construction of numerous automation equipment and high-performance systems, such as: cosmic ships and rockets, airplanes, helicopters, radar antennas, joints of industrial robots, atomic reactors, naval mechanisms, servo-mechanisms, motors-reducers, machine tools, shareholders in hermetic spaces, etc. [1-5].

However, the durability of harmonic transmissions is limited, being conditioned by the durability of the flexible wheel, which is subject to complex dynamic stresses, both from the wave generator and from the fixed rigid wheel.

Since the advent of harmonic transmission, many specialists have focused on researching the dynamic behavior of the toothed flexible wheel. Thus, Sahoo and Maiti investigated the state of stresses and strains in the case of a long flexible

wheel cup-type deformed by a cam wave generator [6], Zou et al. determined stress and deformation states of short flexible wheel, also of the cup-type deformed by a cam wave generator [7]. Folega chose as a model of analysis a short flexible wheel with external teeth, deformed by a wave generator with discs [8], and Dong et al. they established an analysis model also consisting of the long flexible wheel cup-type, and took into account the action of the alternative dynamic load [9].

In this context, the present paper aimed to investigate the deformation of short flexible wheel from a double harmonic transmission, under the action of a cam wave generator.

Double harmonic transmissions are part of the category of toothed harmonic transmissions, characterized by a high orientation accuracy, compact and coaxial construction, small backlash, low axial size and small mass, high transmission ratio, etc. [10], [11]. The structure of the double harmonic transmission subjected to the research is presented in figure 1. It consists of: cam wave generator (1), flexible wheel (2), fixed rigid wheel (3) and mobile rigid wheel (4).

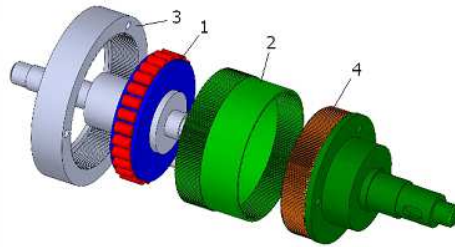


Figure 1. The structure of the double harmonic transmission

In the case of a double harmonic transmission, the short flexible wheel has the shape of a flexible circular tube with a thin wall, which is open at both ends and is provided at each end with teeth (at one end with outer teeth and at the other end with inner teeth).

By forcibly mounting the wave generator (1) inside the flexible wheel (2), it deforms elliptically and will have four equidistant engagement zones: two with fixed rigid wheel (3 - having inner teeth) in the left front plane of the flexible wheel and two others with mobile rigid wheel (4 - having outer teeth) in the right front plane of the flexible wheel. There is a 90° angle between the two pairs of opposite gear areas.

2. The deformation of the flexible toothed wheel

The functional performance and durability of the double harmonic transmission are largely influenced by the manufacturing accuracy of the flexible wheel and the

wheel deformation law, which in turn depends on its geometry, the type of wave generator and how it is coupled to the output shaft.

In order to investigate the deformation of the flexible wheel, it is admitted the hypothesis that the average fiber of the deformed wheel keeps its elliptical shape and constant length in any cross section of it, because the deformations produced are in the elastic domain.

It has also been admitted that the elliptical deformation of the flexible wheel is performed according to the cosinusoidal law, which can be reproduced with a good approximation, with the help of a generator with two deformation waves, with an elliptical profiled cam (figure 2).

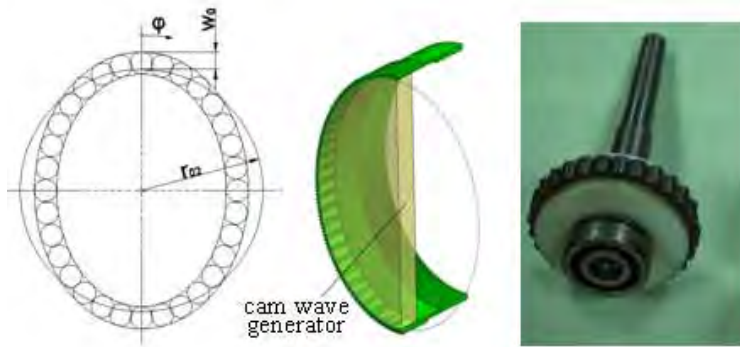


Figure 2. The model and construction of the cam wave generator

The static pictures of the deformation of the short flexible wheel, in its two frontal cross-sections, were defined by means of the calculation relations of the radial (w, w') and tangential (v, v') displacements of the points located on the average fibers from the two front sections of the wheel as well as the angle of rotation of the normal ((θ, θ')), valid for the case of a cam wave generator:

$$w = w_0 \cdot \cos 2 \varphi \quad (1)$$

$$v = - (w_0 / 2) \cdot \sin 2 \varphi \quad (2)$$

$$\theta = (3 w_0 / 2r_0) \cdot \sin 2 \varphi \quad (3)$$

where: w_0 - is the maximum radial deformation; r_{02} - the average fiber radius of the undeformed flexible wheel; φ - the angular parameter of the cam wave generator.

The calculation relations for the elastic deformations (w , v , θ) of the flexible wheel in the front section where the wave generator operates they are valid and for the front section at the opposite end of the wheel (to the calculation w' , v' , θ'), with the observation that the maximum radial deformation value w_0 will be replaced with $w_0' = 0.27$ mm.

Figure 3 shows the variation diagrams of the radial displacements (w ; w'), tangential (v , v') and of the rotation angle of the normal (θ ; θ') depending on the angular parameter φ of the cam wave generator, for points located on the middle fiber in the two front sections of the deformed flexible wheel (characterized by: $r_{02} = 29.3$ mm; $w_0 = 0.3$ mm and $w_0' = 0.27$ mm).

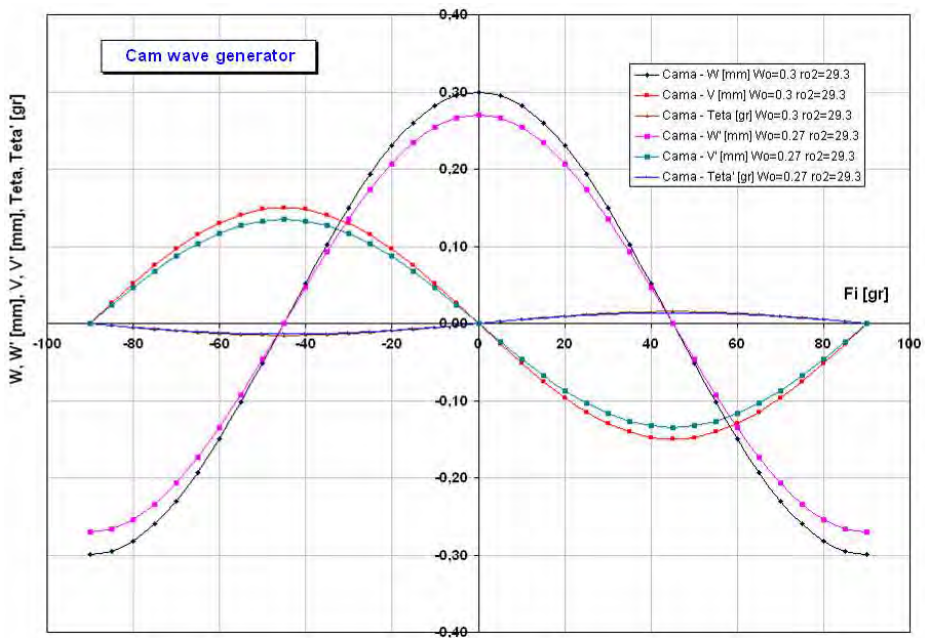


Figure 3. Diagrams of elastic deformations of the short flexible wheel

From the comparative analysis of the curves of variation of radial and tangential displacements it can be seen that these curves keep the same shape in both front sections of the flexible wheel, and the maximum radial deformation in the front section where the cam wave generator operates always has the value greater than the maximum radial deformation in the other front section.

Figure 4 shows the dependence between radial displacements (w , respectively w') and tangential ones (v , respectively v'), for the case of static deformation of the short flexible wheel by the cam wave generator.

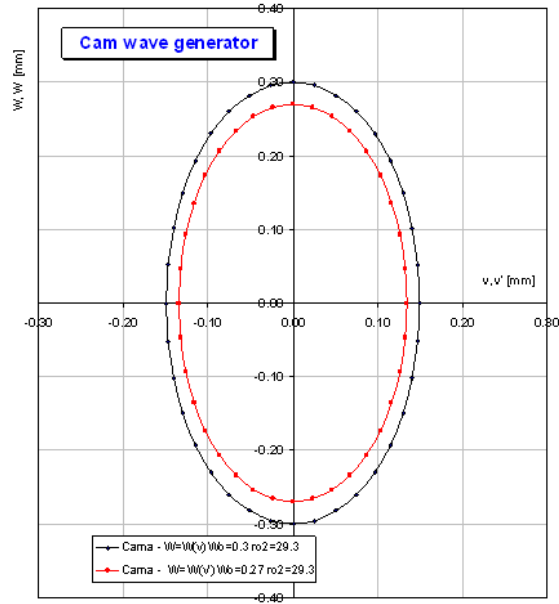


Figure 4. Radial displacement diagram as a function of tangential displacement

3. Numerical simulation of the flexible wheel dynamic

The numerical simulation of the flexible wheel dynamic was performed for the case of elastic deformation of the wheel by a cam wave generator, using the finite element method, from the SolidWorks Simulation module [12].

In the numerical calculation, the flexible wheel was modeled by an open cylinder at both ends, defined by: radius $r_{02} = 29.3\text{mm}$, length $l = 30\text{ mm}$ and wall thickness $s = 0.6\text{ mm}$, which is provided at the ends with the teeth (outer and inner, respectively) having a width equal to 12 mm.

Within the numerical analysis performed, the variations of von Mises displacements and tensions in the flexible wheel body were studied, depending on the loading moment of the transmission.

Figure 5 shows, in the form of color maps, the distribution of the von Mises tensions ($\sigma_{\text{von Mises}}$) and the resulting displacement (Δ) of the flexible wheel body, for a load $M = 100\text{ Nm}$.

It has been found that the stresses arising in the flexible wheel wall are dependent on the transmission load, having a slightly increasing character as the transmission load increases. The maximum tension appears in the area of contact with the wave generator, in the direction of the large axis of the ellipse.

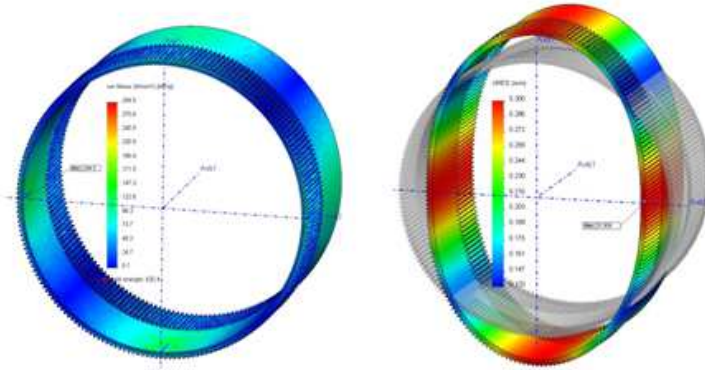


Figure 5. Distribution of $\sigma_{\text{von Mises}}$ tension and resulting displacement Δ

Figure 6 shows, in the form of color maps, the resulting displacements Δ of the characteristic nodes located on the generator N, respectively on the generator E of the deformed flexible wheel, for a load $M = 100 \text{ Nm}$.

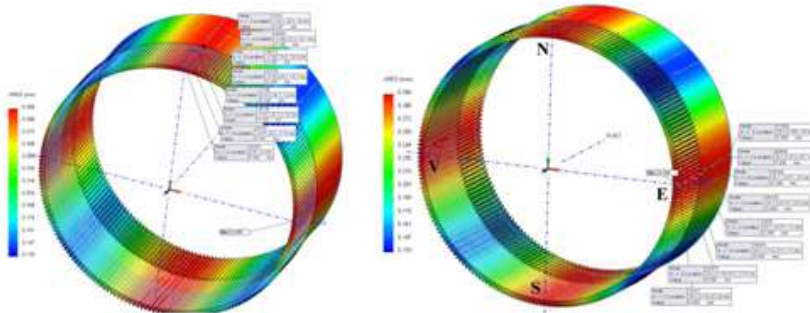


Figure 6. The variation of the displacement Δ along the generators N and E

Figure 7 shows the variation curves of the displacements of the nodes positioned on the two generators (N and E) of the flexible toothed wheel, for a load $M = 100 \text{ Nm}$.

From the analysis of the resulting displacement variation diagram $\Delta = \Delta(z)$, it is observed that in the area of the application point of the deformation force of the

flexible wheel (corresponding to the position $z = 0$, on the generator N) is obtained the value of the maximum radial deformation ($\Delta(0) = w_0 = 0.3 \text{ mm}$).

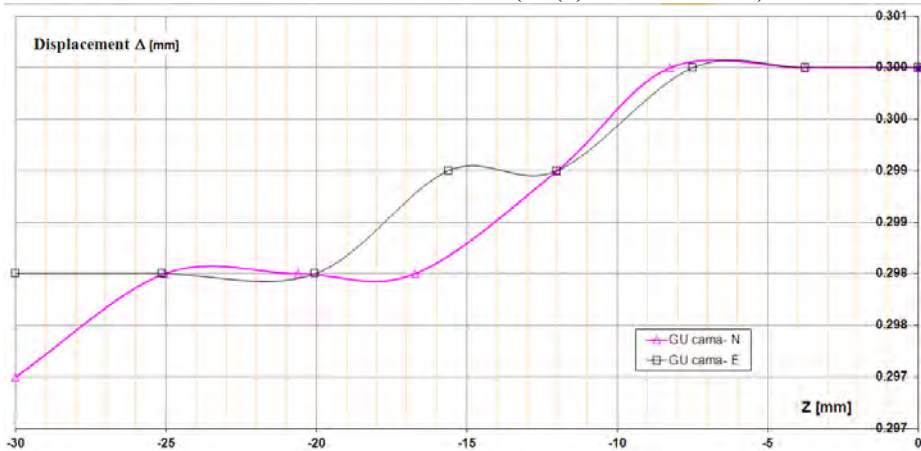


Figure 7. The variation of the displacement Δ along the generators N and E

It is observed that the resulting displacement of the nodes located on the two generators of the deformed flexible wheel has a slightly decreasing character in relation to the increase of the positioning distance of the node with respect to the NSVE plane of the flexible wheel.

4. Conclusion

The paper presents the results obtained following the application of an analytical calculation method of the elastic deformations of the flexible wheel, which is based on a cosinusoidal law of wheel deformation by a cam wave generator.

The correctness of these results was verified and confirmed by numerical simulations performed on the flexible wheel of the double harmonic transmission, using the finite element method from the SolidWorks Simulation program.

From the comparative analysis of these results it was found that the tensions in the flexible wheel wall are dependent on the transmission load and have a slightly increasing character as the load increases. The maximum tension appears in the contact area with the cam wave generator, in the direction of the large axis of the ellipse.

From the study of the variation curves of the resulting displacement of the nodes located on the two generators (N, E) it is observed that the resulting displacement has a slightly decreasing character with the increase of the positioning distance of the nodes in relation to the NSVE face of the flexible wheel, fact confirmed by the results of the analytical study.

References

- [1] Ianici S., Ianici D., *Elemente de inginerie mecanică*, Universitatea Eftimie Murgu Reșița, 2015.
- [2] Frolov K.V., Vorobiev V.I., *Mehanika promîșlienîh robotov*, vol. 1, 2, 3, Izd. Vîșșaiia Șkola, 1988/1989.
- [3] Ivanov M.N., *Volnovîe zubciatîe peredaci*, Izd. Vîșșaiia Șkola, 1981.
- [4] Ghinzburg G., *Volnovîe zubciatîe peredaci*, Izd. Mașinostroenie, 1977.
- [5] Kovalev N.A., *Peredaci ghibkimi kolesami*, Izd. Mașinostroenie, 1979.
- [6] Sahoo V., Maiti R., *State of stress in strain wave gear flexspline cup on insertion of drive cam - experiment and analysis*, Proceedings of the World Congress on Engineering 2016, Vol. II, WCE 2016, 29 June - 1 July, 2016, London, U.K.
- [7] Zoo C., Tao T., Jiang G., Mei X., *Deformation and stress analysis of short flexspline in the harmonic drive system with load*, Proceedings of 2013 IEEE, International Conference on Mechatronics and Automation, 4 - 6 August, 2013, Takamatsu, Japan, pp. 676-680.
- [8] Folega P., Analysis of stress state of toothed ring of flexspline by means the BEM, *Archives of Material Science and Engineering*, 59(1), 2013, pp.40-45.
- [9] Dong H., Zhu Z., Zhou W., Chen Z., Dynamic simulation of harmonic gear drives considering tooth profile parameters optimization, *Journal of Computers*, 7(6), 2012, pp. 1429-1436.
- [10] Ianici S., Ianici D., Constructive design and dynamic testing of the double harmonic gear transmission, *Analele Universității „Eftimie Murgu” Reșița, Fascicula de Inginerie*, 22(1), 2015, pp. 231-238.
- [11] Ianici S., Ianici D., *Numerical simulation of stress and strain state of the flexible wheel of the double harmonic transmission*, The 8th International Symposium KOD 2014, 12-15 June, Balatonfured, Hungary, pp. 135-138.
- [12] Rujici D., *Contribuții la perfecționarea constructiv-funcțională a transmisiilor armonice dințate duble*, Teza de doctorat, Universitatea „Eftimie Murgu“ din Reșița, 2012.

Addresses:

- Prof. Dr. Eng. Sava Ianici, Babeș-Bolyai University, Faculty of Engineering, Piața Traian Vuia, nr. 1-4, 320085, Reșița, s.ianici@uem.ro
- Lect. Dr. Eng. Draghița Ianici, Babeș-Bolyai University, Faculty of Engineering, Piața Traian Vuia, nr. 1-4, 320085, Reșița, d.ianici@uem.ro
(* corresponding author)

Sacredness to desecration: ‘Languaging’ and ‘othering’ of peoples and places through dumping of domestic waste in Urora, Benin City, Nigeria

Hope Iyawe*

This paper examines the dynamics of environmental change of physical spaces and the behaviour of the residents of a formerly close-knit community whose belief systems are contrary to their lifeworld situation as observed in Urora settlement in Benin City, Nigeria. The findings revealed that the satellite images show that the study area was much greener 20 years ago and environmentally attractive compared to the current time. Lack of infrastructure such as waste bins has led to a shift in mindset among the residents to accommodate illegal dumping contrary to attitudes in the past. Population growth and refuse generation and disposal is also a significant challenge. Based on the findings, the paper posits for the realignment and reconsideration of the embodied sacredness of nature with the mode of expression of the past which was pro-environmentally inclined and focussed.

Keywords: *sacredness, desecration, languaging, othering, domestic waste*

1. Introduction

Urora’s lifeworld has parallels with some settlements of sub-Saharan cities. Most residents in formerly close-knit communities in sub-Saharan African countries experience some degree of human-human-environment dislocations as their areas undergo population explosion especially due to rapid urbanisation (Ogu, 2000). One example of this dislocation arises from inadequate waste management services which force residents to live contrary to their belief systems regarding sanitation, thus contributing to cognitive dissonance. Evidence abounds that the majority of residents in sub-Saharan African cities subscribe to spiritual belief systems which

are against indiscriminate waste disposal (Millar *et al.*, 2005; Ajala, 2011; Ojedokun and Balogun, 2013; Iyawe, 2019). In some communities, certain spaces are designated as sacred in line with peoples' specific religious beliefs. However, increasing urban sprawl, population explosion and inadequate physical planning/infrastructural development have contributed to escalation in solid waste disposal challenges.

The scenario of waste disposal has, in turn, affected residents' language of interaction as they communicate with one another especially when trying to achieve the balance between normative goal of cleanliness and godliness on the one hand; and on the other hand, dispose refuse indiscriminately due to weak management services (Iyawe 2019). Researchers have agreed that the language of interaction defines implicitly or explicitly human beings in the world as the exercise is a product of engagement of the competing individual wants and desires (Becker, 1991). Consequently, in this lifeworld situation, sounds from the style of communication/expression have become contrary to the meanings they are supposed to convey in the ensuing exchange of living together in the community. In the sociological context, the process whereby a majority or a minority constructs a shared 'Us-Them' representation of another group by using discourses of class, gender and social order is referred to as 'othering' (Palfreyman, 2005, Zabus, 1990). Adesanmi (2011) describes otherness as how people see themselves as the 'norm' while seeing others who do not 'look' like them as inferior, primitive and anomalous. The resultant social identities reflect how individuals and groups internalise stereotyped social categories within their social systems. The use of class, gender and social order distinctions appears to resonate among different communities globally where issues of cultural differences, language barriers and religious persuasions seem to have taken centre stage in the day to day lives of the people (Medina, 2000; Adesanmi, 2011).

Given these developments and from the perspectives of the everyday life, the study presents a picture of a transition from sacredness to the desecration to illustrate the dynamics of environmental change of the physical space and the resultant behaviour of residents. This change is analysed within the full cycle of waste from the source to waste to the dump as well as change in the languaging involved. Using ethnographic and phenomenological data, the study explains how once a rich natural environment with sacred grooves became degraded through ad-hoc developments and the resultant indiscriminate waste disposal. The relationship between sacred natural environment and desecration of the landscape has escalated primarily due to the intensification of activities of rural-urban migration and spatial expansion. Thus, for the peoples' well-being, the dynamics of environmental change and the behaviour of residents in response to waste management challenges through languaging and practices of waste disposal are not mutually isolated but can be assumed rhizomatically as reciprocally influential. The paper, therefore, contributes

to an understanding of the environmental change of physical spaces and the environmental behaviour of low-income residents whose belief systems and cosmology stands contrary to their daily live experiences (see Figure 1). The four key objectives of the reported study are;

- To illustrate that indiscriminate waste disposal strongly correlates with inadequate planning, population explosion due to rapid urbanisation and the erosion of cultural and religious values:
- To illustrate the extent to which the mother-tongue language of the community (as a means of communication/expression during waste generation and disposal) has changed over time in tandem with the changing landscape.
- To substantiate on why residents desecrate certain places while largely sparing religious and residential places.
- To demonstrate the significance of kinship, age and gender considerations (“in/out-group”) in relation to assigning roles and responsibilities and how this is being challenged by itinerant push-cart and scavengers as an emergent component of the waste disposal cycle.

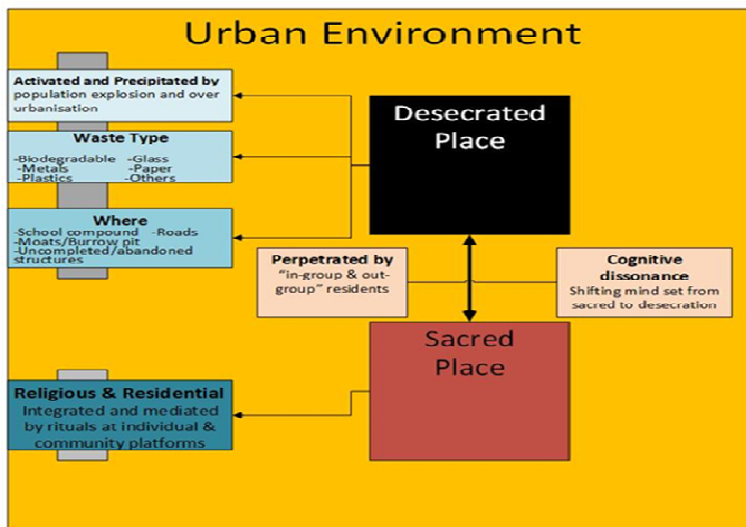


Figure 1. Conceptual mapping of environmental and behaviour change of Urora residents

2. Research methodology

2.1. Study area: Urora

Urora lies between latitudes 6° 22'04", 6° 22'43" N and longitudes 5° 41'11", 5° 42'23" E with a population of 48 219 (2018 estimate projected from the 2006

National Population Census). It is situated within Ikpoba-Okha Local Government Council which is one of the 18 local councils of Edo state. Idogbo, which serves as the administrative headquarters of the council is about 20 kilometres away from Urora. However, the study location has been engulfed by Benin City, the state capital, due to population explosion especially arising from rapid urbanisation (see Figure 2). Ikpoba-Okha has a projected population of 425 860 on a land area of 862km² and a density of 494 inhabitants per km² (2011 estimate of population from the 2006 National Population Census).

On traditional administrative setup, while the Oba holds sway in Benin City and beyond (as other traditional leaders are hierarchically subordinate to the Oba), the neighbouring communities have *Enigies* (plural for *Enogie*) as their traditional heads, Urora has a traditional priest (*Ohen*). This arrangement may explain the presence of the shrine close to the main entrance to the community and also the celebration of certain feasts and festivals (such as *Igue* and *Ikpoleki*) at certain times of the year. Traditionally, and also for contemporary administrative convenience, the settlement is sub-divided into three quarters, namely Urora I (*Ohen* quarters), Urora II (across the Benin-Okene-Abuja highway), and Urora III (*Aideyanba* Quarters). Each of these quarters has their local traditional head as chiefs or *Ohen*.

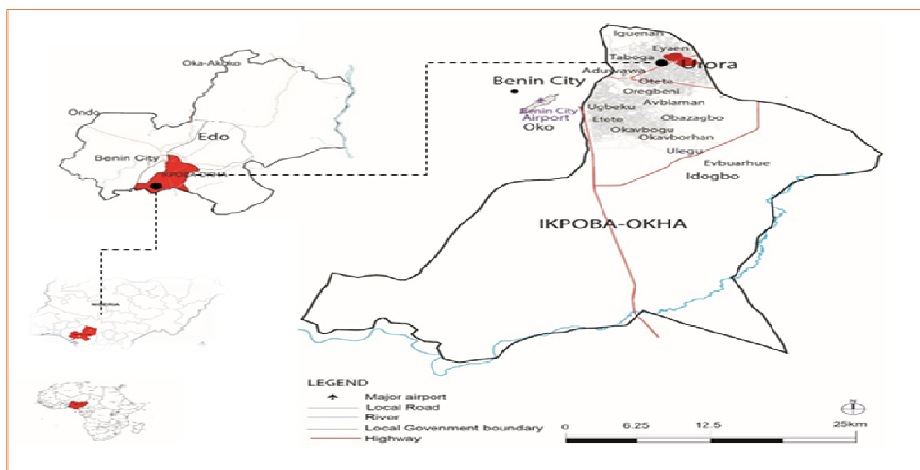


Figure 2. Map of Edo state showing Ikpoba-Okha and Urora
Source: ESMLH,1990

2.2. The phenomenological and ethnographic study

The study adopted a combination of phenomenological and ethnographic approaches which focussed on the essence and lived experiences of resident

participants as the researcher used four and half months while assuming a participant-observation in the fieldwork. The phenomenological research aimed at suspending prior value judgements and focusing on pursuing the meaning of the phenomena from the perspective of the participants' experiences. This approach focused on participants' awareness, experiences and related responses to the solid waste. The interview questions sought to explore the lived experiences especially around the themes such as sacredness, desecration and language adaptations. Examples are:

- What is the local understanding of the concept of waste (mother-tongue words and what they connote)?
- In your mother-tongue is there a word for the people who handle waste?
- Describe your experience/encounter with the solid waste disposal/management process from generation at home to disposal at the public open space, would you say there is a specific person assigned the role to sweep/pack/dispose solid waste on a regular basis?
- Any particular reason why it should be that person and not other members of the household?
- How regularly is the solid waste generated and disposed from the homestead?
- With what container(s) is the solid waste disposed from the homestead?
- What value do they place on waste?
- Would the head of households be involved in waste management/disposal?

2.2.1. Data collection

Data for the study were collected as part of more extensive research conducted throughout 4 and half months between November 2016 to March 2017 and July 2017. The study has four main stages: *Stage 1* involved GPS in order to produce an updated base map with readings of meaning-making features of the settlement as none was readily available. The production of the map was complemented with the production of the 1997 and 2017 historical satellite imagery of the area to show at a glance the trend of physical developments in the area over the last 20 years (see Figure 3). The primary data collection stage of the study was facilitated by a resident gate-keeper/key informant who guided the researcher around to see the settlement.

2.2.2. Data presentation of place, 'inner-to-outer' and 'othering

Rural-urban migration, population explosion and the unbridled urbanisation of Benin City has had a spill-over effect on the settlement of Uroora. In particular, the

built area has increased by 58 % while the vegetation has decreased by almost 100% over a twenty-year period (see Figure 3).

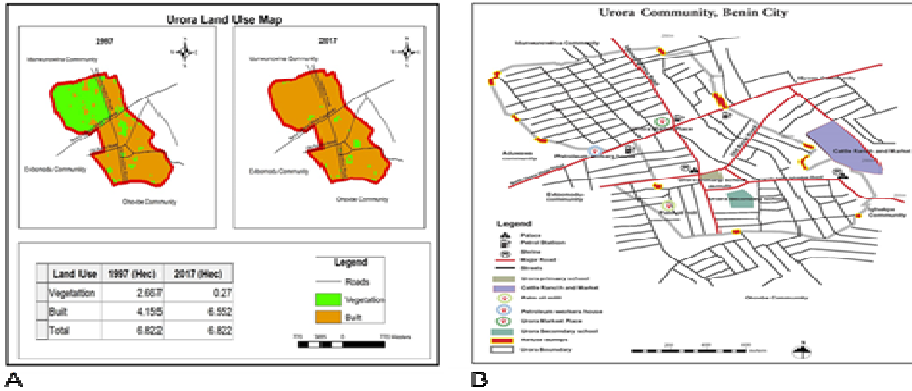


Figure 3a. Satellite Imagery of Urora community 1997 and 2017
Source: ESMLH, 1990

Figure 3b. Urora community showing the roads and PA features
Source: Field survey November 2016-March 2017

2.2.3. The solid waste story of research participants

After shadowing these households for five days, the researcher undertook an in-depth phenomenological interview in the homes of 3 heads of households selected according to the following criteria:

- Head of household, a population of seven, non-Urora indigene, a Christian.
- Head of household, population of seven persons, Urora indigene, a new convert from ATR to Christianity.

Another interesting aspect of the study is the inclusion of an indigene to shed some light on the use of the host community mother tongue in the solid waste story. The reason for this was purely pragmatic as I had access to the three heads of households. Therefore, part of the focus of this paper is to re-live the experience of waste generation and disposal activities that facilitated the physical conditions of the settlement from sacredness to desecration.

- Head of household, family population of eight persons, non-Urora indigene, a Muslim.

2.2.4. A case study of the three families

The household is a Christian family size of seven headed by a 50-year-old businessman and lives at the boundary between Urora and Eyaen communities (approximate location marked “3” on Figure 4). Table 1 presents the solid waste gen-

erated by this family for about five days in different categories from March 6-10, 2017.

Table 1. Waste composition per capita and in percentage, Christian family, a population of 7, off Idunmwunowina

Waste type	Kg
Biodegradable	0.9
Plastics	0.71
Putrescible	1.2
Paper	0.4
Glass	-
Metals	0.01
Textiles	0.3
Others	-
Total	3.52

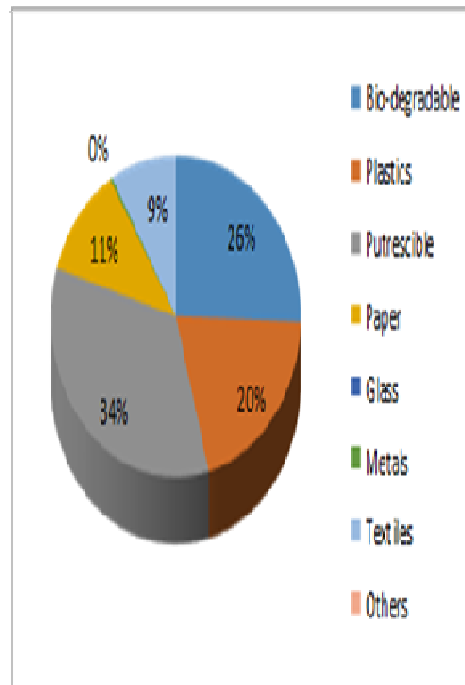


Figure 4. Solid waste generation

2.2.5. Case study 2: The two households close to the formal cattle market

From Fig.5a-b below shows the waste generated portrays the difference in living standards of the households. The itinerant cart-pushers gather waste (which could include solid wastes of more than one household) in Jute bags from clients as the vendor moves from house to house soliciting for more waste (Plate 1).

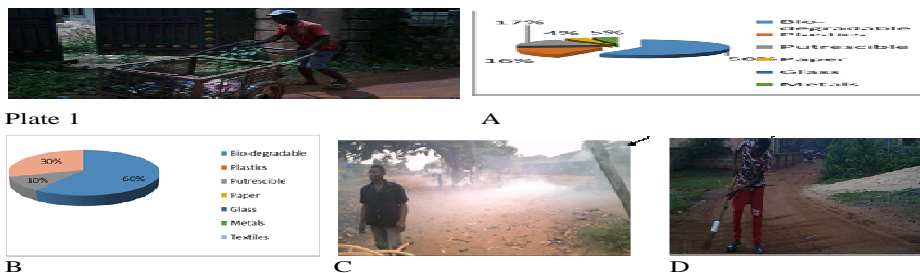


Plate 1. Push-cart vendor during operation, solid waste generation at Aideyamba (a), solid waste generation at cattle market (b), open-air burning of solid waste (c), and compound sweeping (d).

3. Results and discussion

The satellite images in Figure 3 shows that the total built area increased 58% from 4155 to 6552 hectares over a 20-year period and a corresponding decrease in vegetation cover of almost 100%. The expansion of housing units reflects increased urbanisation and population migration from the hinterland to Benin City, the state capital. As expected, the demand for available spaces for other activities apart from housing has increased astronomically with the almost non-availability of vacant land for future expansion. As a result, street corners, public open spaces, trench/burrow pits/ dug-out moats have become alternative spaces for waste disposal by residents (Figure 4 and 5a). Given this scenario, and coupled with the inability of the municipality to cope with waste management provision, previously protected areas have been exposed to indiscriminate waste disposal. This arrangement suggests that residents are no longer restrained from generating and disposing waste indiscriminately to the detriment of the environment. Thus, the results corroborate Tedeschi *et al.* (1971) study that if there exist such constraints people are likely to pollute their environment even when their belief systems tell them otherwise, thus manifesting a clear example of cognitive dissonance. Given this lack of restraint, disorder is bound to spread.

While waste is dumped indiscriminately in public open spaces, the current study found that there are exceptions in individual homes and places of worship. From the action focus (orthopraxy) perspective, we can argue that since most of the residents are somewhat religious, they tend to obey personalities, authorities and comply with laid down rules and regulations which is why they do not desecrate certain places. This position supports Alcorta and Sosis (2005) observations that ritual, emotion and holy symbols find spatial, emotional and behavioural dimensions and adaptations- that residents adapt to what they see as long as body, brain and environment are in agreement-embodiment.

Age, gender and kinship expectations, which form the basis for assigning roles and responsibilities within the family and community, are at present complimented by push-cart operators and itinerant scavengers. Informal waste-pickers have emerged from the over urbanisation of and population explosion in Benin City. This fact correlates with studies by Wilson *et al.* (2009) who argue that as the population escalates a fraction of the people will engage in some of the informality to make a living. The definition of age, gender and kinship nexus comprise part of the "in-group", and at the same time, "out-group" categories, as it possesses a more encompassing definition than otherwise known. Therefore, since there exists roles and responsibilities predicated on gender, age and kinship considerations the issue of "us" and "them" will continue even within the nuclear family.

4. Conclusion

The study focused on the interrelationships between changes in the environment of physical spaces and residents' attitudes through the lens of religion, psychology and phenomenology/neurophenomenology in Urora. Urbanisation, population explosion and erosion of community values were revealed to be responsible for the desecration of spaces that were once held as sacred. Given the existential-phenomenological view that humans do not stay in their actualities but in their possibilities, the language of communication and expression have been modified to adjust to the general situation-as language is far removed from its meanings. Given the advantages and potentials presented by the research community, there is every possibility that a realignment and reconsideration of their embodied sacred nature with the mode of expression of the past be advocated for human-human-environment sustainability. The language was seen as purposely led, ordered and conditioned. Rather than being repulsed by the activities of polluters, it appears community leaders are sympathetic to people with filthy tendencies and overwhelmed by these happenings as other residents pretend as if nothing has happened. In post-colonial African urban centres, the phenomena explored in this study appear to find spatial expression as the indigenous community which play host to other residents tend to be heterogeneous in outlook.

Acknowledgment. I greatly thank my lovely wife for her show of understanding. In addition, I appreciate the contributions carried out by Engr. Olotu Yahaya.

References

- [1] Adesanmi P., You're not a country, Africa. *A personal history of Africa present*, Penguin Books, Random House South Africa, 15(3), 2011, pp. 322-358.

- [2] Ajala A.S., *Space, identity and health risks*. University of Pittsburgh, USA 2017. <http://hcs.pitt.edu>, Accessed 12 July 2017.
- [3] Alcorta C.S., Sosis R., Ritual, Emotion, and Sacred symbols, *Human Nature*, 16(4), 2005, pp. 323-359.
- [4] Becker A.L., Language and Linguaging, *Language and Communication*, 11(2), 1991, pp.33-35.
- [5] ESMLH., Bulletin of Edo State geographical location, *DIVA-GIS and Edo State Ministry of Lands Surveys*, 20(2), 1990, pp.400-415.
- [6] Iyawe H., Place attachment and pro-environmental behaviour paralysis: A study of household solid waste management, *Journal of Construction Project Management and Innovation*, 9(1), 2019, pp. 72-84.
- [7] Medina M., Scavenging cooperatives in Asia and Latin America. *Resource conservation recycling*, 31(2), 2000, pp 51-69.
- [8] Millar D., Kendie S.B, Apusigah A.A, Haverkort B., African knowledge and Sciences: Understanding and supporting the ways of knowing in Sub-Saharan Africa, *Compass series on Worldviews and Sciences 3 Papers and Proceedings of an International Conference of African Knowledges and Sciences*. Oct. 23-29, 2005, Bolgatanga U/R Region Ghana, pp. 40-50.
- [9] Ogu V.I., Waste management in Benin City: Private sector and municipal waste management in Benin City Nigeria, *Environment & Urbanization*, 12(2), 2000, pp. 103-117.
- [10] Ojedokun O., Balogun S.K., Self-monitoring and responsible environmental behaviour: The mediating role of attitudes towards littering, *Frontiers in Psychological and Behavioural Science*, 2(1), 2013, pp.31-38.
- [11] Palfreyman D., Othering in an English language program, *TESOL Quartely*, 39(2), 2005, pp.211-233.
- [12] Tedeschi J.T., Schlenker B.R., Bonoma T.V., Cognitive Dissonance: Private ratiocination or public spectacle? *American Psychologist*, 26(3), 1971, pp. 685–695.
- [13] Wilson D.C., Araba A.O., Chinwah K., Cheeseman C.R., Building recycling rates through the informal sector, *Waste Management*, 29(2), 2009, pp.629-635.
- [14] Zabus C., Othering the foreign language in the West African Europhone Novel, *Canadian Review of Comparative Literature*, 21(3), 1990, pp.450-455.

Address:

- Dr. Hope Iyawe, Department of Urban & Regional Planning, Auchi Polytechnic, Auchi, Edo State, Nigeria: hopeiyawe2@gmail.com
(* corresponding author)

Opportunities to tackle apathy in solid waste management in rural integrated urban environment: The case of the Urora community in Benin City, Nigeria

Hope Iyawe, Obas John Ebohon*

In sub-Saharan African countries, there exists apathy towards solid waste management and services. Indiscriminate waste disposal in Urora is addressed through a recent study which uses a combination of concepts from the sense of community, empowerment and phenomenological principles to explore how to engage households with other stakeholders to address the disconnect that has resulted in environmental degradation. The findings revealed that the problem of indiscriminate waste disposal in this community could not be meaningfully understood without understanding their communal living, behaviour and practices as mediated by rituals unmitigated by passage of time. Based on these results, this paper argues that 'living in the community' means taking an active part in the settlement's physical environments for effective income generating opportunities.

Keywords: *Apathy, Community, Empowerment, Ritual, Solid Waste Management*

1. Introduction

Indiscriminate waste disposal is a pervasive problem across cities of developing countries (Medina, 2010; UN-Habitat, 2010; Guerrero, *et al.*, 2013). Solid wastes are variously defined and they manifest in various form but common identifiable characteristics. Solid wastes could be garbage, refuse, sludge from a wastewater treatment plant, water supply treatment plant, or air pollution control

facility and other discarded materials including solid, liquid, semi-solid, or contained gaseous material, resulting from industrial, commercial, mining and agricultural wastes.

Several factors account for indiscriminate disposal of solid wastes, this includes the collapse of the traditional waste management systems, rapid rates of urbanisation unmatched by commensurate infrastructure and services, and above all, poor attitudes to waste management across society, including households and businesses (Addaney and Oppong, 2015). Global solid wastes generation is projected to escalate rapidly by 2050, jumping from 2.01 billion tonnes in 2016 to 3.4 billion tonnes by 2050. Daily per capita waste generation is found to be highest in high income or developed economies, this is projected to rise by 19 % by 2050. The low to middle income countries will experience the highest per capita solid waste generation, this is projected to increase by more than 40 %. According to the World Bank (2018), this comes as no surprise as waste generation was generally found to increase at a faster rate for incremental income changes at lower income levels than at high-income levels. The total quantity of waste generated in low-income countries is expected to increase by more than three times by 2050.

Several factors have been adduced for the growth trend in solid wastes (Mighua *et al.*, 2009, Burntley, 2007). Indeed, increasing population, economic growth, increase in living standards and rapidly changing lifestyles, and rapid urbanisation have been identified as significant factors underpinning acceleration in solid wastes production (Minghua *et al.*, 2009). Observable global trend shows that as countries achieve accelerated economic growth and development, particularly where the proceeds of such growth is equitably distributed, not only will lifestyles and pattern of consumption begin to change, also, the quantity and format of good and services consumed will begin to change (Bello, 2016). Other implicit factors contributing to solid wastes generations include inadequate organizational and institutional management and building capacities (Douti *et al.*, 2017; Oteng-Ababio *et al.*, 2013), which is exacerbated by the narrow capital base effect solid waste management systems and processes (Burntley, 2007; UN Habitat, 2010).

However, while these factors generally apply to the analysis of solid wastes across countries, analysing them within a country-specific context allows policies to be tailored to country peculiarities, taking on board the socio-cultural elements and dimension to solid wastes generation. In particular, the roles of communities, which serves as critical agents of change in mechanical societies, as represented at local levels in developing countries, can best be ascertained by seeking local solutions at relevant scales to global solid wastes problems. Doing so will further accomplish two things, firstly, it will deepen the interests of local communities in solid wastes. Secondly, it will also bridge capacity gaps both in terms of financial and human capital resources by opening up participatory opportunities for solid wastes management at local levels.

A key contributory factor to waste generation is the current and traditional linear extract-produce-use-dump (throughput flow model) material and energy flow that has been popular with the modern economic system but unsustainable (Korhonen *et al.*, 2017; Frosch and Gallopoulos, 1989). Accordingly, the flow runs down the system where it operates, where it takes its source and where it releases its wastes. To stem its tide, a circular/sharing economic system with a cyclical, alternative flow is advocated; this economic system emphasises product, material reuse, repair, refurbishing, biomass, wind solar and waste-derived energy throughout the product value chain (leung, *et al.*, 2019; Korhonen, *et al.*, 2017; Mihelcic *et al.*, 2003; Rashid *et al.*, 2013). The sense of community and empowerment requires the conscious and fruitful combination of body, brain and environment which is possible through phenomenological study (see Figure 1). Phenomenology is an attempt to understand, adequately describe, analyse and interpret the consciousness and lived experience of an actor without addition or subtraction (Wertz *et al.*, 2011). Therefore, phenomenology is a philosophy and a research method designed to explore and understand people’s everyday lived experiences through the use of the three variables of intentionality, perception and embodiment of research subjects.

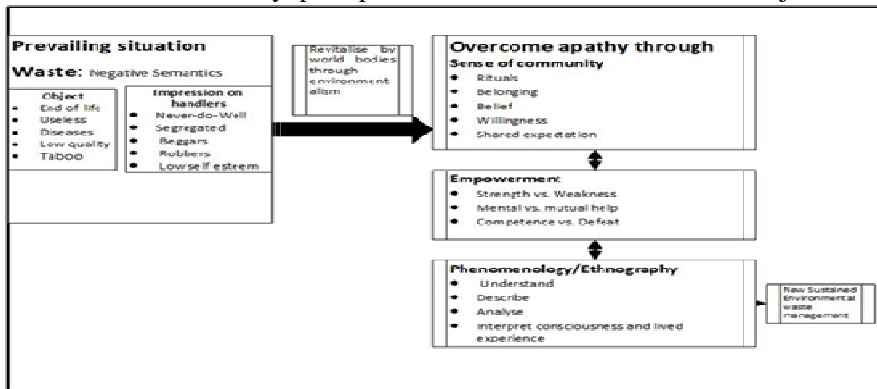


Figure 1. Conceptual Mapping of Apathy and Opportunities of Indiscriminate Waste Discourse

2. Research methodology

2.1. Study area: Urora

Urora lies between latitudes 60 22'04", 60 22'43" N and longitudes 50 41'11", 50 42'23" E with a population of 48 219 (2018 estimate projected from the 2006 National Population Census). However, the study location has been engulfed by Benin City, the state capital, due to population explosion especially arising from rapid urbanisation (see Figure 3). Figure 3 shows the map of Edo state showing Ikpoba-Okha where the Urora community is located. Administratively, Urora falls under the Benin Kingdom, the King or the Oba is the ultimate traditional authority

to whom all traditional leaders' reports. In other words, all traditional rulers, the Enigies in the Benin Kingdom, are hierarchically subordinate to the Oba. Additionally, Urora has a traditional priest (Ohen). Traditionally, and also for contemporary administrative convenience, the community is sub-divided into three quarters, namely Urora I (Ohen quarters), Urora II (across the Benin-Okene-Abuja highway), and Urora III (Aideyanba Quarters). Each of these quarters has their local traditional head as chiefs or Ohen. By the 1999 constitution, and as it is the case in many parts of the world, municipal waste management and service operations are executed by local councils or local authorities (Rotich *et al.*, 2006). The capacity of local authorities to function effectively in this role predicated upon their capital base, particularly the scope for local income generation through local taxations and ability to borrow from the capital market. As it is the case the world over, the ability of local authorities to raise revenue through taxation and access the capital market is severely restricted by national governments. In the particular case of Nigeria, local authorities or Councils are politically and economically emasculated by State Governments.

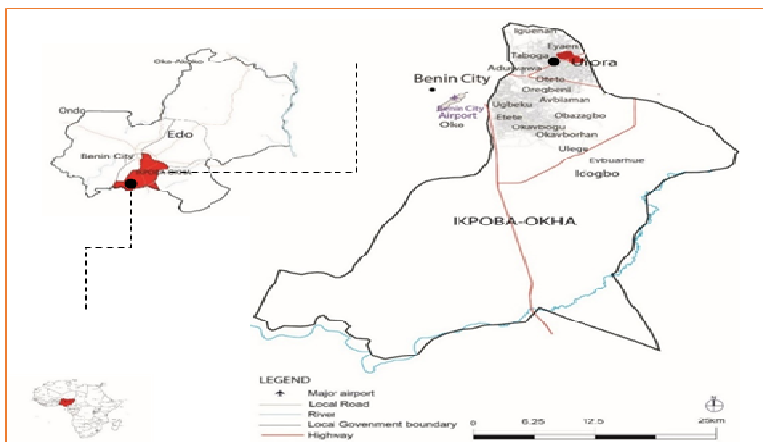


Figure 2. Source: Adapted and modified from DIVA-GIS and Edo State Ministry of Lands Surveys

Data for the study were collected as part of a more extensive research conducted throughout 4 months between late November 2016 to early March 2017 and 7-21 July 2017. The study has four main stages: *Stage 1* involve GPS in order to produce an updated base map with readings of meaning-making features of the settlement as none was readily available. The primary data collection stage of the study was facilitated by a resident gate-keeper/key informant who guided the researcher around to see the settlement. Secondly, the researcher visited locations like the Ogua-edion (elders' sanctuary), shrines, sacred groves and unauthorised dump sites

(Figure 3). This visit includes the names and different locations of worship centres in the settlement. *Stage 2* involved interviews with 3 key informants who have insights of happenings within and outside the community (Marshall, 1996) who have lived in the settlement for more than ten years (Kyle and Chick, 2007). Questions revolved around social mechanism of waste-disposal patterns and related attitudes in connection with waste generation and management. In selecting the key informants, the study used the purposeful sampling technique to select them based on the recommendations of community members - the second-person phenomenological interview method as elaborated upon by Olivaires *et al.* (2015) to interview the key informants. The study undertook direct observation through participation in ceremonies such as marriages, burials and church programmes at households and community platforms while maintaining the status of observer-as-participant (Marshall, 1996). In *Stage 3*, the researcher conducted interviews with twenty focus group discussants who provided insight into the impassivity of the waste phenomenon in the settlement and beyond.

2.2. Data analysis

The study used Colaizzi (1978) phenomenological study in analysing participants transcripts. This method is subdivided into five steps:

- Read and re-read each transcript to have a general picture about the unfolding episode through bracketing of ideas, thoughts and feelings.
- For each transcript, the significant statements that concern resident apathy and opportunities stem impassivity is emphasised and thereby derive meaning units from the statements.
- Cluster the meaning units into themes and categories.
- Place findings of the study into an exhaustive description of the phenomenon of apathy and opportunities.
- Describe the fundamental structure of the phenomenon and approach the participants a second time to validate the researcher's descriptive results with their experiences.

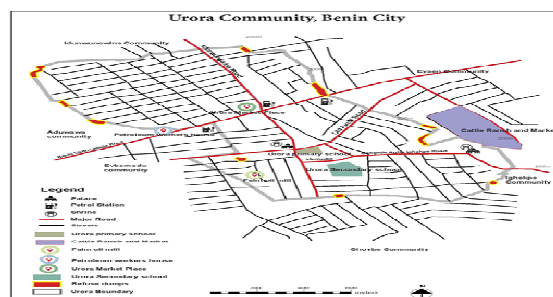


Figure 3. Urora community and urban feature. Source: Author field survey, 2016

Table 4. Statement of significance and formulated meaning

Significant Statements	Meaning Unit
<p>Question: Describe your experience or encounter with living together in the community, as to roles and responsibilities with solid waste disposal/management process from generation at home to disposal at the public open space?</p> <p>Response: In my house we have division of labour and responsibilities; males and females perform separate functions so also with the age of members of the family. For waste matters, my wife and children undertake that responsibility especially when the waste in the house are from the kitchen. Females take care of the homes while my children depending on their age assist my wife in doing the house chores. They gather the waste in and around the house as they take turn on weekly basis. This arrangement does not include those serving punishment for which they could be punish through the clearing waste for the period the punishment would last. This practice is passed down the generation and so become institutionalised. Wastes emit petrifying odours, particularly where they are organic and exposed to serious weather conditions such as extreme heat and wet seasons. After collection, we use the bucket or the wheelbarrow depending on the quantity to convey the waste to the moat.</p> <p>Question: How regular is the solid waste generated and disposed of from your household?</p> <p>Response: After we gather the waste in a disused container for about three days, they are transported in a wheelbarrow to the nearest dumpsite, others with backyard waste dumps avail themselves on daily basis as the remainder makes use of the push-cart vendors</p> <p>Question: Why would residents be disinterested with waste products?</p> <p>Response: To us, solid wastes are useless, condemned, and discarded dirty rubbish, and why would anyone want to be associated with it. In the local language, the '<i>Ihuen</i>' '<i>Iku</i>' – these are derogatory terms that no one wants to be associated. Besides, wastes breed disease-carrying vectors such as flies, rodents, cockroaches that contaminate food and cause diseases.</p>	<p>Home division of labour based on age and gender consideration</p>

3. Results and discussion

Given that the study undertook a combination of ethnographic and phenomenological studies, three broad themes/results are discernible-

- Residents apathy towards waste management is rooted in social and cultural norms which residents have been accustomed.
- Certain waste products have value and can form the basis of income-generating opportunities for households, if oriented towards that goal. However, given the stigma attached to anyone or anything associated with solid wastes in the community, considerable doubts remain whether such initiative will attract anyone from the community.
- To achieve continued success in the settlement and elsewhere there must be a stakeholders' dialogue between all stakeholders, including religious and community leaders, residents, governments, waste managers and prospective private sector investors.

Urora residents associates wastes with stigmas see the presence of waste and connotations regarding waste as a taboo and to avoid its occurrence. An average household in the locality has an internal division of labour along the lines of gender and age considerations (see Table 4) - this position further alienates most of the residents from participating in the waste management or disposal service as it is considered menial tasks to be left to the children. Further, the stigmas associated with waste and wastes handlers also exacerbate solid wastes problems in Urora. These findings corroborate those of Medina (2000) and Fahmi (2006) found for Asia and Latin America respectively that the stigmas attached to solid wastes are a major hindrance to sustainable solid wastes management.

The sense of community is instructive in its emphasis that the community as an entity endures while individuals come and exit the community. The implication being the importance of embedding sustainable wastes management into communities in terms of norms and values so that those who come in or exit the community buy into the value or take the value with them where ever they go. This encourages both the present and future generations of residents to imbibe community values, which comes to them as a way of life. This will persist irrespective of their ethnic and religious colourations. The absence of waste repositories is a huge constraint on sustainable wastes management, forcing residents to dispose their waste openly on uninhabited lands, road junctions, burrow pits and moats. Given the vagaries of the weather between wet and dry seasons, improper or indiscriminate disposal of solid wastes poses huge environmental hazards to the Urora community. A common feature of indiscriminate solid wastes disposal in Urora is the proliferation of the non-degradable wastes such as plastics, which the community could seize upon to make paving slabs (Kumilarbi *et al.*, 2018).

A significant source of opportunity yet to be tapped is the waste from the herds of cattle at the cattle ranch/market. This category of waste continues to pose prob-

lems for the community given the free-range of the heads and the damage to farmlands and gardens in the process and the droppings spread indiscriminately to create environmental nuisance of smell and unsightliness. However, with appropriate technology and know-how, the droppings from the cattle can be used for composting to increase the yield of agricultural produce. Aside, these organic wastes are a ready source of renewable energy for cooking. Indeed, studies by Rao *et al.*, (2010) and Cuellar and Webber (2008) have ascertained this type of wastes can be processed through anaerobic digestion into methane gas suitable for cooking.

Also evident from the results is the current rudimentary practice of using pushcart vendors for waste collection from households and those that scavenge for indiscriminately disposed waste products of intrinsic value for resale, indicating huge scope for a circular economy. However, such subsistence approach to solid waste management has proved unsustainable owing to the increasing rate of solid wastes generation. This is corroborated by the huge amounts of solid wastes left unattended and burnt openly with huge pollution effects. Evident from the fieldwork is the presence of various ethnic nationalities in Nigeria reside in the community, including the *Benins*, the *Esans*, the *Ibos*, the *Hausas*, the *Fulanis* and the *Urhobos* among others. These ethnic nationalities are of different religious backgrounds and they meet regularly to foster inter-communal unity and cooperation. This provides an effective platform for the community to strategise and formulate effective solid wastes policies that the community can take full ownership. Such a strategy could involve a community recycling depot, which will offer employment and income generating opportunities (Wilson, *et al.*, 2006)⁵.

The community-scale solid waste management intervention is critical to sustainable waste management. Sensitising the community about the hazards posed by indiscriminate solid wastes disposal empowers people to protect their own and family's health. The community waste management strategy should focus more on wastes reduction, reuse, recycle, recover, and less on disposal.

4. Conclusion

The objectives of the study were to explore and understand the apathy towards responsible disposal of solid wastes in Urora community; to explore the scope for generating employment and income generating opportunities for the Urora community from sustainable solid wastes management and to explore the reasons behind the low solid wastes collection and processing in Urora and the role of culture in effecting sustainable solid wastes management.

These objectives have been fulfilled, the study shows that the apathy towards indiscriminate solid wastes disposal in Urora is as a result of lack of effective wastes management strategies, policies, and infrastructure. Above all, the stigma attached to solid wastes is a major deterrence to households associating with solid

wastes despite the employment and income generating opportunities in existence but not seized upon. What the study also shows is the pivotal role community and religious leaders have to play in reversing the stigma attached to solid wastes management in communities such as Urora.

Acknowledgment. I greatly thank my lovely wife for her show of understanding. In addition, I appreciate the contributions carried out by Engr. Olotu Yahaya.

References

- [1] Addaney M., Oppong, R. A., Critical Issues of Municipal Solid Waste Management in Ghana, *JENRM*, 2(1), 2015, pp. 30-36.
- [2] Bello H., Impact of Changing Lifestyle on Municipal Solid Waste Generation in Residential Areas: Case Study of Qatar, *International Journal of Waste Resources*, 8(2), 2018.
- [3] Burntley S.J., A review of municipal solid waste composition in the United Kingdom. *Journal of Waste Management*, 27 (3), 2007, pp. 1274 -1285.
- [4] Collaizzi P.F., Psychological research as the phenomenologist views it. In R. Vaile&M. Kings (Eds.), *Existential-phenomenological alternatives for psychology*. Oxford University Press, 1978, (pp. 48-71).
- [5] Cuellar A.D., Webber M.E., Cow power: the energy and emissions benefits of converting manure to biogas. *Environmental Research Letters*, 3 (1), 2008, pp. 40-43.
- [6] Douiti N.B., Abanyie S.K., Ampofo S., Solid Waste Management Challenges in Urban Areas of Ghana: A Case Study of Bawku Municipality, *International Journal of Geosciences*, 8(1), 2017, pp. 494-513.
- [7] Fahmi W.S., The impact of privatisation of solid waste management on the Zebaleen garbage collectors of Cairo, *Environmental Urban*, 17(2), 2006, pp.155-170.
- [8] Frosch D., Gallopoulos, N., Strategies for Manufacturing, *Scientific American*, 261 (3), pp.144-152.
- [9] Guerrero, L.A., Maas G., Hogland, W., Solid waste management challenges for cities in developing countries. *Waste Management*, 33(1), 2013, pp. 220-232.
- [10] Korhonen J, Honkasalo A, Seppala J., Circular economy: The concept and its limitations, *Ecological Economics*, 143(2), 2017, pp. 37-46
- [11] Kumi-Larbi A., Yunana D., Kamsouloum P., Webster M., Wilson D.C., Cheeseman C., Recycling waste plastics in developing countries: Use of low-density polyethylene water sachets to form plastic bonded sand blocks, *Waste Management*, 80(4), 2018, pp. 112-118.

- [12] Leung X.Y., Xue L., Wen H., Framing the Sharing economy: Towards a sustainable ecosystem, *Tourism Management*, 71(3), 2019, pp. 44-53.
- [13] Marshall M.N., The key informant technique, *Family Practice*, 13(1), 1996, pp. 92-97.
- [14] Medina M., Solid Wastes, Poverty and the Environment in Developing Country Cities: Challenges and Opportunities. United Nations University, World Institute for Development Economics Research, Working Paper No. 2010/23.
- [15] Mihelcic J.R., Crittenden J.C., Small M.J., Shonnard D.R., Hokanson D.R., Zhang Q., Chen H., Sorby S.A., James V.U., Sutherland J.W., Schnoor J.I., Sustainability Science and Engineering: The emergence of a new metadiscipline, *Environmental Science and Technology*, 3(2), 2003, pp. 5314-5324.
- [16] Minghua Z., Xiumin F., Rovetta A., Qichang H., Vicentini F., Bingkai L., Guisti A., Yi L., Municipal solid waste management in Pudong new area, China, *Journal of Waste Management*, 29 (3), 2009, pp.1227 - 1233.
- [17] Oteng-Ababio M., Arguello J.E.M., Gabby O., Solid waste management in African cities: Sorting the facts from the fads in Accra, Ghana. *Habitat International*, 39 (3), 2013, pp. 96-104.,
- [18] Rao P.V., Baraj S.S., Dey R., Mutnuri S., Biogas generation potential by anaerobic digestion for sustainable energy development in India, *Renewable and Sustainable Energy Reviews*. 14(7), 2010, pp.2086-2094.
- [19] Rotich K.H., Zhao Y., Dong J., Municipal solid waste management challenges in developing countries – Kenyan case study, *Waste Management* 26(3), 2006, pp 92–100.
- [20] UN-Habitat., Solid Waste Management in World Cities: Water and Sanitation in the World Cities, *Earthscan Publishing, London & Washington*, 14(3), 2010, pp. 92-97.
- [21] Wertz F.J., McMullen L.M, Josselson R., Anderson R., McSpadden E., Five ways of doing qualitative analysis; phenomenological psychology, grounded theory, discourse analysis, narrative research, and intuitive inquire. *The Guilford Press, New York, USA*, 6(2), 2011, pp.40-44.

Addresses:

- Dr. Hope Iyawe, Department of Urban & Regional Planning, Auchi Polytechnic, Auchi, Edo State, Nigeria, hopeiyawe2@gmail.com
- Prof. Obas John Ebohon, Center for Sustainability & Resilient Infrastructure and Communities, School of The Built Environment and Architecture, London South Bank University, London, SE1 0AA''
(* corresponding author)

Heat absorption and Hall current effects on unsteady MHD flow past an inclined plate

Gaurav Kumar*, S.M.K. Rizvi, Amresh Kumar

In the present paper, we study the effect of heat absorption on unsteady flow of a viscous, incompressible, electrically conducting fluid past an impulsively started inclined plate with variable wall temperature and mass diffusion in the presence of transversely applied uniform magnetic field and Hall current. Earlier we analyzed the effects of radiation and chemical reaction on MHD flow past a vertical plate with variable temperature and mass diffusion. We had obtained the results which were in agreement with the desired flow phenomenon. To study further, we are changing the model by considering heat absorption on fluid, and changing the geometry of the model. Here in this paper we are considering the plate positioned inclined from vertically plane and impulsively started with velocity u_0 . The temperature of plate and the concentration level near the plate is increase linearly with time. The governing equations involved in the present analysis are solved by the Laplace-transform technique. The results obtained have been analyzed with the help of graphs drawn for different parameters like thermal Grashof number, mass Grashof Number, Prandtl number, permeability parameter, Hall current parameter, heat absorption parameter, magnetic field parameter and Schmidt number. The numerical values obtained for skin-friction and Nusselt number have been tabulated. The results are found to be in a good agreement and the data obtained is in concurrence with the actual MHD fluid flow phenomenon.

Keywords: MHD flow, heat absorption, inclined plate, variable temperature, mass diffusion, Hall current.

1. Introduction

The effect of heat absorption on MHD with heat and mass transfer is of great importance in many applications such as development of metal waste from spent

nuclear fuel, fluids undergoing exothermic and endothermic chemical reaction, convection in Earth's mantle, post-accident heat removal, fire and combustion modeling etc. Hall effect on MHD mixed convective flow of a viscous incompressible fluid past a vertical porous plate immersed in porous medium with heat source was analyzed by Sharma et.al [11]. MHD-conjugate heat transfer analysis for a vertical flat plate in presence of viscous dissipation and heat generation was studied by Mamun et. al [5]. Shit and Haldar [8] have worked on combined effects of thermal radiation and Hall current on MHD free-convective flow and mass transfer over a stretching sheet with variable viscosity. Radiation effect on MHD free convection flow along vertical flat plate in presence of Joule heating and heat generation was proposed by Alia et.al [1]. Seth et.al [10] have investigated numerical solution of unsteady hydromagnetic natural convection flow of heat absorbing fluid past an impulsively moving vertical plate with ramped temperature. Tanvir and Alam [12] have worked on finite difference solution of MHD mixed convection flow with heat generation and chemical reaction. Unsteady hydromagnetic flow of a heat absorbing dusty fluid past a permeable vertical plate with ramped temperature was analyzed by Das et.al [2]. Stanford and Gerald [9] have studied on a new numerical analysis of the Hall effect on MHD flow and heat transfer over an unsteady stretching permeable surface in the presence of thermal radiation and heat source. Chemical reaction effect on unsteady MHD flow past an impulsively started oscillating inclined plate with variable temperature and mass diffusion in the presence of Hall current was presented by Rajput and Kumar [6]. Further, Rajput and Kumar [7] have worked on effects of radiation and chemical reaction on MHD flow past a vertical plate with variable temperature and mass diffusion. Kumar along with Bansal [3] have considered unsteady flow past on vertical cylinder in the presence of an inclined magnetic field and chemical reaction. Chemical reaction effect on MHD flow past an impulsively started vertical cylinder with variable temperature and mass diffusion was studied by Kumar et.al [4]. This paper deals with an analysis of effects of heat absorption and Hall current on unsteady flow past an impulsively started inclined plate in the presence of transversely applied uniform magnetic field with heat and mass transfer. The problem is solved analytically using the Laplace Transform technique. A selected set of graphical results illustrating the effects of various parameters involved in the problem are presented and discussed. The numerical values of skin-friction have been tabulated.

2. Mathematics Analysis.

The geometric flow model of the problem is shown in Figure-1. The unsteady flow of an electrically conducting, viscous, incompressible and heat absorbing fluid past an impulsively started inclined plate with variable wall temperature and mass diffusion in the presence of Hall current has been considered. The x axis is taken

along the vertical plane and z axis is normal to it. Thus the z axis lies in the horizontal plane. The plate is inclined at angle α from vertical. The magnetic field B_0 of uniform strength is applied perpendicular to the flow. Further, the angle of inclination changes then the magnetic field changes its direction, such that it always remains perpendicular to it. Thus the direction of magnetic field is tied with the plate. Initially it has been considered that the plate as well as the fluid is at the same temperature T_∞ . The species concentration in the fluid is taken as C_∞ . At time $t > 0$ the plate starts moving with velocity u_0 in its own plane and temperature of the plate are raised to T_w . The concentration C near the plate is raised linearly with respect to time.

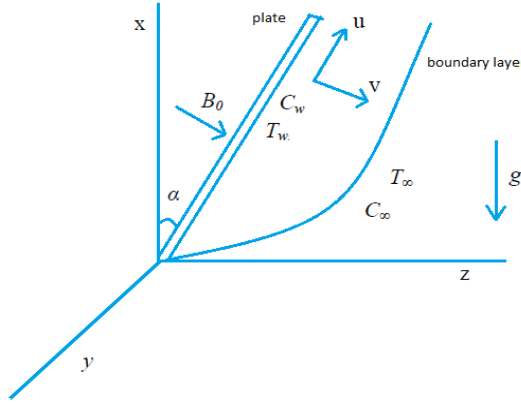


Figure 1.

Then under these assumptions and the Boussinesq's approximation, the flow is governed by the following system of equations:

$$\frac{\partial u}{\partial t} = \nu \frac{\partial^2 u}{\partial z^2} + g\beta \cos\alpha (T - T_\infty) + g\beta^* \cos\alpha (C - C_\infty) - \frac{\sigma B_0^2 (u + mv)}{\rho(1 + m^2)}, \quad (1)$$

$$\frac{\partial v}{\partial t} = \nu \frac{\partial^2 v}{\partial z^2} + \frac{\sigma B_0^2 (mu - v)}{\rho(1 + m^2)}, \quad (2)$$

$$\frac{\partial C}{\partial t} = D \frac{\partial^2 C}{\partial z^2}, \quad (3)$$

$$\rho C_p \frac{\partial T}{\partial t} = k \frac{\partial^2 T}{\partial z^2} - Q(T - T_\infty). \quad (4)$$

The following initial and boundary conditions are

$$\left. \begin{aligned}
 t \leq 0 : u = 0, v = 0, T = T_\infty, C = C_\infty, \text{ for all } z, \\
 t > 0 : u = u_0, v = 0, T = T + (T_w - T_\infty) \frac{u_0^2 t}{v}, C = C_\infty + (C_w - C_\infty) \frac{u_0^2 t}{v}, \text{ at } z = 0, \\
 u \rightarrow 0, v = 0, T \rightarrow T_\infty, C \rightarrow C_\infty \text{ as } z \rightarrow \infty.
 \end{aligned} \right\} (5)$$

Here u and v are the primary and secondary velocities, g - the acceleration due to gravity, β - volumetric coefficient of thermal expansion, t - time, $m(=\omega_e \tau_e)$ is the Hall current parameter with ω_e - cyclotron frequency of electrons and τ_e - electron collision time, T - temperature of the fluid, β^* - volumetric coefficient of concentration expansion, C - species concentration in the fluid, ν - the kinematic viscosity, ρ - the density, C_p - the specific heat at constant pressure, k - thermal conductivity of the fluid, D - the mass diffusion coefficient, T_w - temperature of the plate at $z = 0$, Q - heat absorption coefficient C_w - species concentration at the plate $z = 0$, B_0 - the uniform magnetic field, σ - electrical conductivity.

The following non-dimensional quantities are introduced to transform equations (1), (2), (3) and (4) into dimensionless form:

$$\left. \begin{aligned}
 \bar{z} = \frac{z u_0}{v}, \bar{u} = \frac{u}{u_0}, \bar{v} = \frac{v}{u_0}, \theta = \frac{(T - T_\infty)}{(T_w - T_\infty)}, S_c = \frac{v}{D}, \mu = \rho \nu, \\
 P_r = \frac{\mu C_p}{k}, H = \frac{Q \nu}{u_0^2 \rho C_p}, G_r = \frac{g \beta \nu (T_w - T_\infty)}{u_0^3}, M = \frac{\sigma B_0^2 \nu}{\rho u_0^2}, \\
 G_m = \frac{g \beta^* \nu (C_w - C_\infty)}{u_0^3}, \bar{C} = \frac{(C - C_\infty)}{(C_w - C_\infty)}, \bar{t} = \frac{t u_0^2}{v}.
 \end{aligned} \right\} (6)$$

The symbols in dimensionless form are as under:
 \bar{u} is the primary velocity, \bar{v} - the secondary velocity, \bar{t} - time, θ - the temperature, \bar{C} - the concentration, G_r - thermal Grashof number, G_m - mass Grashof number, μ - the coefficient of viscosity, P_r - the Prandtl number, S_c - the Schmidt number, H - heat absorption coefficient, M - the magnetic parameter.

Thus the model becomes:

$$\frac{\partial \bar{u}}{\partial \bar{t}} = \frac{\partial^2 \bar{u}}{\partial \bar{z}^2} + G_r \cos \alpha \theta + G_m \cos \alpha \bar{C} - \frac{M(\bar{u} + m \bar{v})}{(1 + m^2)}, \quad (7)$$

$$\frac{\partial \bar{v}}{\partial \bar{t}} = \frac{\partial^2 \bar{u}}{\partial \bar{z}^2} + \frac{M(m \bar{u} - \bar{v})}{(1 + m^2)}, \quad (8)$$

$$\frac{\partial \bar{C}}{\partial \bar{t}} = \frac{1}{S_c} \frac{\partial^2 \bar{C}}{\partial \bar{z}^2}, \quad (9)$$

$$\frac{\partial \theta}{\partial \bar{t}} = \frac{1}{P_r} \frac{\partial^2 \theta}{\partial \bar{z}^2} - H\theta. \quad (10)$$

The corresponding boundary conditions become:

$$\left. \begin{array}{l} \bar{t} \leq 0 : \bar{u} = 0, \bar{v} = 0, \theta = 0, \bar{C} = 0, \quad \text{for all } \bar{z}, \\ \bar{t} > 0 : \bar{u} = 1, \bar{v} = 0, \theta = \bar{t}, \bar{C} = \bar{t}, \quad \text{at } \bar{z} = 0, \\ \bar{u} \rightarrow 0, \bar{v} \rightarrow 0, \theta \rightarrow 0, \bar{C} \rightarrow 0, \quad \text{as } \bar{z} \rightarrow \infty. \end{array} \right\} \quad (11)$$

Dropping bars in the above equations, we get:

$$\frac{\partial u}{\partial t} = \frac{\partial^2 u}{\partial z^2} + G_r \cos \alpha \theta + G_m \cos \alpha C - \frac{M(u + mv)}{(1 + m^2)}, \quad (12)$$

$$\frac{\partial v}{\partial t} = \frac{\partial^2 v}{\partial z^2} + \frac{M(mu - v)}{(1 + m^2)}, \quad (13)$$

$$\frac{\partial C}{\partial t} = \frac{1}{S_c} \frac{\partial^2 C}{\partial z^2}, \quad (14)$$

$$\frac{\partial \theta}{\partial t} = \frac{1}{P_r} \frac{\partial^2 \theta}{\partial z^2} - H\theta. \quad (15)$$

The boundary conditions are:

$$\left. \begin{array}{l} t \leq 0 : u = 0, v = 0, \theta = 0, C = 0, \quad \text{for all } z, \\ t > 0 : u = 1, v = 0, \theta = t, C = t, \quad \text{at } z = 0, \\ u \rightarrow 0, v \rightarrow 0, \theta \rightarrow 0, C \rightarrow 0, \quad \text{as } z \rightarrow \infty. \end{array} \right\} \quad (16)$$

Combining equations (12) and (13), the flow model becomes:

$$\frac{\partial q}{\partial t} = \frac{\partial^2 q}{\partial z^2} + G_r \cos \alpha \theta + G_m \cos \alpha C - q \left(\frac{M(1 - im)}{1 + m^2} \right), \quad (17)$$

$$\frac{\partial C}{\partial t} = \frac{1}{S_c} \frac{\partial^2 C}{\partial z^2}, \quad (18)$$

$$\frac{\partial \theta}{\partial t} = \frac{1}{P_r} \frac{\partial^2 \theta}{\partial z^2} - H\theta. \quad (19)$$

Finally, the boundary conditions become:

$$\left. \begin{aligned} t \leq 0 : q = 0, \theta = 0, C = 0, & \quad \text{for all } z, \\ t > 0 : q = 1, \theta = t, C = t, & \quad \text{at } z=0, \\ q \rightarrow 0, \theta \rightarrow 0, C \rightarrow 0, & \quad \text{as } z \rightarrow \infty. \end{aligned} \right\} \quad (20)$$

Here $q = u + i v$,

The dimensionless governing equations (17) to (19), subject to the boundary conditions (20), are solved by the usual Laplace - transform technique. The solutions obtained are as under:

$$\begin{aligned} C &= t \left\{ \left(1 + \frac{z^2 S_c}{2t} \right) \operatorname{erfc} \left[\frac{\sqrt{S_c}}{2\sqrt{t}} \right] - \frac{z\sqrt{S_c}}{\sqrt{\pi}\sqrt{t}} e^{-\frac{z^2}{4t} S_c} \right\}, \\ \theta &= -\frac{I}{4Hi} e^{-zi\sqrt{-HP_r}} \left\{ -2i\sqrt{-H}t(A_1 - e^{-zi\sqrt{-HP_r}} A_2 - 2) + z\sqrt{P_r}(A_1 + e^{-zi\sqrt{-HP_r}} A_2 - 2) \right\} \\ q &= \frac{I}{2} e^{-\sqrt{M(1-im)(1+m^2)^{-1}}z} A_{33} + \frac{G_r \operatorname{Cos} \alpha}{4} \left((M(1-im)(1+m^2)^{-1}) - HP_r \right)^{-2} \left[(M(1-im)(1+m^2)^{-1}t + P_r - HP_r t - I) \left(e^{-\sqrt{M(1-im)(1+m^2)^{-1}}z} A_3 - e^{-\sqrt{-HP_r}zi} A_{11} \right) \right. \\ &+ e^{-\sqrt{M(1-im)(1+m^2)^{-1}}z} A_4 \left(\sqrt{M(1-im)(1+m^2)^{-1}} - HP_r \left(M(1-im)(1+m^2)^{-1} \right)^{1/2} \right) \\ &+ A_{14}(I - P_r)(A_5 - A_{12}) - \frac{I}{2i\sqrt{-H}} z e^{-\sqrt{-HP_r}zi} A_{10} \sqrt{P_r} \left(-HP_r + \left(M(1-im)(1+m^2)^{-1} \right) \right) \left. \right] \\ &+ \frac{G_m \operatorname{Cos} \alpha}{4} \left(M(1-im)(1+m^2)^{-1} \right)^{-2} \left[2A_6 e^{-\sqrt{az}} (I - M(1-im)(1+m^2)^{-1}t) \right. \\ &+ e^{-\sqrt{M(1-im)(1+m^2)^{-1}}z} \left(z\sqrt{M(1-im)(1+m^2)^{-1}} A_8 + 2A_9 S_c \right) + 2A_{15} A_7 (I - S_c) \left. \right] \\ &+ \frac{G_m \operatorname{Cos} \alpha}{2\sqrt{\pi}} \left(M(1-im)(1+m^2)^{-1} \right)^{-2} \left[2 \left(M(1-im)(1+m^2)^{-1} \right) z\sqrt{t} S_c e^{-\frac{z^2 S_c}{4t}} \right. \\ &+ A_{16} \sqrt{\pi} \left(M(1-im)(1+m^2)^{-1} z^2 S_c + 2tM(1-im)(1+m^2)^{-1} + 2S_c - 2 \right) \\ &+ A_{13} A_{15} \sqrt{\pi} (I - S_c) \left. \right] \end{aligned}$$

The expressions for the constants involved in the above equations are given in the appendix.

Skin friction

The dimensionless skin friction at the plate $z=0$:

$$\left(\frac{dq}{dz}\right)_{z=0} = \tau_x + i\tau_y,$$

Separating real and imaginary part in $\left(\frac{dq}{dz}\right)_{z=0}$, the dimensionless skin friction component $\tau_x = \left(\frac{du}{dz}\right)_{z=0}$ and $\tau_y = \left(\frac{dv}{dz}\right)_{z=0}$ can be computed.

Nusselt number

The dimensionless Nusselt number at the plate $z=0$ is given by:

$$Nu = \left(\frac{\partial\theta}{\partial z}\right)_{z=0} = -t\sqrt{HP_r} + \frac{I}{4\sqrt{H}}((-2 + 2\text{erfc}[\sqrt{Ht}])\sqrt{P_r} - 2\sqrt{Ht}\left(\frac{2\exp(Ht)\sqrt{P_r}}{\sqrt{\pi}} - 2\text{erfc}[\sqrt{Ht}]\sqrt{HP_r}\right))$$

3. Results and Discussion

The velocity profiles for different parameters like thermal Grashof number (Gr), magnetic field parameter (M), Hall parameter (m), Prandtl number (Pr) and Heat absorption parameter (H) are shown in figures 1.1 to 2.8. The fluid flow with high velocity when plate is vertical and low velocity when plate is horizontal, It is observed from figures 1.1 and 2.1 that the primary and secondary velocities of fluid decrease when the angle of inclination (α) is increased. This is due to facts that fluid velocity depends on gravity components ($g\cos\alpha$). Figures 1.2, 2.2, 1.3 and 2.3 show the buoyancy effect, and it is observed that both the primary and secondary velocities increase on increasing thermal Grashof number G_r and mass Grashof number G_m . Therefore, it concludes that buoyancy force tends to accelerate primary and secondary velocities. Also, if Hall current parameter m is increased then u increases, while v gets decreased (figures 1.4 and 2.4). The influence of magnetic field in a electrically conducting fluid has established a force which is known as Lorentz force and that force perform against the main flow. So these kind of resisting forces slow down the primary velocity of fluid as detected from figures 1.5 and 2.5 that the effect of increasing values of the parameter M results in decreasing u and increasing v . It is deduced that when heat absorption parameter H is increased then the velocity u is increased, while velocity v get decreased (figures 1.6 and 2.6). Further, it is observed that velocities decrease when Prandtl number and Schmidt number are increased (figures 1.7, 2.7, 1.8 and 2.8). In actual sense,

the increase of Sc means decrease of molecular diffusivity (D). This means the process of diffusion will decrease.

Skin friction is given in table1. The value of τ_x increases with the increase in Hall current parameter, Prandtl number, thermal Grashof number, mass Grashof Number, heat absorption parameter and time, and it decreases with the angle of inclination of plate, the magnetic field and Schmidt number. Similar effect is observed with τ_y , except the angle of inclination of plate, magnetic field, and time, in which case τ_y increases with the angle of inclination of plate, magnetic field parameter, and decreases with time. Nusselt number is given in table2. The value of Nu decreases with increase in Prandtl number, heat absorption parameter and time.

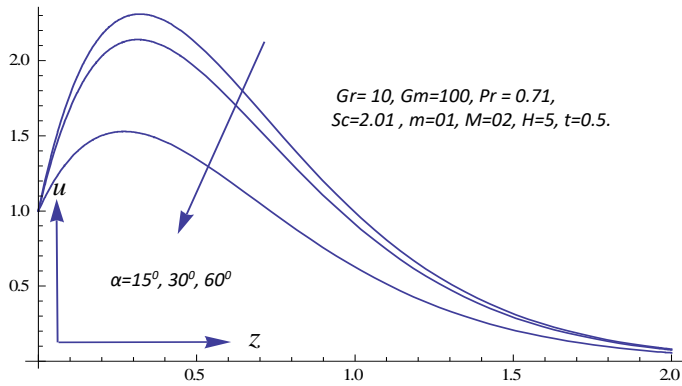


Figure 1.1. Velocity u for different values of α

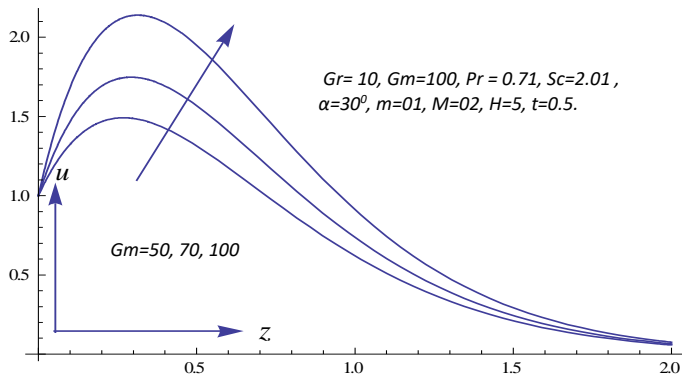


Figure 1.2. Velocity u for different values of Gm .

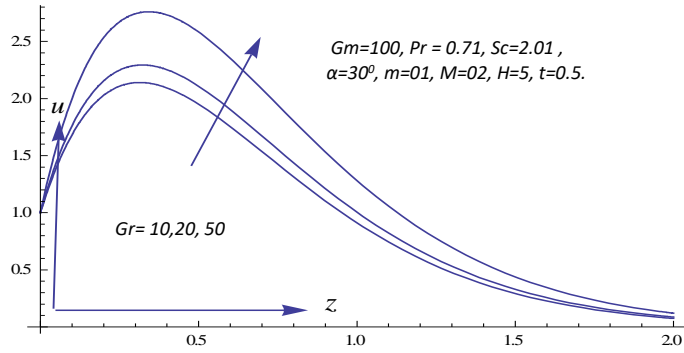


Figure 1.3. Velocity u for different values of Gr .

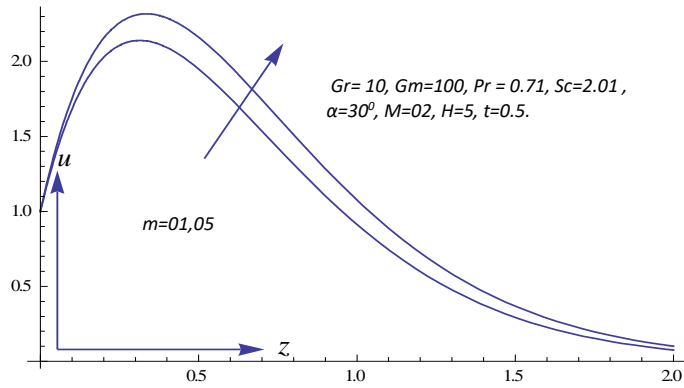


Figure 1.4. Velocity u for different values of m .

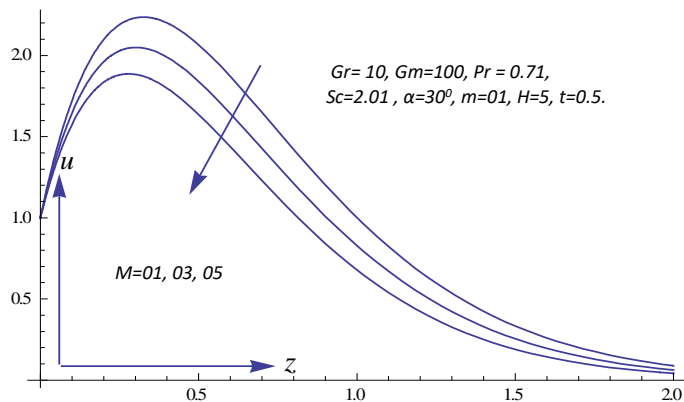


Figure 1.5. Velocity u for different values of M .

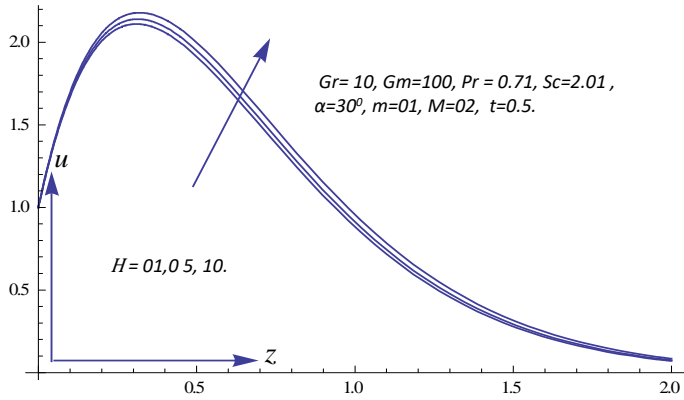


Figure 1.6. Velocity u for different values of H .

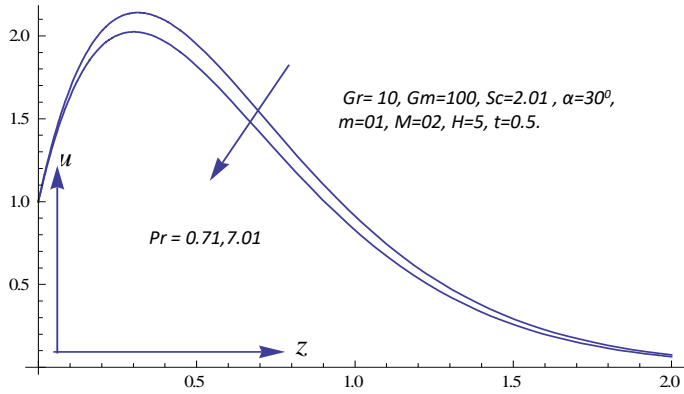


Figure 1.7. Velocity u for different values of Pr .

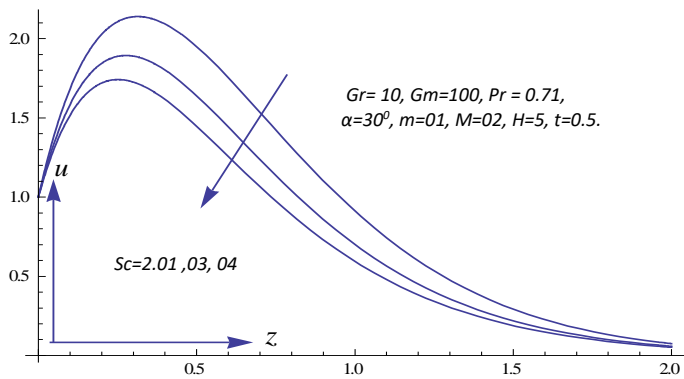


Figure 1.8. Velocity u for different values of Sc .

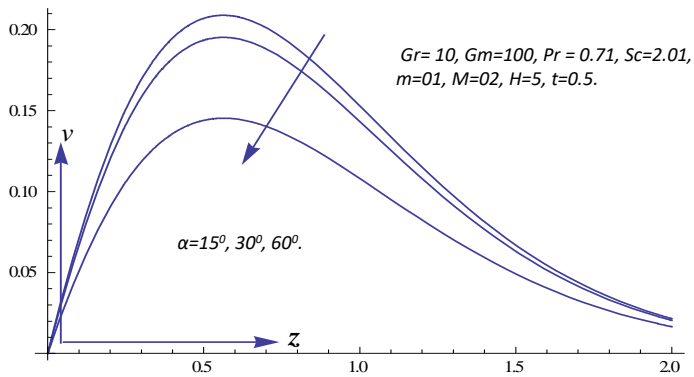


Figure 2.1. Velocity v for different values of α

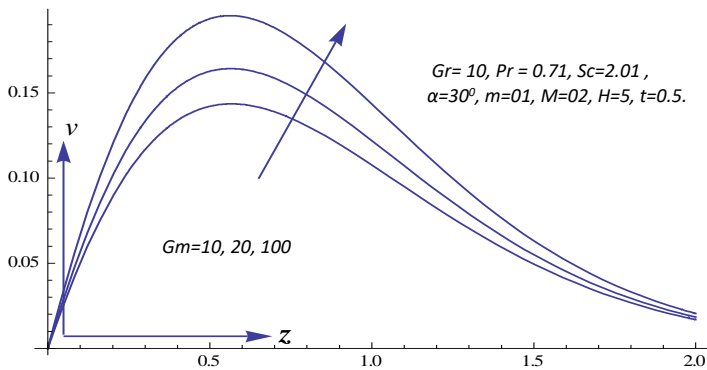


Figure 2.2. Velocity v for different values of Gm .

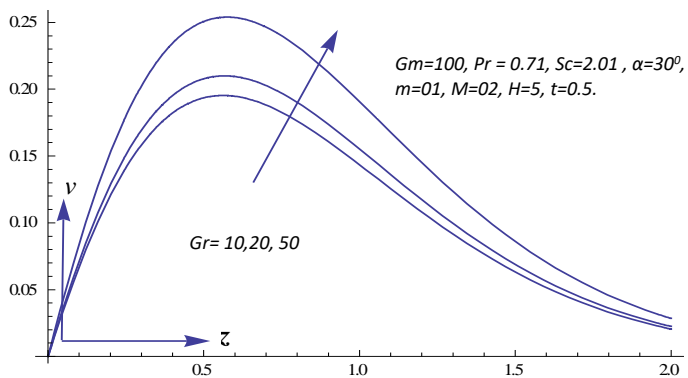


Figure 2.3. Velocity v for different values of Gr .

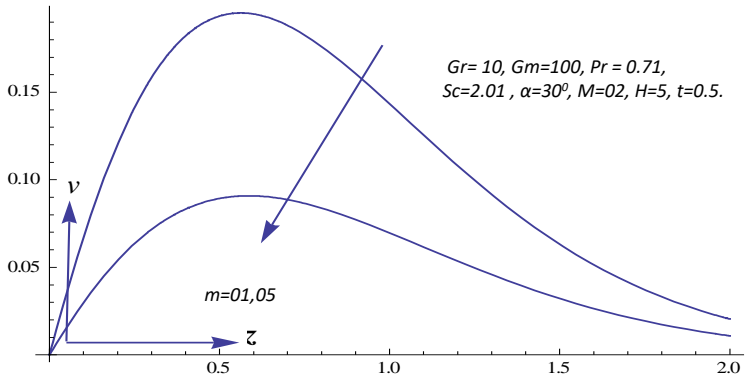


Figure 2.4. Velocity v for different values of m .

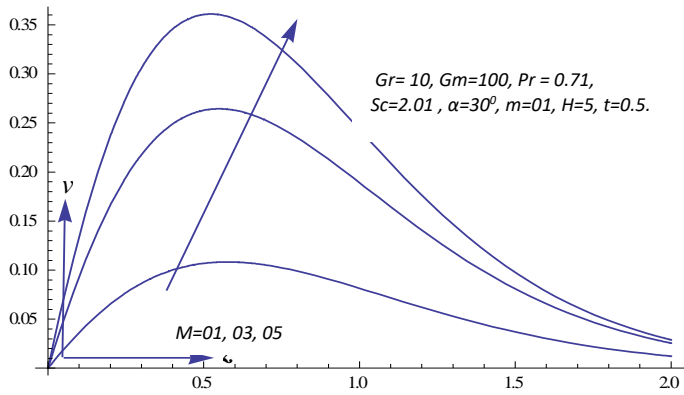


Figure 2.5. Velocity v for different values of M .

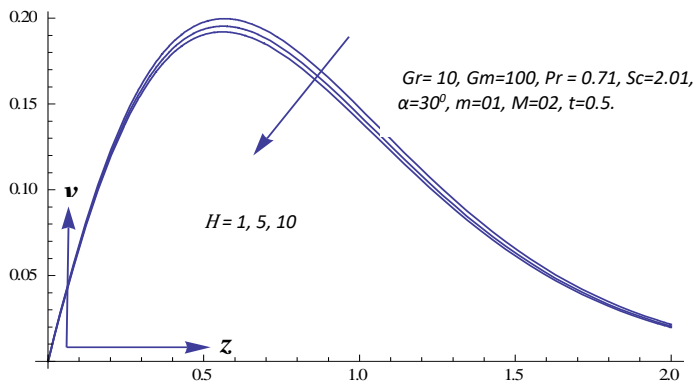


Figure 2.6. Velocity v for different values of H .

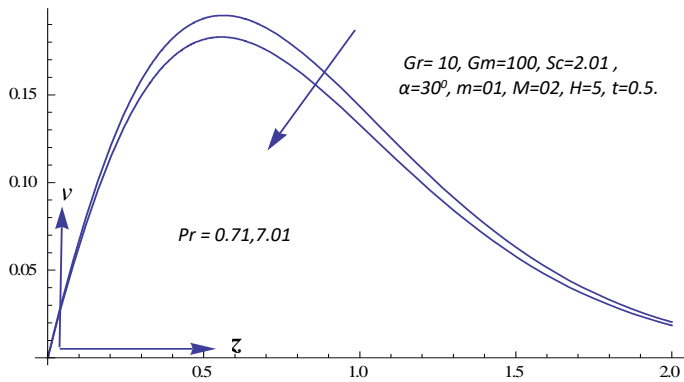


Figure 2.7. Velocity v for different values of Pr .

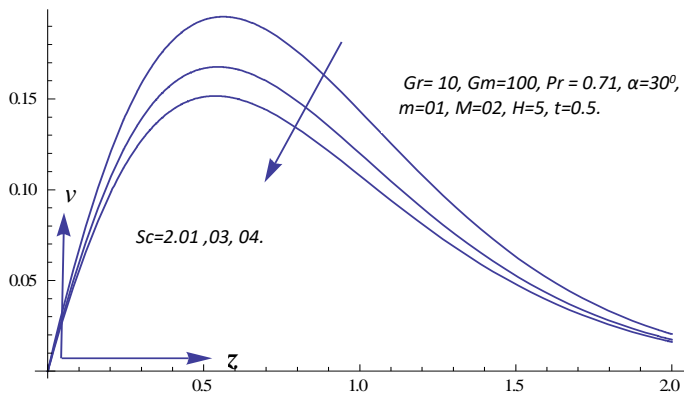


Figure 2.8. Velocity v for different values of Sc

Table 1. Skin friction for different parameter (α in degrees)

α	M	m	Pr	Sc	Gm	Gr	H	t	τ_x	τ_y
15	2	1.0	0.71	2.01	100	10	05	0.2	1.1195290	-0.223340
30	2	1.0	0.71	2.01	100	10	05	0.2	0.8472360	-0.175820
60	2	1.0	0.71	2.01	100	10	05	0.2	-0.150420	0.0016993
30	5	1.0	0.71	2.01	100	10	05	0.2	-0.717858	1.0649428
30	2	5.0	0.71	2.01	100	10	05	0.2	1.2885115	0.0212287
30	2	1.0	7.01	2.01	100	10	05	0.2	1.0009976	0.2649130
30	2	1.0	0.71	3.00	100	10	05	0.2	0.0432260	-0.612874

30	2	1.0	0.71	4.00	100	10	05	0.2	0.3934309	-0.188970
30	2	1.0	0.71	2.01	050	10	05	0.2	-0.337800	-0.194743
30	2	1.0	0.71	2.01	100	50	05	0.2	0.8088639	-1.975099
30	2	1.0	0.71	2.01	100	10	10	0.2	1.1059549	0.1179261
30	2	1.0	0.71	2.01	100	10	05	0.4	5.4633980	-0.568607

Table 2. Nusselt number for different parameter

H	Pr	t	Nu
05	0.71	0.4	-2.9533214
10	0.71	0.4	-3.7673379
05	4.00	0.4	-2.2309082
05	7.01	0.4	-2.9512142
05	0.71	0.3	-2.3535000
05	0.71	0.5	-3.5488468

4. Conclusion

In this paper a theoretical analysis has been done to study the effect of heat absorption on unsteady MHD flow past an impulsively started inclined plate with variable wall temperature and mass diffusion in the presence of Hall current. The results obtained for velocity and skin friction are in agreement with the actual flow. It is observed that the primary velocity increases with increasing the values of Hall parameter and heat absorption parameter. The secondary velocity decrease with increasing the values of Hall parameter heat absorption parameter. It is also found that the skin friction decreases with increasing the values of Hall parameter and heat absorption parameter. The Nusselt number decreases with heat absorption parameter.

Appendix:

$$a = \frac{M(1-im)}{1+m^2}, \quad A_1 = \operatorname{erfc} \left[\frac{-2Hit - z\sqrt{Pr}}{2\sqrt{t}} \right], \quad A_2 = \operatorname{erfc} \left[\frac{-2Hit + z\sqrt{Pr}}{2\sqrt{t}} \right],$$

$$A_3 = (-1 - A_{17} + e^{2\sqrt{az}}(A_{18} - 1)), \quad A_4 = (1 + A_{17} + e^{2\sqrt{az}}(A_{18} - 1)),$$

$$\begin{aligned}
A_5 &= (-1 + A_{19} + \exp(2z\sqrt{\frac{(a-H)P_r}{Pr-1}})(A_{20} - 1)), \\
A_6 &= (1 + A_{21} + \exp(2\sqrt{az})(1 - A_{22})), A_7 = (-1 + A_{23} + \exp(2z\sqrt{\frac{aS_c}{S_c-1}})(A_{24} - 1)), \\
A_8 &= (1 + A_{21} + \exp(2\sqrt{az})(A_{22} - 1)), A_9 = (-1 - A_{21} + \exp(2\sqrt{az})(A_{22} - 1)), \\
A_{10} &= (1 + A_{25} + \exp(-2Hi\sqrt{P_r})(A_{26} - 1)), A_{11} = (1 - A_{25} + \exp(-2Hi\sqrt{P_r})(A_{26} - 1)), \\
A_{12} &= (-1 - A_{27} + \exp(2z\sqrt{\frac{(a-H)P_r}{Pr-1}})(A_{28} - 1)), \\
A_{13} &= (-1 - A_{29} + \exp(2z\sqrt{\frac{aS_c}{S_c-1}})(A_{30} - 1)), \\
A_{14} &= \exp(\frac{at}{Pr-1} - z\sqrt{\frac{(a-H)P_r}{Pr-1} - \frac{HtP_r}{Pr-1}}), A_{15} = \exp(\frac{at}{S_c-1} - z\sqrt{\frac{aS_c}{S_c-1}}), \\
A_{16} &= (-1 + \operatorname{erf}(\frac{z\sqrt{S_c}}{2\sqrt{t}})), A_{17} = \operatorname{erf}(\sqrt{at} - \frac{z}{2\sqrt{t}}), A_{18} = \operatorname{erf}(\sqrt{at} + \frac{z}{2\sqrt{t}}), \\
A_{19} &= \operatorname{erf}(\frac{z}{2\sqrt{t}} - \sqrt{\frac{(a-H)tP_r}{Pr-1}}), A_{20} = \operatorname{erf}(\frac{z}{2\sqrt{t}} + \sqrt{\frac{(a-H)tP_r}{Pr-1}}), \\
A_{21} &= \operatorname{erf}(\frac{\sqrt{at} - z}{2\sqrt{t}}), A_{22} = \operatorname{erf}(\frac{\sqrt{at} + z}{2\sqrt{t}}), A_{23} = \operatorname{erf}(\frac{z - 2t\sqrt{\frac{aS_c}{S_c-1}}}{2\sqrt{t}}), \\
A_{24} &= \operatorname{erf}(\frac{z + 2t\sqrt{\frac{aS_c}{S_c-1}}}{2\sqrt{t}}), A_{25} = \operatorname{erf}(-Hi\sqrt{t} - \frac{z\sqrt{P_r}}{2\sqrt{t}}), \\
A_{26} &= \operatorname{erf}(-Hi\sqrt{t} + \frac{z\sqrt{P_r}}{2\sqrt{t}}), A_{27} = \operatorname{erf}(\sqrt{t}\sqrt{\frac{a-H}{Pr-1}} - \frac{z\sqrt{P_r}}{2\sqrt{t}}),
\end{aligned}$$

$$A_{28} = \operatorname{erf}\left(\sqrt{\frac{(a-H)t}{P_r-1}} + \frac{z\sqrt{P_r}}{2\sqrt{t}}\right), \quad A_{29} = \operatorname{erf}\left(\frac{1}{2\sqrt{t}}\left(\sqrt{\frac{at}{S_c-1}} - z\sqrt{S_c}\right)\right),$$

$$A_{30} = \operatorname{erf}\left(\frac{1}{2\sqrt{t}}\left(\sqrt{\frac{at}{S_c-1}} + z\sqrt{S_c}\right)\right),$$

References

- [1] Alia M.M., Mamunb A.A., Malequec M.A, Azimd N.H.A, *Radiation effects on MHD free convection flow along vertical flat plate in presence of Joule heating and heat generation*, *Procedia Engineering* (Elsevier), 56, 2013, pp. 503–509.
- [2] Das M., Mahatha B.K., Nandkeolyar R., Mandal B.K., Saurabh K., Unsteady hydromagnetic flow of a heat absorbing dusty fluid past a permeable vertical plate with ramped temperature, *Journal of Applied Fluid Mechanics*, 7(3), 2014, pp. 485-492.
- [3] Kumar G, Bansal A, Unsteady flow past on vertical cylinder in the presence of an inclined magnetic field and chemical reaction, *Analele Universitatii „Eftimie Murgu“ Resita, Fascicula de Inginerie*, 26(1), 2019, pp 107-118.
- [4] Kumar G., Kumar A., Misra M.K., Srivastava V., Chemical reaction effect on MHD flow past an impulsively started vertical cylinder with variable temperature and mass diffusion, *Journal of Science and Arts*, 47(2), 2019, pp. 513-522
- [5] Mamun A.A., Chowdhury Z.R., Azim M.A., Molla M.M., *MHD-conjugate heat transfer analysis for a vertical flat plate in presence of viscous dissipation and heat generation*, *International Communications in Heat and Mass Transfer*, 35, 2008, pp. 1275–1280.
- [6] Rajput U.S., Kumar G., Chemical reaction effect on unsteady MHD flow past an impulsively started oscillating inclined plate with variable temperature and mass diffusion in the presence of Hall current, *Applied research journal*, 2(5), 2016, pp.244-253.
- [7] Rajput U S, Kumar G, *Effects of radiation and chemical reaction on MHD flow past a vertical plate with variable temperature and mass diffusion*, *Journal of Naval Architecture and Marine Engineering*, 16, 2019, pp. 99-108.
- [8] Shit G.C., Halder R., Combined effects of thermal radiation and Hall current on MHD free-convective flow and mass transfer over a stretching sheet with variable viscosity, *Journal of Applied Fluid Mechanics*, 5(2), 2012, pp. 113-121.
- [9] Stanford Shateyi , Gerald T Marewo, On a new numerical analysis of the Hall effect on MHD flow and heat transfer over an unsteady stretching permeable

- surface in the presence of thermal radiation and heat source/sink, *Shateyi and Marewo Boundary Value Problems*, 170, 2014, pp. 014-170.
- [10] Seth G.S., Sarkar S., Mahato G.K., *Numerical solution of unsteady hydro-magnetic natural convection flow of heat absorbing fluid past an impulsively moving vertical plate with ramped temperature*, *International Journal of Applied Mathematical Research*, 2(2), 2013, pp. 317-324.
- [11] Sharma B.K., Jha A.K., Chaudhary R.C., Hall effect on MHD mixed convective flow of a viscous incompressible fluid past a vertical porous plate immersed in porous medium with heat source/sink, *Rom. Journ. Phys.*, 52(5), 2007, pp. 487–503.
- [12] Tanvir A., Md. Mahmud A., Finite difference solution of MHD mixed convection flow with heat generation and chemical reaction, *Procedia Engineering (Elsevier)*, 56, 2013, pp. 149 –156.

Addresses:

- Dr. Gaurav Kumar Department of Mathematics & Computer Science, Babu Banarasi Das University, Lucknow, India, logontogauravsharma@gmail.com (*corresponding author)
- Dr. S.M.K. Rizvi, Department of Mathematics & Computer Science, Babu Banarasi Das University, Lucknow, India. kamil@bbdu.ac.in
- Dr. Amresh Kumar, Department of Mathematics, Babu Banarasi Das Northern India Institute of Technology, Lucknow, India. amresh_srivastava@yahoo.co.in

A Python application to generate digital signals

Tatian-Cristian Mălin, Dorian Nedelcu*, Gilbert-Rainer Gillich

We introduce in this paper an application developed in the Python programming language that can be used to generate digital signals with known frequencies and amplitudes. These digital signals, since have known parameters, can be used to create benchmarks for test and numerical simulation.

Keywords: *Python application, signal generation, sinusoid, noise, damping, phase shift*

1. Introduction

The typical sensor for measuring the dynamic response of structures is the accelerometer. It generates a digital signal that is represented by a sequence of discrete values [1]-[3]. When interpreting earthquake response signals measured with accelerometers, estimation of velocities and displacements is often required [4].

To study the behavior of structures during earthquakes, we need digital signals that are presenting different earthquake movements. A list of databases that can be accessed on the Web that contain earthquake accelerograms in digital form are presented in [5], the most relevant being [6]-[8]. Due to modern techniques and methods of processing and converting analog data into digital data, the original recordings from bulletins and seismograms can be digitized and re-analyzed [9]. However, since most diagrams represent acceleration signals, we need to find the antiderivatives, namely the velocity and displacement. In prior research we developed an algorithm and implemented it in an application written in Python language, which calculates the antiderivatives. To test the accuracy of this application we need using digital signals with known parameters (frequency, amplitude, phase, damping coefficient, existence of noise). In this paper, we introduce the application that generates digital signals with known parameters and exemplify outcomes for different settings of the parameters.

2. The generated signal

The aim of this section is to introduce the theoretical aspects regarding the signals we can generate with an application we developed in Python. In the proposed application we can generate signals with up to three harmonic components S_i ($i=1\dots3$), which have the amplitudes a , b and c , the frequencies f_i and the phase Ph_i . Thus, the harmonic components of the signal can be written as follows:

- the first sinusoidal component is:

$$S_1 = a \cdot \sin(2 \cdot \pi \cdot f_1 \cdot t + \pi \cdot Ph_1) \quad (1)$$

- the second sinusoidal component is:

$$S_2 = b \cdot \sin(2 \cdot \pi \cdot f_2 \cdot t + \pi \cdot Ph_2) \quad (2)$$

- the third sinusoidal component is:

$$S_3 = c \cdot \sin(2 \cdot \pi \cdot f_3 \cdot t + \pi \cdot Ph_3) \quad (3)$$

In relations (1) to (4), t represents the time, i.e. the length of the signal.

We can also add both noise W and damping D to the signal. The damping is generated by involving the term:

$$D = e^{Damp \cdot t} \quad (4)$$

where $Damp$ is the damping coefficient. Note that, the damping coefficient can get associated positive values in the case of increasing the amplitude of the signal, or negative values in the case we intend to decrease the amplitudes.

The effect of noise can be expressed as:

$$W = p(x) \cdot Noise / \max[p(x)] \quad (5)$$

where $p(x)$ is the probability density for the Gaussian distribution and $Noise$ is a randomly generated value for each discrete time moment.

Finally, the most complex form of the signal is:

$$S = D \cdot (S_1 + S_2 + S_3 + W) \quad (6)$$

The signal is used to test application that derivate or integrate signals, for which the signal parameters should be known.

3. The *SignalGeneration* application

The *SignalGeneration* application was developed based on the Python programming language and is defined by four classes: "SignalGeneration", "Table_Grid", "Plot" and "PlotNotebook" and four public functions: "ExtragTextMemory", "ExtragImageMemory", "IsNumeric" and "Put_Clipboard". The main window represents a notebook control, which manage one chart window with the named tab: "Signal Generated". The "Plot" and "PlotNotebook" classes create the main window where the notebook with the chart windows will be created.

The public function "ExtragTextMemory" extract the Excel template from database to be saved as Excel file into "RESULTS" folder created by application. The template contains chart that will be updated at the end of the transfer. The public function "ExtragImageMemory", extracts the icons from database to memory to be used as icons when creating the toolbar.

The public function "Put_Clipboard" copies a string into Windows Clipboard and is called by "OnExcel" function from "SignalGeneration" class. When the results are exported to Excel file, these are memorized in strings copied to Windows Clipboard and pasted into Excel. The reason of this operation is a significative short time required for transfer comparing with export values cell by cell.

The "Table_Grid" show the numerical results on screen into a grid control.

The application uses a SQLite database to memorize the toolbar icons as image format and the "Excel template.xls" file, where the numerical and charts results will be exported. These files were loaded as Binaly Large Objects (BLOB) in "Config.db" application's file. Features of the toolbar are shown in figures 1 and 2.

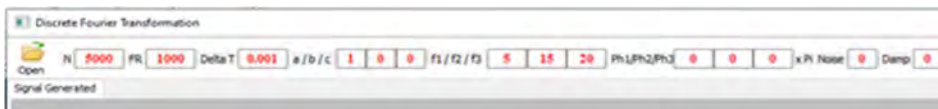









Figure 1. The toolbar of the *SignalGeneration* application – input data





Figure 2. The toolbar of the *SignalGeneration* application – processing buttons

The application's toolbar is located at the top-left of the main window and includes text and button controls marked, with the functions described in table 1.

Table 1. Functions of the *SignalGeneration* toolbar

	Open – Load signal form CSV saved previous file.
N <input type="text" value="5000"/>	Text control to input 'Number of samples' N variable.
FR <input type="text" value="1000"/>	Text control to input 'Sampling frequency' FR variable.
Delta T <input type="text" value="0.001"/>	Text control to show 'Time interval' Delta T variable (Read Only – computed by application).
a / b / c <input type="text" value="1"/> <input type="text" value="0"/> <input type="text" value="0"/>	Text controls to input 'First/Second/ Third Amplitude' values of the A1/ A2/A3 variables.
f1 / f2 / f3 <input type="text" value="5"/> <input type="text" value="15"/> <input type="text" value="20"/>	Text controls to input 'First/Second/Third Target Frequency' values of the f1/f2/f3 variables.
Ph1/Ph2/Ph3 <input type="text" value="0"/> <input type="text" value="0"/> <input type="text" value="0"/>	Text controls to input 'First/Second/ Third Phase' coefficients of the Ph1/ Ph2/Ph3 variables.
x Pi Noise <input type="text" value="0"/>	Text control to input 'White Noise' Noise variable.
Damp <input type="text" value="0"/>	Text control to input 'Damping coefficient' Damp variable.
	Generate – Calculate the signal based on equation (6) and create the chart of the signal.
	Data table – Shows the table of the signal values, calling "Table_Grid " class.
	Word – Save application's graphical results to Word file.
	Excel – Save application's results (graphical and numerical) to Excel file.
	Fit Chart – Returns to initial view in the chart windows.
	Zoom - Enlarges selected area in chart windows.

	Pan - zoom in/out with the right mouse button pressed.
	Exit – Quit the application, calling "OnClose" function from "SignalGeneration" class.

The *SignalGeneration* application use the dependencies presented in table 2.

Table 2. Dependencies used by the *SignalGeneration* program

Python(x,y)	A free scientific and engineering development software for numerical computations, data analysis and data visualization based on Python programming language.	https://python-xy.github.io/
Matplotlib	A Python 2D plotting library which produces publication quality charts.	https://matplotlib.org/
wxPython	The cross-platform Graphical User Interface toolkit for the Python language.	https://wxpython.org/
SQLite	A C-language library that implements a small, fast, self-contained, high-reliability, full-featured, SQL database engine.	https://www.sqlite.org/index.html
numpy	The fundamental package for scientific computing with Python.	https://numpy.org/

4. Examples of generated signals

The signals, which represent measured accelerations in mm/s^2 are generated with a number of samples $N=6000$ by a sampling frequency $FR=1000$ Hz. In table 3 are presented different settings of the parameters used to generate signals with the *SignalGeneration* application.

Table 3. Parameter settings for the generated signals

Figure	a	b	c	f_1	f_2	f_3	Ph_1	Ph_2	Ph_3	Damp	Noise
3	1	0	0	1	0	0	0	0	0	0	0
4	1	0	0	1	0	0	1	0	0	0	0.5
5	1	0	0	1	0	0	1	0	0	0.5	0

6	1	1	0	1	15	0	0	0	0	-0.5	0.5
7	1	1	1	1	5	10	0	0	0	0	0
8	1	1	1	1	5	10	0	0	0	-0.5	0
9	1	1	1	1	5	10	1	1	1	-0.5	0.5

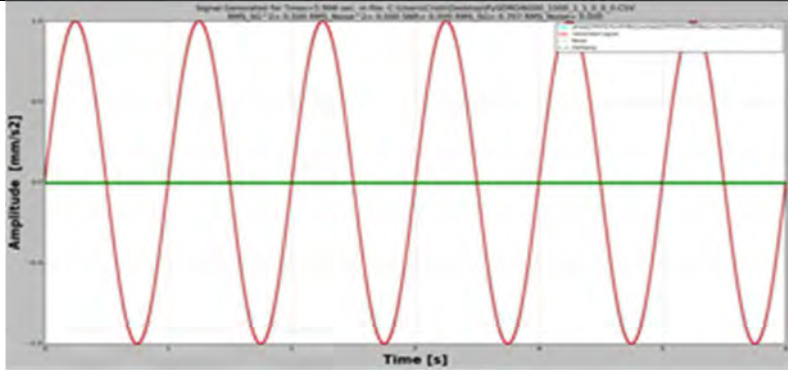


Figure 3. The signal with one harmonic component

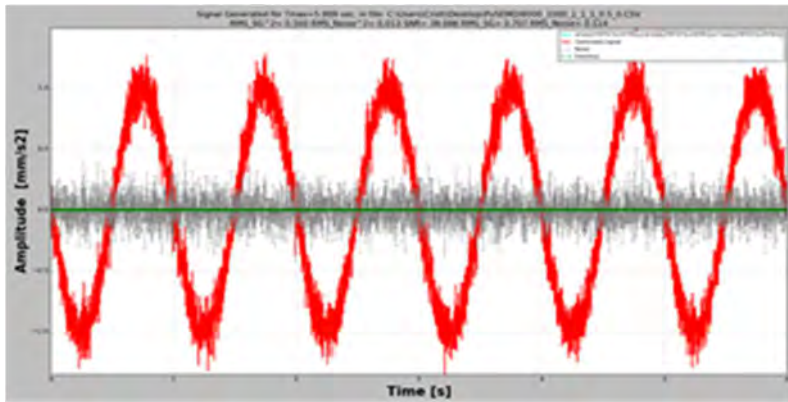


Figure 4. The signal with one harmonic component polluted with noise

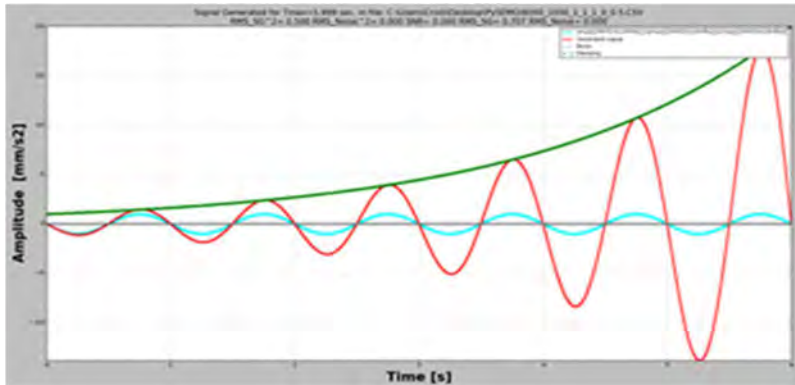


Figure 5. The signal with progressively increasing amplitude

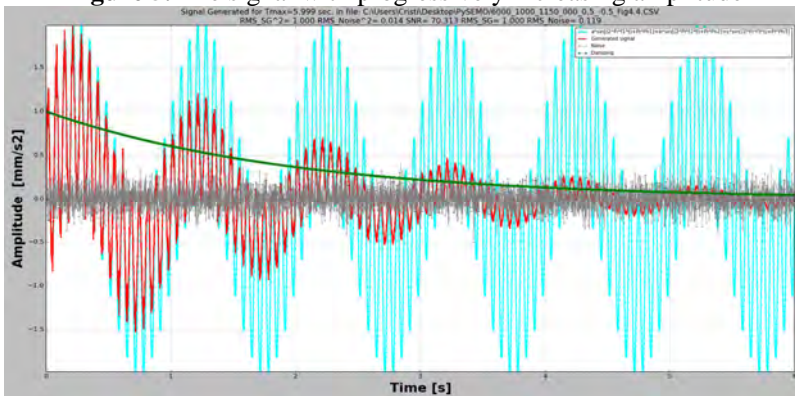


Figure 6. Damped signal with two components

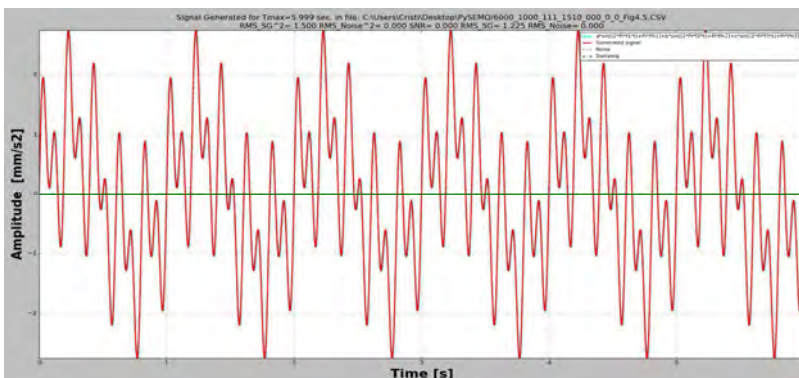


Figure 7. Signal with three components

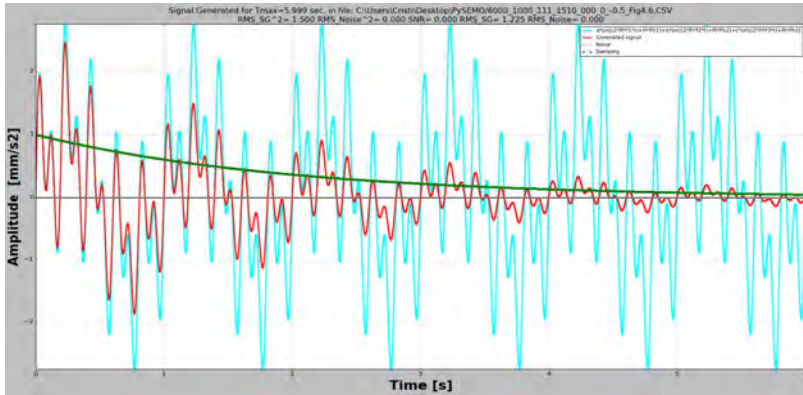


Figure 8. Damped signal with three components

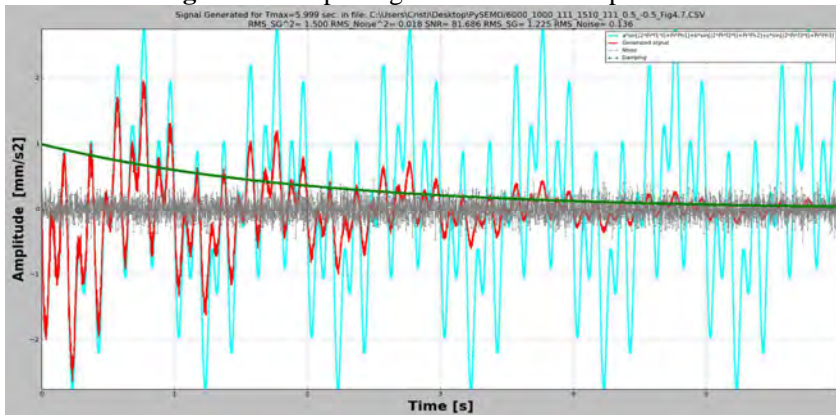


Figure 9. Damped signal with three components polluted with noise

In figures 3 to 9, we present the generated signals with the parameter settings from table 3. The different signals are represented in these figures with different colors (*green* – damping, *gray* – noise, *cyan* – signal with one to three components in the absence of damping and noise) and with *red* is represented the resulted signal.

5. Conclusion

In this paper, we present an application developed in the Python programming language that generates digital signals with known parameters (frequency, amplitude, phase, damping coefficient, existence of noise) and exemplify outcomes for different settings of the parameters. These digital signals, since have known parameters, can be used to create benchmarks for test and numerical simulation.

For our future research we need digital signals, with known parameters, to calculate the velocity and displacement from accelerograms and to use them as input for dynamic simulations, made for base-isolated structures.

References

- [1] Dueck R.K., *Digital Design with CPLD Applications and VHDL*, Cengage Learning, 2nd edition, 2011.
- [2] Proakis J.G., Manolakis D.G., *Digital Signal Processing*, Pearson Prentice Hall, 2007.
- [3] Grahame S., *Analogue and Digital Communication Techniques*, Newnes, 1999.
- [4] Nedelcu D., Malin T.C., Gillich G.R., Barbinta C.I., Iancu V., *Displacement and velocity estimation of the earthquake response signals measured with accelerometers*, The 9th International Conference on Advanced Concepts in Mechanical Engineering - ACME 2020, Jun. 4-5, 2020, Iasi, Romania.
- [5] Malin T.C., Gillich G.R., Nedelcu D., Iancu V., *Earthquake registrations database*, *Analele Universitatii „Eftimie Murgu“ Resita, Fascicula de Inginerie* 26(1), 2019.
- [6] <https://www.ngdc.noaa.gov/hazard/earthqk.shtml> last accessed 09.08.2020.
- [7] <https://earthquake.usgs.gov/earthquakes/search/> last accessed 09.08.2020.
- [8] <https://www.strongmotion.org> last accessed 09.08.2020.
- [9] Malin T.C., Gillich G.R., Nedelcu D., Iancu V., *Digitization of earthquake signals stored as images*, 43rd International Conference on Mechanics of Solids, 2019.

Addresses:

- PhD Student Tatian-Cristian Mălin, Babeş-Bolyai University, Faculty of Engineering, Piața Traian Vuia, nr. 1-4, 320085, Reșița, cristian.malin@student.uem.ro
- Prof. Dr. Eng. Dorian Nedelcu, Babeş-Bolyai University, Faculty of Engineering, Piața Traian Vuia, nr. 1-4, 320085, Reșița, d.nedelcu@uem.ro
(* corresponding author)
- Prof. Dr. Eng. Gilbert-Rainer Gillich, Babeş-Bolyai University, Faculty of Engineering, Piața Traian Vuia, nr. 1-4, 320085, Reșița, gr.gillich@uem.ro

Static and dynamic tests at a railway tank wagon

Tiberiu Stefan Mănescu, Nicusor Laurentiu Zaharia*, Constantin Ioan Barbița

Railway tank wagons are widely used for the transportation of liquid cargo as petroleum products, acids, alcohol etc. During the last years only tank wagons with bogies were manufactured (four axles wagons). The prototype of each wagon's series is tested according with international standards in purpose to validate the design (the project). This paper present the static and dynamic test performed at the body of a four axles tank wagon.

Keywords: tests, tank wagon, body, stress, strain

1. Stress calculation based on strains measurement.

Stress occur in the structures due the efforts. With the help of strain gauges glued on a structure we ca measure strains when an effort (force or moment) is applied. The strain measured with a strain gauge can be transform in stress with Hooke's law [1]:

$$\sigma = E \cdot \varepsilon \quad (1)$$

where σ is the stress, E is Young modulus and ε is the measured strain with the strain gauge. The strains measured with a rosette (0° - 45° - 90°) can be transform in stress with above equations [1]:

$$\sigma_1 = \frac{E}{2(1-\nu)} (\varepsilon_A + \varepsilon_C) + \frac{E\sqrt{2}}{2(1+\nu)} \sqrt{(\varepsilon_A - \varepsilon_B)^2 + (\varepsilon_C - \varepsilon_B)^2} \quad [N/mm^2] \quad (2)$$

$$\sigma_2 = \frac{E}{2(1-\nu)} (\varepsilon_A + \varepsilon_C) - \frac{E\sqrt{2}}{2(1+\nu)} \sqrt{(\varepsilon_A - \varepsilon_B)^2 + (\varepsilon_C - \varepsilon_B)^2} \quad [N/mm^2] \quad (3)$$

$$\sigma_{ech} = \sqrt{\sigma_1^2 + \sigma_2^2 - \sigma_1\sigma_2} \quad [N/mm^2] \quad (4)$$

where σ_1 is the principal stress 1, σ_2 is the principal stress 2, σ_{ech} is von Mises equivalent stress, E is Young modulus and ε_A , ε_B , ε_C are the measured strains with the rosette and ν is Poisson ratio.

2. Sensors setup

Strain sensors (strain gauges and rosettes) are glued on the structure (body) of the wagon based on finite element analysis and/or experience of the of the test experts. The setup of the sensor is important for each test's objective according with the standard [2], [3].

2.1. Sensor setup for static tests.

For the static tests, strain gauges and rosettes were mounted for strains measurements and stress calculation. The forces were measured with force cells and the deformation of the body under loads were measured with displacement transducers.

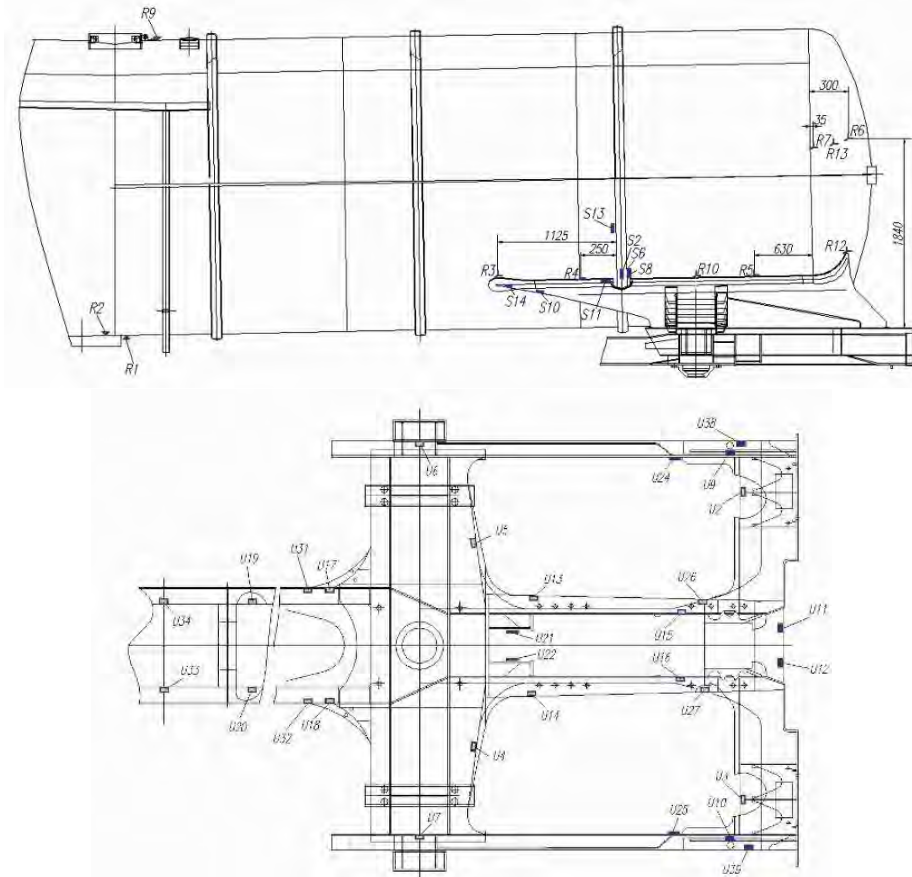


Figure 1. Strain gauge and rosettes layout.

2.2. Sensor setup for dynamic test.

For the dynamic tests (impact tests), strain gauges and rosettes were used for strains measurements and stress calculation. The impact forces under buffer's plate was measured with load cell, the acceleration in longitudinal direction was measured with an accelerometer. The impact speed was also measured.



Figure 2. Force cell and accelerometer.

3. Tests

Before the tests, numerical studies with finite element method were done. Those studies were the starting point of some of strain gages locations [4]. The finite element analysis software used was ANSYS [7]. At this moment, the finite element method is widely used all over the world by the designers, but is far to be perfect; because of its limits it is necessary that virtual experiments to be confirmed by real experiments. But still, finite element method is one of the most powerful tools used in design stage or when the necessity to modify the body of the prototype vehicle when some unconformities appear due the testing or because some last moments client requirements [8]. During the years, the observations proved that none of the testing methods (virtual or real) it is not a panacea (a combinations of the methods is recommended), at that moment the real tests are the key (or decision element) to prove the conformity or not of a product with reference documents (standards, technical specifications etc.).

Experimental stress analysis with strain gages for the tank wagon was performed in Romanian Railway Authority AFER's Rolling Stock Laboratory (RENAR accredited laboratory) as follows:

- Static tests on AFER's static test bench from Bucharest;
- Dynamic ramming at AFER's Railway Testing Center from Făurei.

Experimental stress analysis with strain gages for wagons is made according with [9], [10]. European Normative 12663 was fundamentally changed in 2010 (even if modification draft was from 2007) regarding to the first version from 2000. Since

2010, the standard has two parts, the first is for passenger coaches and locomotives and the second part is for the wagons. Regarding the second part, there are similarities between the EN 12663 and ERRI B12/RP 17 and ERRI B12/RP 60 especially to the classifications of elements joints (welded) commonly founded at railways applications used to make an evaluation of vehicle body fatigue during life time, based of static tests.

3.1. Static tests and results.

The static tests performed to the tank wagon were [10]:

- Horizontal forces:
 - Tensile test at couple level with 1500 kN (TA);
 - Compressive test at couple level with 2000 kN (CA);
 - Compressive test on buffer's axe with 2 x 1000 kN (CT);
 - Compressive test on buffers at 50 mm below buffer's axe level with 2 x 750 kN (CT50);
 - Diagonal compressive test with 400 kN (CDD right and CDS left);
- Vertical loads (according with technical specification of the wagon):
 - vertical load test (V1) normal load;
 - vertical load test (V2) exceptional load;
 - lifting of the wagon at one end (RID);
 - lifting of the wagon (RID4)
- Combined loads:
 - tensile test at couple level combined with vertical load V1 (TA+V1);
 - compressive test at couple level combined with vertical load V1 (CA+V1);
 - compression buffer's axe test combined with vertical load V1 (CT+V1).

Horizontal forces were applied with hydraulic installation of the test bench at one end of the wagon and creating reactions at the other end of the wagon. Vertical loads were created loading the tank with water.

The measured stress with strain gauges in N/mm², must be smaller [10] than these indicated in the next table.

Table 1. Permissible stress for Chassis material: S355J2G3

Horizontal forces, lifting and combined loads limits (σ_{aH})		Welding free area 355	Welding area 323
Vertical loads (σ_{aV})	Class	A 277	
		B 150	
		C 133	
		D 110	

For rolling stock applications, strain gages with 10 mm measuring base are recommended but from our experience we can tell that also strain gages with 6 mm measuring base can be used. Because the body of the wagon is made from steel, Y series strain gages were used for general purpose. The electrical nominal resistance of Y series strain gages for railway applications is 120Ω because the strain gages it is a simple resistor [10]. As a measuring method experimental stress analysis with strain gages is very interesting because is an indirect measuring method: the strains from the wagon's body are transformed in an electrical resistance variation (because the strain gage is glued on the body) and from the variation of electrical units are transformed on a mechanical unit. In the next table are presented results for some strain gauges for horizontal and vertical loads.

Table 2. Results for some strain gauges (SG)

SG	σ_{aH}	σ_{aV}	CA	CT	CT50	TA	CDD	CDS	RID	RID4	V1
S1	309	110	10	17	15	-2	23	-18	0	9	-5
S2	355	277	-117	-172	-129	2	-85	22	128	-156	-55
S3	309	110	9	11	8	-9	3	-2	-12	-3	-6
S4	355	110	-12	2	2	10	0	1	6	5	-18
S5	309	110	-21	-4	-4	12	-2	1	4	2	-12
S6	309	110	-20	-38	-29	17	-20	7	26	-39	-15
S7	309	110	7	81	72	-7	87	-57	-176	77	11
S8	309	110	-5	-6	-6	9	2	-5	30	-12	-24
S9	355	277	-128	-186	-144	103	-68	-5	339	47	15
S10	355	277	-93	-126	-94	75	-51	8	132	-49	-13

3.2. Dynamic test and results.

Ramming tests simulate shock due sorting in marshaling yard. Shocks with empty wagon and loaded wagon were performed. The purpose of the shock test with empty wagon is that after the test, the functionality of the wagon not be affected, so no strains or stress in wagon's body are measured.

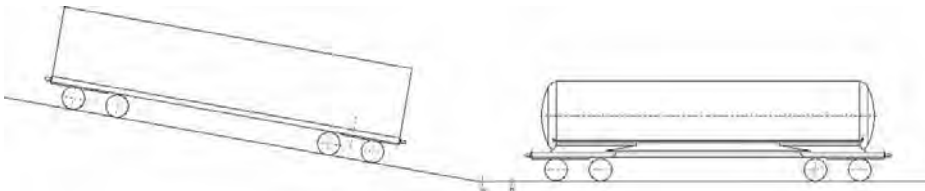


Figure 3. Ramming of the tank wagon.

The dynamic tests with empty or loaded wagon were performed as follows:

- The tank wagon was empty or loaded at maximum axle load;
- The tank wagon, placed in straight and level line was rammed by a ramming wagon fitted according with ERRI B12/RP17 report, chapter 3.1 (see figure 3);
- 40 shocks were done and maximum and residual strains were measured. With the help of Microsoft Excel, the trend of cumulated residual strains \mathcal{E}_{rc} was observed. The tests were performed at Fåurei Test Center.

Below in the figures is presented the evolution of different measured parameters, and the numerical results are presented in tables 3 and 4.

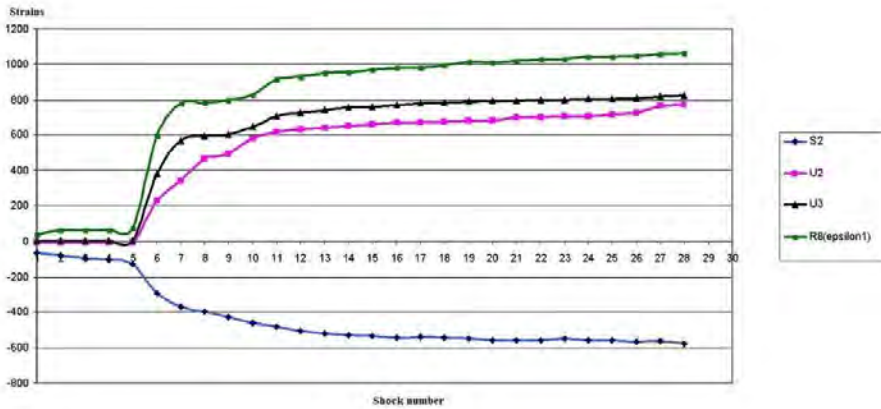


Figure 4. Strains evolution.

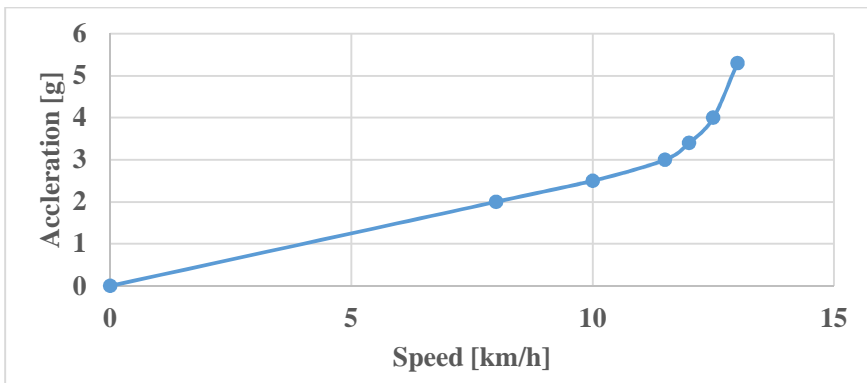


Figure 5. Acceleration versus speed.

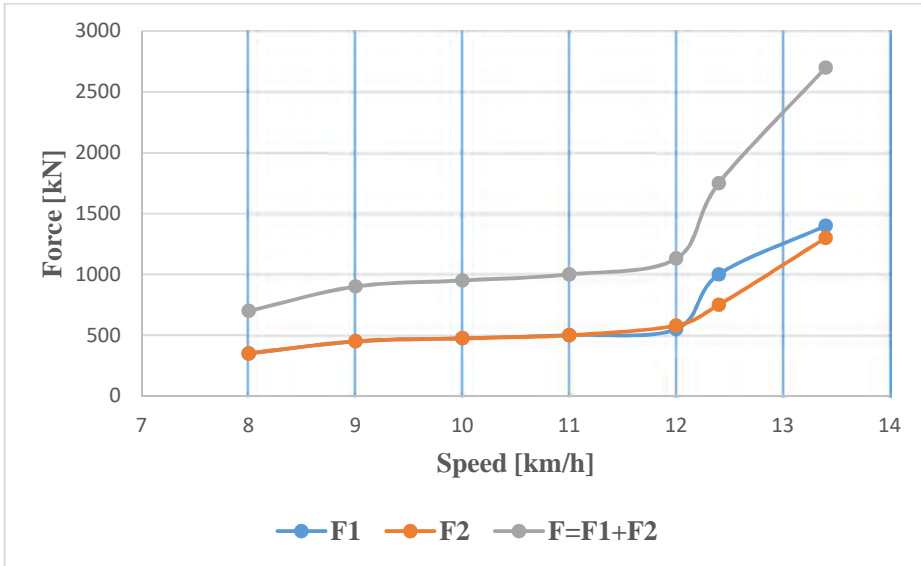


Figure 6. Force on buffers versus speed.

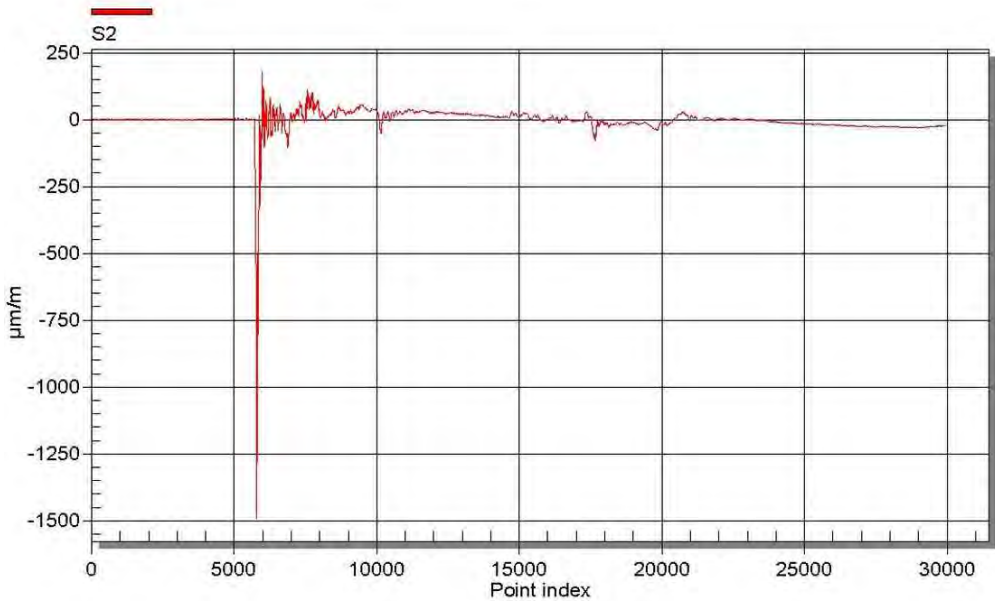


Figure 7. Strain evolution during a shock for S2 strain gauge.

Table 3. Results for some strain gauges (SG)

Shock number	5		10		15		20	
V km/h	12.16		12.00		12.08		11.92	
	σ_{\max} N/mm ²	ϵ_{rc} $\mu\text{m}/\text{m}$	σ_{\max} N/mm ²	ϵ_{rc} $\mu\text{m}/\text{m}$	σ_{\max} N/mm ²	ϵ_{rc} $\mu\text{m}/\text{m}$	σ_{\max} N/mm ²	ϵ_{rc} $\mu\text{m}/\text{m}$
S2	-232	-4	-194	-30	-200	-53	193	-49
S3	-9	5	-8	8	-8	10	-8	11
S9	-80	-10	-71	-29	-71	-24	-69	-25
S14	-89	17	-73	4	-74	-2	-69	-3
S15	-69	1	-49	-2	-50	-1	-44	2
S16	-172	-26	-151	-45	-155	-62	-153	-65
U2	171	-7	153	-5	148	-5	148	-6
U3	222	12	190	13	189	13	184	11
U26A	-88	-55	-84	-66	-81	-66	-82	-84
U27A	-179	66	-153	62	-156	65	-152	57

Table 4. Results for some strain gauges (SG)

Shock number	25		30		35		40	
V km/h	12.04		11.88		12.08		12.08	
	σ_{\max} N/mm ²	ϵ_{rc} $\mu\text{m}/\text{m}$	σ_{\max} N/mm ²	ϵ_{rc} $\mu\text{m}/\text{m}$	σ_{\max} N/mm ²	ϵ_{rc} $\mu\text{m}/\text{m}$	σ_{\max} N/mm ²	ϵ_{rc} $\mu\text{m}/\text{m}$
S2	-203	-59	-233	-52	-236	-62	-229	-91
S3	-8	12	-9	13	-9	17	-9	18
S9	-71	-27	-84	-27	-87	-34	-82	-53
S14	-71	-10	-83	-8	-86	-13	-82	-28
S15	-41	6	-51	16	-72	28	-67	18
S16	-160	-73	-180	-69	-185	-71	-180	-100
U2	151	-6	163	-8	167	-7	159	-7
U3	189	7	212	5	216	5	213	3
U26A	-85	-101	-92	-98	-92	-109	-89	-103
U27A	-157	51	-173	49	-177	38	-176	41

4. Conclusion

The tank wagons are widely used by railway freight operators to load and transport products like oil, gases, crude oil, mineral and vegetal oils, acids, alcohol, bitumen, water etc.

The results calculated with finite elements method are used useful in design stage or as previous stage of experimental stress analysis. The finite elements analysis was performed step by step: for example, if the thickness of the tank is smaller with 50% than initial, the tare of the wagon is 30% smaller than initial. The results confirm that such hard modification is possible, because the von Mises stress and displacements are smaller that allowable stress and deformations.

Experimental stress analysis with strain gages offer accurate measured results of an existing stress from a wagon's body when external forces are applied. Because is non-destructive measuring method, the test can be repeated. The accuracy of measuring devices is extremely high and it is validated by calibration with special calibrator devices or precision resistors. The experimental results, can be also used in purpose to validate finite element analysis results or as feedback for numerical model.

Based on test results, the designer can improve his design to increase the quality of the final product.

There is a correlation between the symmetrical measuring points, but differences appear during tests.

The explanations of the results can be:

- the wagon structure is not entirely symmetrically (dimensional tolerances are allowed for the chassis elements);
- the measuring points are not exactly at the same coordinates (minor differences appear during strain gages gluing);
- the forces are not applied symmetrically, because the longitudinal axe of the wagon is not coincident with railways axe (because of rail gauge).

References

- [1] Mănescu T.Ș., Jiga G.G., Zaharia N.L., Bîtea C.V., *Noțiuni fundamentale de rezistența materialelor si teoria elasticității*, Editura Eftimie Murgu, Reșița, 2010.
- [2] Tripa P., *Metode mecanice pentru determinarea deformațiilor și tensiunilor mecanice*, Editura Mirton, Timișoara, 2010.
- [3] Barbinta C.I., Tufisi C., Hamat C.O., Nedelcu D., Gillich G.R., Sensitivity analysis for frequency-based prediction of cracks in open cross-section beams, *Vibroengineering PROCEDIA*, 27, 2019, pp.7-12.

- [4] Mănescu T.S., Zaharia N.L., Avram D.S., Țigănașu N.M., *Nonlinear finite element analysis used in at tank wagons*, Proceedings of the 4th WSEAS International Conference on Finite Differences - Finite Elements - Finite Volumes - Boundary Elements, pp. 110-113, World Scientific and Engineering Academy and Society (WSEAS) Stevens Point, Wisconsin, USA, 2011.
- [5] Mănescu T.S., Zaharia N.L., Avram D.S., Țigănașu N.M., *Experimental stress analysis on a wagon model for railway vehicles*, Advances in Control, Chemical Engineering, Civil Engineering and Mechanical Engineering, European Conference of Mechanical Engineering, Puerto De La Cruz, Tenerife, Nov. 30- Dec. 2, 2010, pp. 19-21.
- [6] Capek J., Malkovsky Z., *Experience with the Testing of Railway Vehicles according to the European Standards*, Proceeding of The First International Conference on Railway Technology: Research, Development and Maintenance, Las Palmas de Gran Canaria, Spain 2012, Wroclaw, Poland, pp. 133-134.
- [7] Zaharia N.L. *Determinarea stării de tensiune și deformații în structurile portante de cale ferată prin metoda elementelor finite cu ajutorul Ansys*, Simpozionul Național de Material Rulant de Cale Ferată, Nov. 26-27, 2012, Universitatea Politehnica București, Editura MatrixRom, București.
- [8] Vatulia G., Falendysh A., Orel Y., Pavliuchenkov M., *Structural Improvements in a Tank Wagon with Modern Software Packages*, 10th International Scientific Conference Transbaltica 2017: Transportation Science and Technology, Elsevier Procedia Engineering, 2017.
- [9] EN 12663-1:2010+A1:2014 Railway applications. Structural requirements of railway vehicle bodies. Locomotives and passenger rolling stock (and alternative method for freight wagons).
- [10] EN 12663-2:2010 Railway applications. Structural requirements of railway vehicle bodies. Freight wagons.

Addresses:

- Prof. Dr. Eng. Tiberiu Ștefan Mănescu, Babeș-Bolyai University, Faculty of Engineering, Piața Traian Vuia 1-4, 320085 Reșița, mts.tibi@yahoo.com
- Dr. Eng. Nicușor Laurențiu Zaharia, Romanian Railway Authority București, Calea Griviței 393, 010719 București, laurentiu@afer.ro (* *corresponding author*)
- Dr. Eng. Constantin Ioan Bărbintă, Babeș-Bolyai University, Faculty of Engineering, Piața Traian Vuia 1-4, 320085 Reșița constantin.barbinta@yahoo.ro

Improvement of Jain's algorithm for frequency estimation

*Andrea Amalia Minda, David Lupu, Gilbert-Rainer Gillich**

In this paper we propose a procedure to correct Jain's algorithm, which in certain situations fails in correctly estimating the frequency by indicating frequency values that are very far from the real frequency. It happens because the two points considered for the method proposed by Jain are not on the same lobe. Thus, a method is proposed according to which these points are chosen so that the results are improved.

Keywords: *frequency estimation, interpolation, algorithm, Discrete Fourier Transform, modal analysis*

1. Introduction

In numerous engineering applications involving measurements to estimate the frequencies of signals, such as damage detection [1], telecommunication [2], radar/sonar [3] it is crucial to accurately estimate the frequencies. Usually, the frequencies are estimated involving the Discrete Fourier Transform (DFT), but the results depend rather on the sampling strategy as on the frequency of the signal. In order to improve frequency readability, interpolation methods are used, with the help of which the maximum of the interpolation curve is determined. So, the frequency is given by the inter-line position of the maximum of the curve. These interpolation methods take into account the largest sample magnitude from DFT and one or two neighbors. Some methods use polynomial functions for interpolation [4,5], others an asymmetric *pseudo-sinc* function [6,7].

The literature presents interpolation methods based on different algorithms that use two or three points from the module spectrum [8]-[11] or the complex values of the spectrum [4,5,12]. When the accuracy of these interpolation methods is analyzed [6,13,14], it was found that in some of them, when the signal contains an integer number of cycles, the correct frequency is obtained [10,11], but there are also methods that introduce big errors in that case [9]. Among the latter methods we choose that developed by Jain, and here we present how it can be improved by se-

lecting the proper points for interpolation. We show, by comparing the results obtained with the original and improved algorithm, the superiority of the latter.

2. Jain's algorithm for frequency estimation

Let us consider a sinusoidal signal as a sampled sequence

$$a[n] = A \exp \left[j2\pi \frac{f_0}{f_s} n \right], n = 0, \dots, N-1 \quad (1)$$

where A is the amplitude, f_0 is the frequency of the signal, f_s is the sampling rate, N the number of acquired samples, n the index of the samples and $j^2 = -1$. From the sampling strategy, we obtain the distance between two spectral lines, i.e. the is the frequency resolution, that is:

$$\Delta f = \frac{f_s}{N} \quad (2)$$

The discrete Fourier transform DFT of $a[n]$ at spectral line k displays the amplitude:

$$A_k = \sum_{n=0}^{N-1} a[n] e^{-j(2\pi/N)nk} \quad (3)$$

In order to determine the true frequency at an inter-line position, Jain's algorithm involves two stages. In the first stage an index k of the largest magnitude samples $|A_k|$ from DFT is determined and in the second stage the target is finding a correction coefficient δ in the vicinity of k and determine the inter-bin frequency location (the corrected frequency) with the formula:

$$f_c = (k + \delta)\Delta f \quad (4)$$

To find the correction coefficient [11], Jain uses two points from the spectrum of modules. The method developed by Jain is based on the following algorithm:

1. Select the points for interpolation and calculate the amplitude ratio:

$$\text{if } |A_{k-1}| > |A_{k+1}|, \text{ then } \alpha_1 = |A_k| / |A_{k-1}|$$

$$\text{else, } \alpha_2 = |A_{k+1}| / |A_k|$$

2. Calculate the correction term:

$$\text{if } \alpha_1 \text{ is selected, then } \delta_1 = \alpha_1 / (1 + \alpha_1)$$

$$\text{else, } \delta_2 = \alpha_2 / (1 + \alpha_2)$$

3. Calculate the corrected frequency:

for δ_1 use the relation

$$f_c = (k - 1 + \delta_1)\Delta f \quad (5)$$

else, use the relation

$$f_c = (k + \delta_2)\Delta f \quad (6)$$

From numerous simulation we found out that the results obtained by involving this algorithm provides good results, except some signal time lengths for which the signal contains almost an entire number of cycles. In next section we show why the algorithm fails for these time lengths and how it can be improved.

3. Correction of Jain's algorithm

Thus, in the proposed algorithm, namely the corrected Jain's algorithm, the two points selected for interpolation must belong to the main lobe, even if the point that is the neighbour of the maximizer has a smaller amplitude as the second neighbour. In [17], an algorithm for selecting the two points with which we will correct Jain's algorithm is proposed. It involves following steps:

- Add $N_{ZP}=2$ points with zero amplitude to the original signal, it results a zero-padded signal
- Calculate the DFT for the zero-padded signal and determine the coordinates for the maximizer and its neighbors
- Subtract N_{ZP} points from the zero padded signal to obtain the original signal
- Calculate the DFT for the original signal and find the coordinates of the maximizer and its neighbors
- Select the proper neighbor
 - o if $|A_k^*| < |A_k|$ (where A_k^* the amplitude of the maximizer for the zero-padded signal) then the point with the amplitude $|A_k|$ is on the left side of the main lobe, the point with the amplitude $|A_{k-1}|$ is on a secondary lobe and the one with the amplitude $|A_{k+1}|$ is on the same lobe as the one with the amplitude $|A_k|$, so we will take for the algorithm the points having the amplitudes A_k and A_{k+1}
 - o else the points with amplitudes $|A_{k-1}|$ and $|A_k|$ are on the same lobe and we will take these points for the algorithm

Figure 1 shows such a case in which we will have to correct the algorithm proposed by Jain and choose the two points differently. This is the case where $|A_{k-1}| < |A_{k+1}|$ and so according to Jain's algorithm we should calculate α_2 based on

the amplitudes $|A_{k+1}|$ and $|A_k|$, then δ_2 and evaluate the frequency with formula (6).

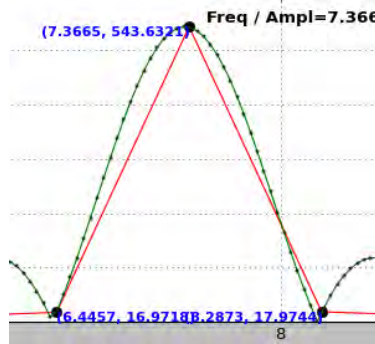


Figure 1. The three points in the DFT spectrum used for interpolation

However, it can be seen that the point having the amplitude $|A_{k+1}|$ is on a secondary lobe and thus we will consider the two points on the same lobe, those having the amplitudes $|A_k|$ and $|A_{k-1}|$, thus calculating α_1 , δ_1 and the frequency based on formula (5).

4. Results and discussion

To illustrate the above, we have chosen a signal generated with the given frequency of $f_{true} = 7.33$ Hz and amplitude $A_{true} = 1$, with a sampling rate $f_s = 1000$ samples/second. Over time interval of 0.3 s, between $t_i = 0.93$ s and $t_f = 1.23$ s we generated the signal. Thus, starting from 931 samples, adding 5 samples at a time, we finally obtained the signal generated with 1231 samples.

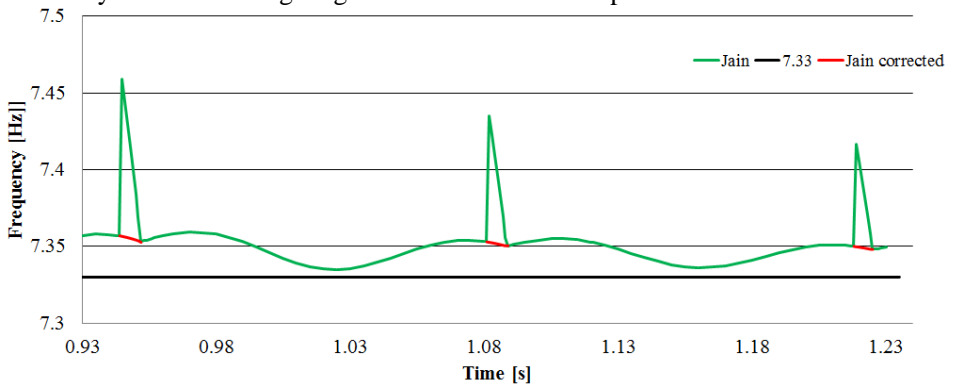


Figure 2. Frequencies estimated with Jain's algorithm and the corrected algorithm

Following the algorithm developed by Jain, we represented graphically (with green line in Figure 2) the estimated frequency using formulas (5) and (6). As we can see, in the area where we have an entire number of cycles this curve suffers a significant jump.

Starting first with $N=946$ samples and ending with $N=953$ samples (Figure 3), then from $N=1083$ samples to $N=1089$ samples (Figure 4) and from $N=1220$ samples to $N=1225$ samples (Figure 5), we chose differently the two points according to the correction algorithm proposed by Jain and presented in paragraph 2, and we obtained the curve with red line. A zoom on the area of interest is presented in figure 3 for 7 entire cycles, figure 4 for 8 cycles and figure 6 for 9 entire cycles.

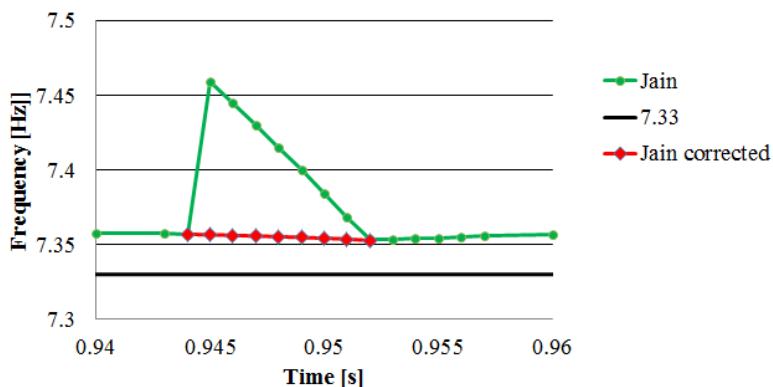


Figure 3. Frequencies estimated with the corrected Jain's algorithm (signal time length around 7 entire cycles)

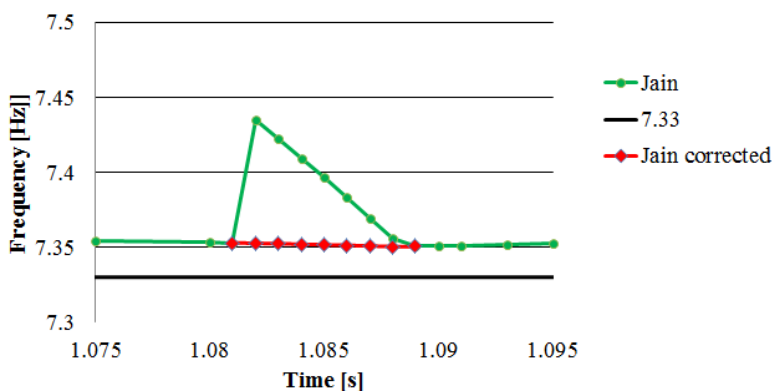


Figure 4. Frequencies estimated with the corrected Jain's algorithm (signal time length around 8 entire cycles)

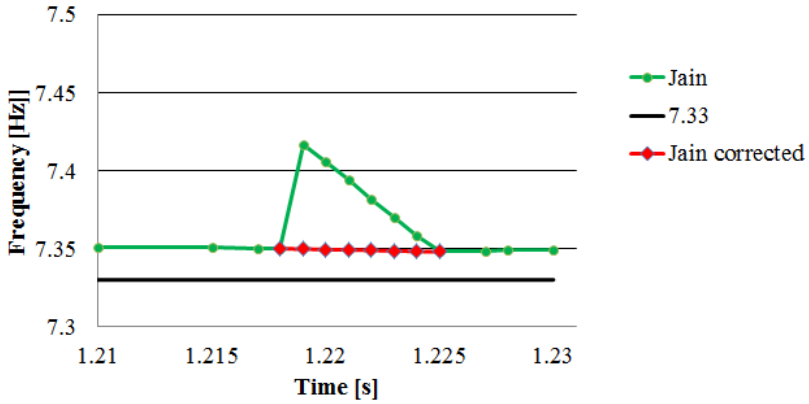


Figure 5. Frequencies estimated with the corrected Jain's algorithm (signal time length around 9 entire cycles)

From figures 3 to 5 one can observe that the error in estimating the frequencies decrease with increasing the time length of the analysed signal for the entire time length range. The improvement of the frequency readability with the corrected Jain's algorithm is obvious.

Table 1. Frequency estimation with Jain's algorithm and the corrected algorithm

T [s]	1.082	1.083	1.084	1.085	1.086	1.087	1.088
N	1083	1084	1085	1086	1087	1088	1089
A_{k-1}	25.21	21.113	17.078	13.103	9.188	5.333	1.541
A_k	541.88	542.765	543.540	544.208	544.769	545.225	545.57
A_{k+1}	25.521	21.748	17.894	13.960	9.948	5.861	1.704
f_{Jain} [Hz]	7.4352	7.42246	7.40947	7.39632	7.38299	7.36949	7.3558
ε_{Jain} [%]	1.437	1.261	1.084	0.905	0.723	0.539	0.352
f_{corr} [Hz]	7.3526	7.35231	7.35197	7.3516	7.35120	7.35079	7.35035
ε_{corr} [%]	0.308	0.304	0.300	0.295	0.289	0.284	0.278

The data used to plot figure 3 is given in table 1, where a special focus concerns the achieved errors. These are denoted as following: (*) the error obtained in estimating the frequency according to the method proposed by Jain is noted with ε_{Jain} ; (**) the error obtained in estimating the frequency according to the proposed correction method is denoted as ε_{corr} . One can observe in table 1 that the proposed correction algorithm makes the maximum error to be reduced from 1.43% as obtained by Jain to 0.3%.

5. Conclusion

The algorithm proposed by Jain that allows to improve frequency readability has been corrected in this paper for different time intervals in which an entire number of cycles occur. This improvement was made by selecting the points to be considered for interpolation so that they are on the same lobe.

References

- [1] Gillich G.R., Mituletu I.C., Praisach Z.I., Negru I., Tufoi M., Method to Enhance the Frequency Readability for Detecting Incipient Structural Damage, *Iranian Journal of Science and Technology, Transactions of Mechanical Engineering*, 41(3), 2017, pp. 233–242.
- [2] Johnson C., Sethares W., Klein A., *Software Receiver Design: Build Your Own Digital Communications System in Five Easy Steps*, 2011.
- [3] Knight W., Pridham R., Kay S., *Digital signal processing for sonar*, Proceedings of the IEEE, 69(11), 1981, pp. 1451–1506.
- [4] Jacobsen E., Kootsookos P., Fast, accurate frequency estimators, *IEEE Signal Processing Magazine*, 24(3), 2007, pp. 123-125.
- [5] Candan C., A method for fine resolution frequency estimation from three DFT samples, *IEEE Signal Processing Letters*, 18(6), 2011, pp. 351-354.
- [6] Gillich G.R., Minda A.A., Korca Z.I., Precise estimation of the resonant frequencies of mechanical structures involving a pseudo-sinc based technique, *Journal of Engineering Sciences and Innovation , A. Mechanics, Mechanical and Industrial Engineering, Mechatronics*, 2(4), 2017, pp. 37-48.
- [7] Minda A.A., Gillich G.R., Sinc Function Based Interpolation Method to Accurate Evaluate the Natural Frequencies, *Analele Universitatii „Eftimie Murgu“ Resita, Fascicula de Inginerie*, 24(1), 2017, pp. 211-218.
- [8] Grandke T., Interpolation Algorithms for Discrete Fourier Transforms of Weighted Signals, *IEEE Transactions on Instrumentation and Measurement*, 32, 1983, pp. 350-355.

- [9] Jain V.K., Collins W.L., Davis D.C., High-Accuracy Analog Measurements via Interpolated FFT, *IEEE Transactions on Instrumentation and Measurement*, 28, 1979, pp. 113-122.
- [10] Ding K., Zheng C., Yang Z., Frequency Estimation Accuracy Analysis and Improvement of Energy Barycenter Correction Method for Discrete Spectrum, *Journal of Mechanical Engineering*, 46(5), 2010, pp. 43-48.
- [11] Voglewede P., Parabola approximation for peak determination, *Global DSP Magazine*, 3(5), 2004, pp. 13-17.
- [12] Quinn B.G., Estimating Frequency by Interpolation Using Fourier Coefficients, *IEEE Transactions on Signal Processing*, 42, 1994, pp. 1264-1268.
- [13] Aboutanios E., Mulgrew B., Iterative frequency estimation by interpolation on Fourier coefficients, *IEEE Transactions on Signal Processing*, 53(4), 2005, pp. 1237-1242.
- [14] Belega D., Petri D., Frequency Estimation by Two- or Three-Point Interpolated Fourier Algorithms based on Cosine Windows, *Signal Processing*, 114, 2015, pp. 115–125.
- [15] Minda A.A., Gillich N., Mituletu I.C., Ntakpe J.L., Mănescu T., Negru I., Accurate Frequency Evaluation of Vibration Signals by Multi-Windowing Analysis, *Applied Mechanics and Materials*, 801, 2015, pp. 328-332.
- [16] Xiang J.Z., Qing S., Wei C., A novel single tone frequency estimation by interpolation using DFT samples with zero-padding, *Proc. IEEE ICSP*, Chengdu, China, Mar. 2017, pp. 277-281.
- [17] Gillich G.R., Nedelcu D., Minda A.A., Lupu D., *An algorithm to find the two spectral lines on the main lobe of a DFT*, 43rd International Conference on Mechanics of Solids, 2019, pp.44-49.

Addresses:

- Lect. Dr. Andrea Amalia Minda, Babeş-Bolyai University, Faculty of Engineering, Piața Traian Vuia, nr. 1-4, 320085, Reșița, a.minda@uem.ro
- PhD student David Lupu, Babeş-Bolyai University, Faculty of Engineering, Piața Traian Vuia, nr. 1-4, 320085, Reșița, david.lupu@student.uem.ro
- Prof. Dr. Eng. Gilbert-Rainer Gillich, Babeş-Bolyai University, Faculty of Engineering, nr. 1-4, 320085, Reșița, gr.gillich@uem.ro
(* corresponding author)

Study for monitoring of the insulation stator winding of the hydro generators using a data acquisition system

Mihaela Molnar, Eugen Răduca*

The paper presents a study for a system for data acquisition in order to monitor online the state of the insulation stator winding of hydro generators, using the LabVIEW graphical programming language. The data acquisition system allows the acquisition of the quantities of interest in the process and at the same time, through it, the creation of a strong database for the current state of the hydro generator insulation.

Keywords: *insulation, stator, data acquisition, LabVIEW*

1. Introduction

During operation, the insulation of the stator winding of the wind turbines is subjected to electrical, thermal, mechanical and environmental stresses. Due to these stresses, the properties of the insulation change and, over a longer period of time, the physical characteristics - including the electrical ones - worsen. [1].

The term "insulation aging" means the gradual degradation (deterioration) of insulating properties. This aging process will lead to a worsening of the reliability of the electrical insulation, characterized by a rate of failure over time.

The causes of the aging of the insulation consist in the irreversible physical-chemical changes in the electrical insulating materials, due to the exploitation demands and, first of all, due to their thermal stresses.

The aging of the insulation is predetermined, first of all, by the temperature of the insulation, due to the facilitation of the development conditions and the increase of the speed of the chemical reactions in the material at high temperature. The higher the temperatures of the electrical insulating materials, the more molecules enter the chemical reaction, thereby intensifying the aging phenomena of the insulation [5].

The influence of the electric field intensity on the aging of the insulation compared to the temperature is significantly lower, but noticeable in certain materials.

The intensity of the electric field directly influences, in other cases indirectly, the aging of the insulation, through the chemical and mechanical effect of the local non-destructive discharges (from or on the surface of the electrical insulating materials) [6].

2. System for the acquisition of quantities of interest in the stator windings of hydro generators in the LabVIEW graphic programming language

2.1. Block diagram of the assembly

The block diagram of the production platform - data acquisition system assembly is presented in figure 1.

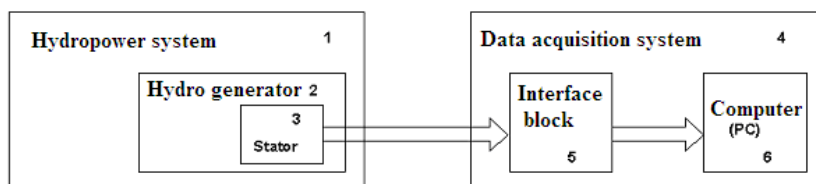


Figure 1. The block diagram of the production platform - data acquisition system assembly

The production platform is represented by the hydropower system 1, in which the hydrogen generator 2 constitutes a subsystem thereof. The component directly targeted for monitoring is its stator.

For some of the stator parameters monitoring is possible (temperature at various points, working voltage), but others can not be known permanently (insulation thickness at each coil) but only when the machine is overhauled [4].

The data acquisition system - 5 - allows the continuous collection and storage of parameters that can be measured directly and continuously.

2.2. The structure of the system

The sizes of interest at the stator windings of the hydro generators are:

- stator winding temperature
- the current in the stator
- electrical voltage of the stator

They are purchased with the following main purposes:

- their monitoring;
- knowledge and processing of information during the operation of hydro generators;

- knowledge and processing of information in hydro generator tests;
- control and regulation of the correct operation of the hydro generators.

Figure 2 shows the structure of a data acquisition system with an analog input signal [3].

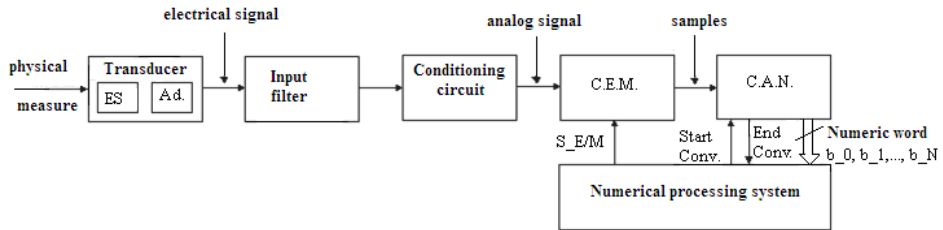


Figure 2. The structure of a data acquisition system with an analog input signal

Where:

- ES – sensitive element;
- Ad. – adapter;
- C.E.M. – sampling and storage circuit;
- C.A.N. – digital to analog converter
- Conv. – conversion

This data acquisition system was used to monitor the quantities of interest in the stator windings of the hydro generators.

2.3. Presentation of the program in the graphic programming language LabVIEW

Figure 3 shows the application we called MWM-AQ-DW1.VI designed built for data acquisition from stator [7].

The program is of graphic type, made in LabVIEW [2] and has two interdependent components figure 3.a - Front panel and figure 3.b - Block diagram.

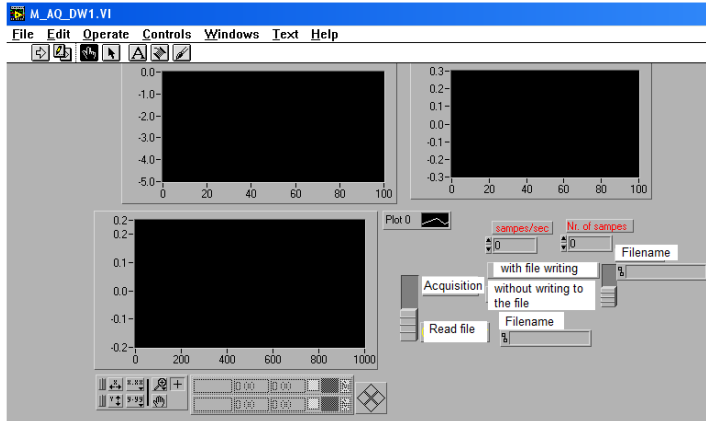
The operation on the program is done from the computer, acting directly on the front panel.

From the block diagram it can be seen that the program was designed for the simultaneous analysis of data in simple precision, on 3 channels, marked channel 0, channel 1 and channel 2.

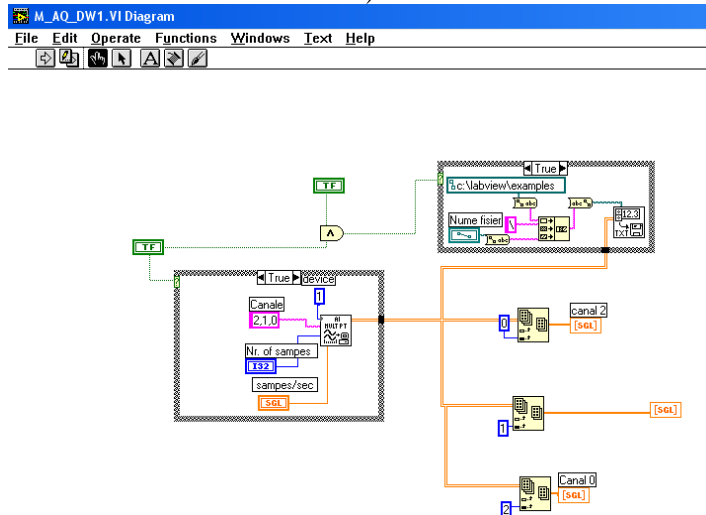
The DI Mult PI command (shown in figure 3.b) is a strong one, being possible the choice by the operator from the front panel (figure 3.a) of the total number of samples purchased, as well as the number of samples purchased in the unit of time.

The accuracy and speed of sampling are primarily conditioned by the acquisition plate used [8]. An NI LabPC + type acquisition board was used.

The board proved to be suitable for the proposed purpose, namely to monitor the insulation temperature as well as the voltage and current in the stator.



a)



b)

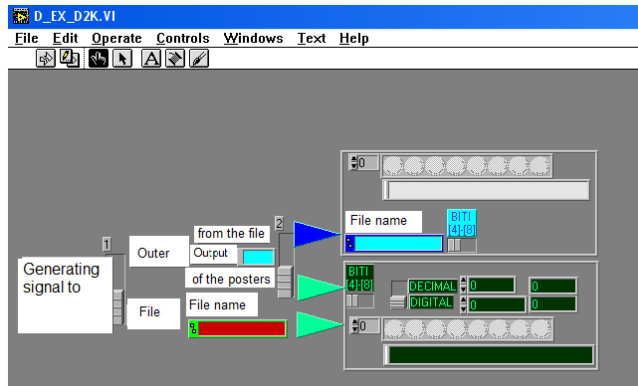
Figure 3. Program for the acquisition of data of interest sizes:

a) Front panel; b) Block diagram

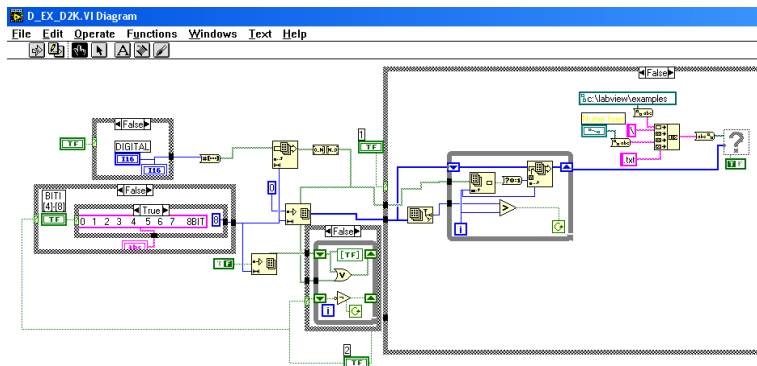
The front panel contains three plotter indicator instruments through which each of the three measured sizes of interest can be viewed at the same time and can be stored or not in a file (through the "write acquisition" and "acquisition selections without write in the file").

Acquisition sizes can be read later at any time from the file in which they were stored ("read file").

Another problem that had to be solved was the transmission of data from the file to another peripheral of the PC where the acquisition was made. For this purpose, the program called D_EX_D2K.VI was designed, whose front panel is given in figure 4. a, and the associated block diagram in figure 4. b.



a)



b)

Figure 4. Data transmission program between the acquisition system and the monitoring system: a) Front panel; b) Block diagram

Through this program the data acquired in the original file can be transmitted to another file via the "Generate signal to file" button. The transmission can be done externally, through the parallel port of the PC, or in another file in the PC.

3. Conclusions

This program is the development of a program that the authors used to measure electrical quantities.

The design and implementation of a monitoring system for determining the state of the insulation has led to the possibility of preventing the destruction of the hydro generator as a result of the destruction of the insulation during its operation.

The data acquisition system allows the acquisition of the measured sizes of interest in the process and at the same time, through it, the creation of a strong database for the current state of the hydro generator insulation.

References

- [1] Boulter E.A., Stone G.C., Historical development of rotor and stator winding insulation materials and systems, *IEEE Electrical Insulation Magazine*, 20(31), pp. 25–39, 2004.
- [2] Bujoreanu C, *LABVIEW, prietenul nostru*, Iași, 2015.
<https://mec.tuiasi.ro/diverse/labview.pdf>
- [3] Ciascai I., *Sisteme de achiziție de date pentru calculatoare personale*, Editura Albastră, Cluj-Napoca, 1998.
- [4] David V, *Masurarea marimilor electrice și neelectrice*, Universitatea Tehnică „Gh Asachi” Iași, 2015.
- [5] Drăgănescu O., *Încercările mașinilor electrice rotative*, Editura Tehnică, București, 1987.
- [6] Horvath T., ș.a., *Încercarea izolației electrice*, Editura Tehnică, București, 1982.
- [7] Răduca M., *Contribuții la identificarea, modelarea și simularea sistemelor de izolație ale hidrogenatoarelor*, Editura Politehnica, Timișoara, 2007.
- [8] Selisteanu D., Petre E., *Instrumentație virtuală. Aplicații de prelucrare numerică a semnalelor*, Editura MATRIXROM, București, 2010.

Addresses:

- Assist. Prof. Dr. Eng. Mihaela Molnar, Babeș-Bolyai University, Faculty of Engineering, nr. 1-4, 320085, Reșița, m.molnar@uem.ro
- Prof. Dr. Eng. Eugen Răduca, Babeș-Bolyai University, Faculty of Engineering, Piața Traian Vuia, nr. 1-4, 320085, Reșița, e.raduca@uem.ro
(* corresponding author)

Three-Axis Level with WiFi Connection

Cristian-Mircea Muscai, Ion-Cornel Mituletu*, Tiberiu Manescu, Liviu-Bogdan Protea

The Three-Axial Level (TAL) device measures the angular inclination around the three axes of the orthogonal system. It consists of a triple-axis magnetometer sensor with I²C transmission and a NodeMCU V3 development board with WiFi module integrated. The device processes data from sensor, displays it on its screen and also transmits the angular values to various PADs (Portable Access Device). The experimental testing confirmed the initial expectation, showing the properly on-site operation of the designed device. This device is useful in the supervising process to avoid perturbing the worker that performs the leveling operation or when the working place is hard to reach.

Keywords: ESP8266, NodeMCU V3, OLED display, standalone web server, triple-axis magnetometer

1. Introduction

Wireless devices and systems create a smart environment by connecting sensors and transducers to develop various industrial and home automation / domotics applications. These equipments are usually embedded and can work independent or integrated in a larger system. Also, the internet provides the possibility to connect a large number of things (Internet of Things - IoT), devices and systems, resulting in smart virtual grids able to exchange important amount of data allover the world.

Based on low-cost development boards and sensors lately they were developed a large gamma of new gadgets, systems, algorithms and software.

As the first example, a cost-effective and efficient system designed to monitor drinking water quality which makes use of Internet of Things (IoT) technology is given. This system consists of several sensors to measure various water parameters and a microcontroller unit interfaced with these sensors, and further processing is

performed at personal computer. The obtained data is sent to the cloud by using IoT based ThinkSpeak application to monitor the quality of the water [1].

Also with the use of IoT platform and visual analytics, a real-time water consumption monitoring system has been developed for household and commercialized building applications. In order to get the water consumption data, a Hall Effect water flow sensor is attached to every faucet, which is then processed by a NodeMCU, then pushed to the Heroku cloud database [2].

In other paper are presented and analyzed the design and implementation aspects of open source Supervisory Control and Data Acquisition software. Case uses of the software are also discussed, mostly focusing in embedded computational platforms and microcontroller-based prototyping boards. The main objective of this software is to provide a low cost, open source and extensible tool for open source and scientific users [3].

Short Term Load Forecasting (STLF) is an essential aspect for smart grid operations such as power dispatch and load management. Therefore, cost effective Arduino Uno, Node MCU/ESP8266, PZEM 004T and DHT 11 sensors are used to achieve the hardware model that acquire the data for a novel online load forecasting, using supervised Machine Learning (ML), algorithms in Internet of Things (IOT) environment [4].

In this paper the accomplishment of a device which measures the angular values around three orthogonal axes is presented. Two of the axes define the absolute horizontal plane, and the third is along the gravitational acceleration direction. Also, the device features ensure the hold of real-time values, recalibration to zero at any desired angle value and wireless data transmission to PADs, mobile devices like phone, tablet and laptop. Zero calibration at any value offers an easier way to repetably achieve an desired angle value, like 13.7 degrees.

2. Design of the device

The device's structure shows the functional principle and does not intend to limit it at the use of these components, because their properly replace can produce higher performances. Thus, the block diagram is presented in figure 1.

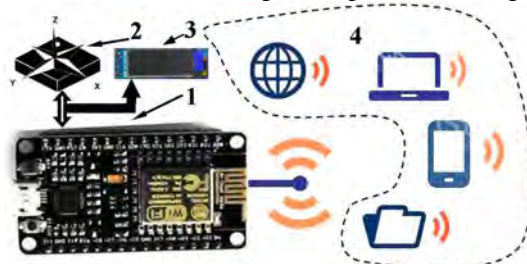


Figure 1. Device block diagram.

The structure from figure 1 is based on NodeMCU V3 development board (1), the values of the angles are given by the triple-axis magnetometer sensor (2), after the processing of the values they are shown on the display (3), and in area (4) the symbols of the PADs are presented, which are the mobile devices possible to connect.

The most significant features of the components are given below:

1. NodeMCU V3: the development board equips the ESP-12E module containing ESP8266 chip having Tensilica Xtensa® 32-bit LX106 RISC microprocessor which operates at 80 to 160 MHz adjustable clock frequency and supports RTOS. There's also 128 KB RAM and 4 MB of Flash memory (for program and data storage) just enough to cope with the large strings that make up web pages, JSON/XML data, and everything we throw at IoT devices nowadays. The ESP8266 Integrates 802.11b/g/n HT40 Wi-Fi transceiver, so it can not only connect to a WiFi network and interact with the Internet, but it can also set up a network of its own, allowing other devices to connect directly to it. It has a total of 17 GPIO pins broken out to the pin headers on both sides of the development board. These pins can be assigned to all sorts of peripheral duties, including:

- A 10-bit ADC channel;
- UART interface is used to load code serially;
- PWM pins for dimming LEDs or controlling motors.
- SPI and I²C interface to link up all sorts of sensors and peripherals, and I²S interface if you want to add sound to your project.

2. Triple-axis magnetometer sensor QMC5883L is based on state-of-the-art, high resolution, magneto-resistive technology. Along with custom-designed 16-bit ADC ASIC, it offers the advantages of low noise, high accuracy, low power consumption, offset cancellation and temperature compensation. It enables 1° to 2° compass heading accuracy. The I²C serial bus allows for easy interface.

3. Display is a 128x32 pixel monochrome OLED. It is small, only about 1" diagonal, but very readable due to the high contrast and contains 128x32 individual white OLEDs, each one is turned on or off by the controller chip. Because the display makes its own light, no backlight is required, the power required to run the OLED is reduced.

Programming NodeMCU by ArduinoIDE requires a few steps. These are shortly presented below, more detailed aspects are given in the article "NodeMCU V3 For Fast IoT Application Development" [5]:

1. Installing the firmware;
2. Preparing the Arduino IDE;
3. Source code elaboration.

To easily achieve the source code, a flowchart must be realized based on the logical functionality of the device and also each component added to the develop-

ment board has to be tested separately, hardware and software. In the initial testing process a few important things have to be highlighted:

- variants of sensors are on the market that seem to be the same, but they are not, therefore the correct software must be identified, and sometimes this is not easy;

- attention has to be drawn to the component wiring, else ambiguous behavior could appear;

- I²C right addresses have to be identified, for this an I²C scanner can be used, it is easy to find on the internet.

A simplified flowchart is presented in figure 2, it defines just the important functional aspects.

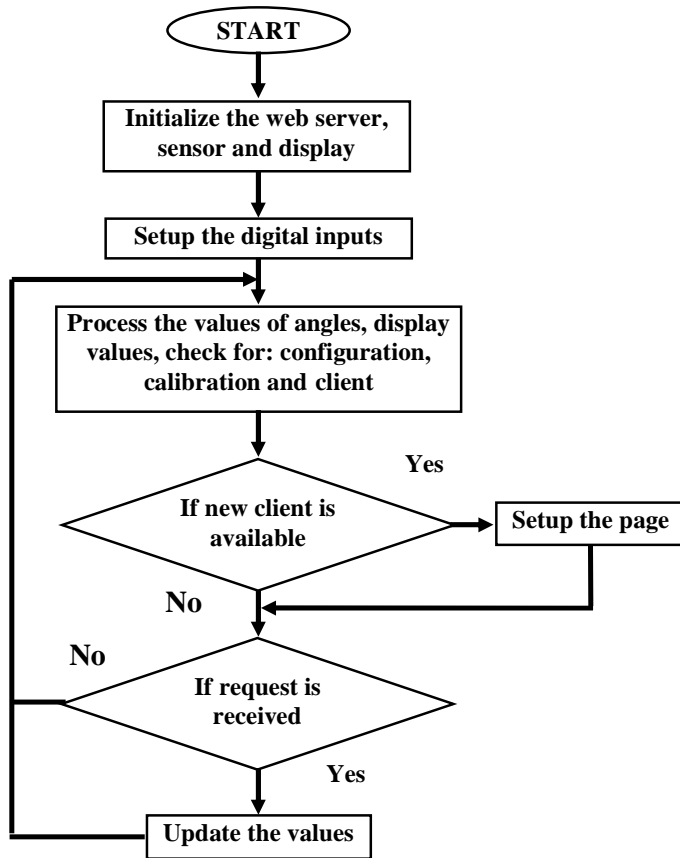


Figure 2. Operation flowchart.

As the flowchart shows the device operation is based on getting the values of angles, their processing and displaying, checking the request of operator for calibration or new configuration, and checking for new wireless network client or requests from the older. The sensor and display are linked on I²C bus, thus at initialization their serial addresses have to be firstly verified. Also, in the initialization stage the digital inputs of the two buttons must be defined.

The most important aspects considered in the hardware design were the position and the fixing of the sensor, the development board placing and the required quantity of energy for long operation. After tests, the continuous operation period was determined as exceeding five days. Power supply is ensured by two series rechargeable batteries, each one having the voltage range between 3.6 and 4.2 V.

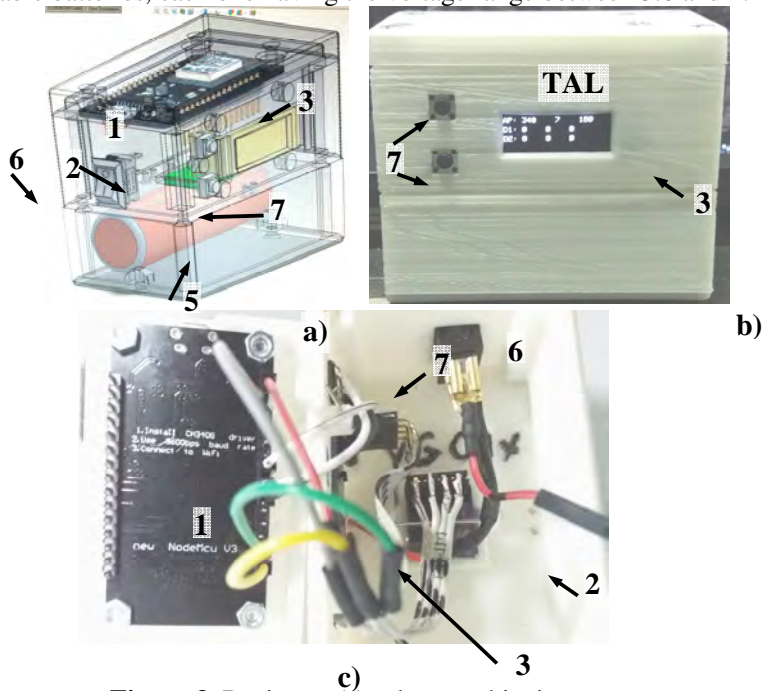


Figure 3. Design and hardware achieving aspects.

The design and hardware dimension were established in SolidWorks, resulting in the assembly form figure 3 a. Device box was presented in a transparent form in order to easily identify the place of the components. In this way, the design was completed by a power switch (6), two push buttons for manual operation (7), up button is assumed as Menu and down button as Select, and batteries (5).

Figure 3.b. depicts the final hardware version, the device box components were accomplished by 3D printing from PLA filament. How the internal connections have been made it is presented in figure 3.c.

Connection diagram is not presented because it is simple. It consists of connecting the SCL and SDA pins, from sensor and display, to the D1 and D2 pins of the development board. Buttons Menu and Select are connected to D14 and D12, acting when they are linked to ground, because the corresponding digital pins are set as digital inputs in pull up mode in the source code.

The most significant aspects in the source code achieving are presented below:

1. ESP8266 acts as Web Server, it can also set up a network by itself. This is possible because it can operate in three different modes: station, soft access point, and both in the same time. This last feature provides the possibility to build mesh networks. As station (STA), it gets IP and can setup a web server, delivering web pages to all connected devices. As soft access point (soft-AP), it creates its own network and acts as a hub for maximum five stations. It does not have interface to a wired network, the mode of operation is called soft access point [6].

2. In the main loop, as server it must handle clients, but more than that it has to do, in this case, the processing of the incoming angular values, displaying the results, and also checking the requests for calibration or configuration;

3. A good way to get some more efficiency is to optimize the number of page charging to the clients. Thus, the auto page refresh can be changed to dynamically load data by AJAX (Asynchronous Javascript And Xml) method. The method provides requesting data from the server asynchronously, in the background, without refreshing the page.

The device was set as soft-AP, so the network is created by itself, at first connection to a new client it sets the browser page and afterwards just updates the values by AJAX method.

AJAX uses a combination of a browser built-in XMLHttpRequest object, to request data from a web server, and JavaScript and HTML DOM, to display or use the data. AJAX applications might use XML to transport data, and they can transport data as plain text or JSON text. AJAX allows web pages to be updated asynchronously by exchanging data with a web server by updating parts of a web page, without reloading the entire page.

3. Testing the device

The testing of the device showed important aspects about how the network made by the device working as soft-AP and the other mobile devices as clients is working. In this regard, it must be specified the device can work stand alone, without any network, but waits for clients. At the connection moment a small gap was observed in the running of the device, it slows down. This gap increased if more

external devices were trying to connect at the same time. AJAX method drastically improved the running speed after connecting to an external device has been performed. Auto refreshing the page of the client produced slow running of the entire network, the number of updates decreasing to less than 10 per second, for three external device connected. AJAX increased this number to more than 20 per second, for five connected devices.

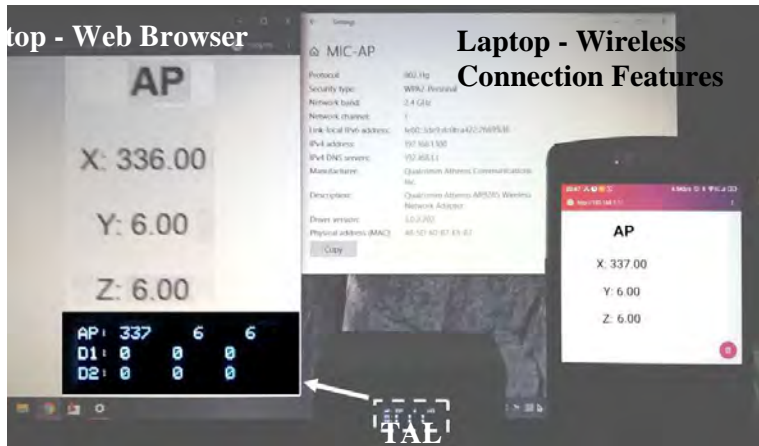


Figure 4. Device testing.

Figure 4 presents one of the testing way, which consisted of the device (TAL), laptop and mobile phone. The small difference between TAL's values and laptop is due to transmitting delay and vibration induced by the laptop to the TAL.

4. Conclusion

TAL device designed and presented can be useful in the supervising process to avoid the perturbation of the worker during operation, and helps when the working place is harder to reach by others.

As running frequency, TAL can transmit more than 20 updated values for each angle, being connected to maximum five PADs.

This device offers data protection and friendly connection to any PAD, and further it can easily be enriched with low-cost component to store data on memory stick, as .csv files.

Acknowledgement. The work has been funded by the Operational Programme Human Capital of the Ministry of European Funds through the Financial Agreement 51675/09.07.2019, SMIS code 125125.

References

- [1] Pasika S., Gandla S.T., Smart water quality monitoring system with cost-effective using IoT, *Heliyon - Contents lists available at ScienceDirect*, (<https://doi.org/10.1016/j.heliyon.2020.e04096>), 2020.
- [2] Tasonga A.C.,Abaob R.P., *Design and Development of an IoT Application with Visual Analytics for Water Consumption Monitoring*, 4th International Conference on Computer Science and Computational Intelligence, Sept. 12–13, 2019, pp. 205-213.
- [3] Scholl M.V., Rocha C.R., Embedded SCADA for Small Applications, *IFAC - PapersOnLine*, 49(21), 2016, pp. 246-253.
- [4] Pratapa Rajua M., Jaya Laxmib A., IOT based Online Load Forecasting using Machine Learning Algorithms, *Procedia Computer Science*, 171, 2020, pp. 551-560.
- [5] Al Dahoud A., Fezari M., NodeMCU V3 For Fast IoT Application Development, <https://www.researchgate.net/publication/328265730> (downloaded at August 21st, 2020).
- [6] ESP32 Web Server with Arduino IDE, <https://randomnerdtutorials.com/download/> (downloaded at August 22nd, 2020).
- [7] The World's Largest Web Developer Site, XML AJAX, https://www.w3schools.com/xml/ajax_intro.asp (downloaded at August 23rd, 2020).

Addresses:

- PhD. Stud. Eng. Cristian-Mircea Muscai, Babeş-Bolyai University, Faculty of Engineering, Piaţa Traian Vuia, nr. 1-4, 320085, Reşiţa, c.muscai@uem.ro
- Lect. PhD. Eng. Ion-Cornel Mituletu, Babeş-Bolyai University, Faculty of Engineering, Piaţa Traian Vuia, nr. 1-4, 320085, Reşiţa, mituic@yahoo.com
(* corresponding author)
- Assoc. Prof. Dr. Habil. Eng. Tiberiu Manescu, “Aurel Vlaicu” University of Arad, B-dul Revoluţiei, nr. 77, 310130, Arad, manescu.tiberiu@gmail.com
- PhD. Stud. Eng. Liviu-Bogdan Protea, Babeş-Bolyai University, Faculty of Engineering, Piaţa Traian Vuia, nr. 1-4, 320085, Reşiţa, b.protea@uem.ro

Estimation of the severity of damage produced by a transverse crack

Marius-Vasile Pop, Gilbert-Rainer Gillich*, Cristian Tufisi, Zeno-Iosif Praisach, Lucian Păun

This paper presents a method to find the severity of a crack for cantilever beams that can be used to estimate the frequency drop due to the crack. The severity is found for the crack located at the location where the biggest curvature (or bending moment) is achieved. Because the fixing condition does not permit a symmetrical deformation around the crack, the apparent severity is smaller as the real one. The latter is found by the estimated value of the trend-line at the fixed end, it being constructed on points that consider the crack position (equidistant points in the proximity of the fixed end) and the resulted deflections.

Keywords: *cantilever beam, transverse crack, damage severity, deflection, statistical method*

1. Introduction

Knowing the mathematical relation that express the damage severity in respect to the damage depth is essential when the estimation of frequency drop due to cracks is targeted. There are many functions to calculate the damage severity, all being deduced from fracture mechanics. Among the first attempts to express the frequency of damaged beams we mention [1]; further authors focused on finding the severity dependency on crack depth [2] - [5]. Newer research developed this domain [6]. The topic is even the subject of PhD theses, see for instance [7]. However, one of the most reliable relation is given in [8]. In our previous research we approached this topic and found a relation to express the frequency of cracked beams in respect to the damage severity [9] - [11]. The severity is found involving Castigliano's second theorem [12], and it was shown that the severity does not directly depend on the moment of inertia of the damaged cross-section [13].

In this paper we propose a different approach, that involves an energy method, the loss of capacity of the beam to store energy being expressed with help of the free end deflection of the beam under dead load.

2. The damage severity

In this section we introduce the damage severity $\gamma(\bar{a})$, which reflects the effect of a crack with depth a to a prismatic cantilever beam with width b and thickness h . The beam has length L and the crack is transversal and located at the larger face of the beam. We denoted the relative crack depth $\bar{a} = a/h$. According to [14], the damage severity is calculated as:

$$\gamma(\bar{a}) = \frac{\sqrt{\delta_{(0,a)}} - \sqrt{\delta_U}}{\sqrt{\delta_{(0,a)}}} \quad (1)$$

where δ_U is the deflection at the free end of the intact beam, and $\delta_{(0,a)}$ is the deflection at the free end of the beam with a crack of depth a at the fixed end (namely at distance $x=0$). Because at the fixed end the deformation manifests just on one side of the crack, the severity achieved here is smaller as that expected. To this aim, we simulate cracks at different positions near the fixed end, and find the theoretical severity from the linear regression curve.

The beam has the geometry and mechanical parameters (taken from the ANSYS library for Structural Steel) presented in table 1.

Table 1. Beam geometry and mechanical parameters

L (m)	b (mm)	h	E	ρ	ν
1000	20	5	2×10^{11}	7850	0.3

The crack positions x_i set in this study are presented in table 2. For all positions, a series of crack depths a_j indicated in table 3 are considered. The width of the crack is always 0.04 mm.

Table 2. Positions of the crack relative to the fixed end

i	0	1	2	4	5	6	7
x_i (mm)	6	8	10	12	14	16	18

Table 3. Depth of the crack

j	0	1	2	4	5	6
a_i (mm)	0.2	0.4	0.6	0.8	1	1.2
j	7	8	9	10	11	12
a_i (mm)	1.4	1.6	1.8	2	2.2	2.4

3. Calculation of the free end deflections

We performed simulation with ANSYS software. The beam was meshed with elements that have the maximum size of the edge 2 mm. For the intact beam, we obtained the deflection $\delta_f = 23.046$ mm at the free end, while for the damage cases the deflections at the free end of the beam are deduced from figures 1 and 2. The trend lines are plotted here and the associated mathematical relations provided together with. Actually, the deflections in these figures are found from the values of the trend line at the distance $x=0$ calculated with the corresponding mathematical relations. Eventually, the estimated deflections for the crack located at the fixed end are given in table 4.

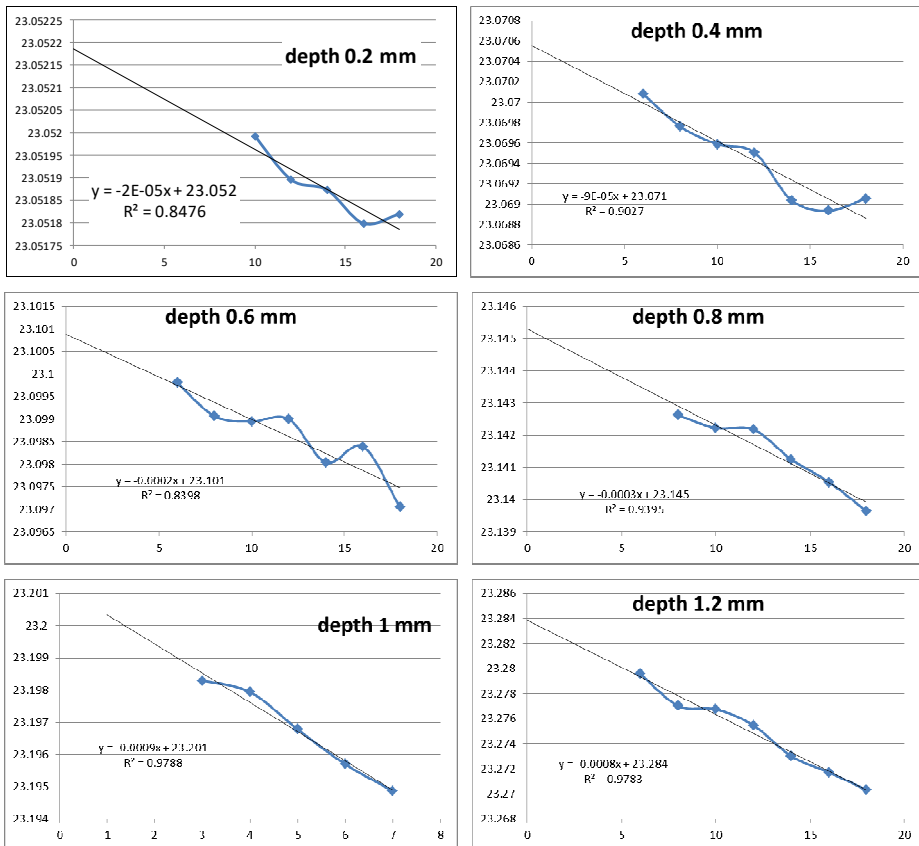


Figure 1. Regression curves for the crack depths 0.2 to 1.2 mm

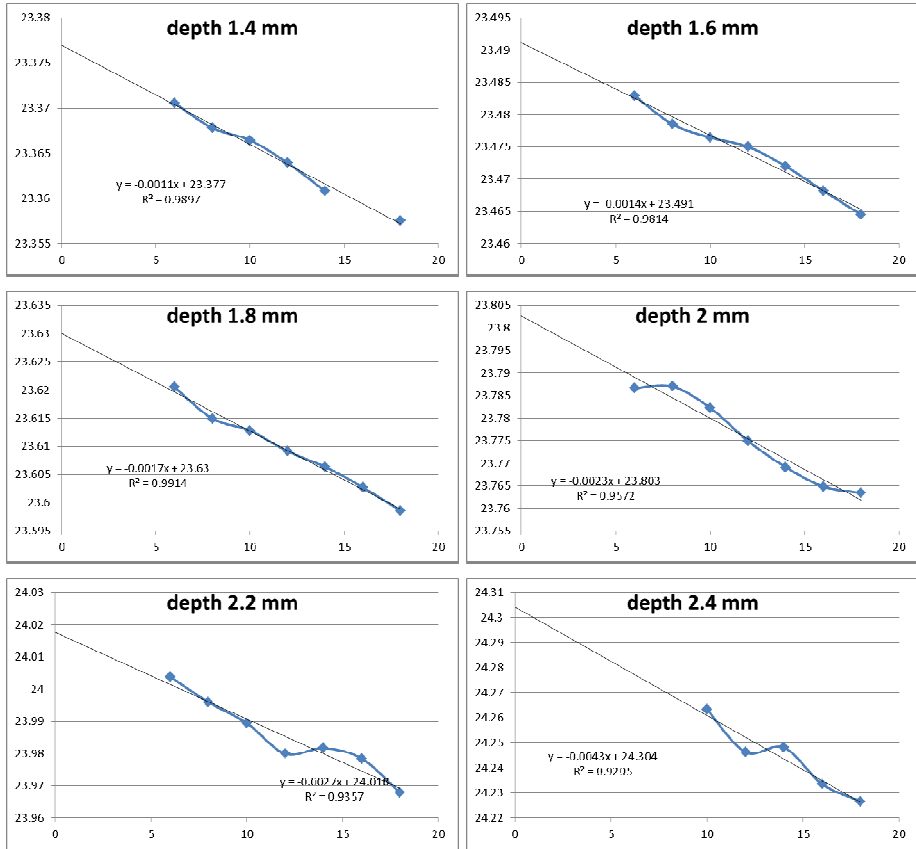


Figure 2. Regression curves for the crack depths 0.2 to 1.2 mm

Table 4. The deflections found for the considered crack depths

a (mm)	0.2	0.4	0.6	0.8	1	1.2
\bar{a} (mm)	0.04	0.08	0.12	0.16	0.2	0.24
$\delta_{(0,a)}$ (mm)	23.052	23.071	23.101	23.145	23.201	23.284
$\gamma(a)$ (mm)	0.00013	0.000542	0.001191	0.002141	0.003346	0.005124
a (mm)	1.4	1.6	1.8	2	2.2	2.4
\bar{a} (mm)	0.28	0.32	0.36	0.4	0.44	0.48
$\delta_{(0,a)}$ (mm)	23.377	23.491	23.63	23.803	24.018	24.304
$\gamma(a)$ (mm)	0.007105	0.009517	0.012434	0.01603	0.020444	0.026224

In table 4, along with the deflections, we show the values of the damage severity calculated with relation (1).

4. The severity evolution with the damage depth

With the data from table 4 we plot a diagram, figure 3, which represents the evolution of the damage severity with the crack depth. On these points we construct a trend line, as a fourth-order polynomial, and find its mathematical expression. This is given in relation (2).

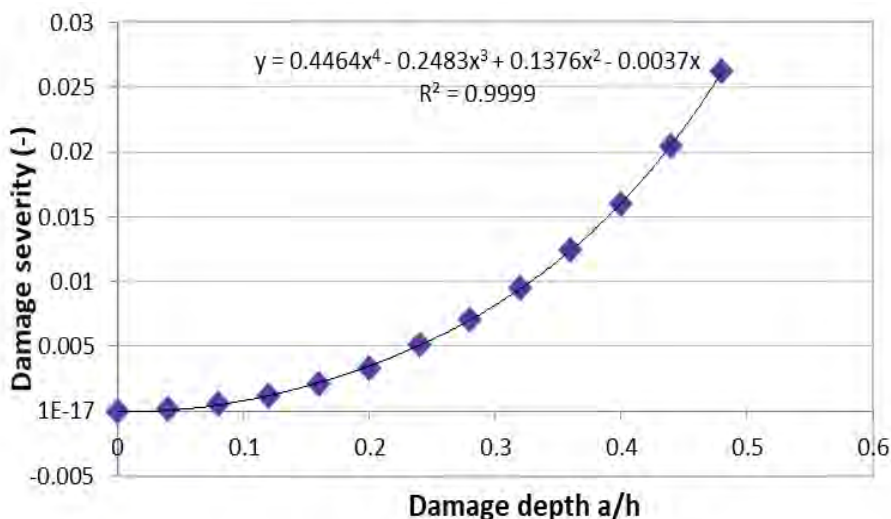


Figure 3. The evolution of the damage severity with the crack depth

One can observe that the curve is forced to start from point (0,0), which reflects the real situation; for no damage the deflection increase is inexistent and thus the severity is zero.

$$\gamma(\bar{a}) = 0.4464\bar{a}^4 - 0.2483\bar{a}^3 + 0.1376\bar{a}^2 - 0.0037\bar{a} \quad (2)$$

A comparison with curves developed by other authors, figure 4, show the reliability of the proposed severity. Note that, the way how the curve is found by the proposed method is simple and fast, dissimilar to the approach of actual methods that use a big number of experiments. In addition, their severity functions depend on the material characteristics, which means that incorrectly determined/involved material characteristics affect the precision of the function.

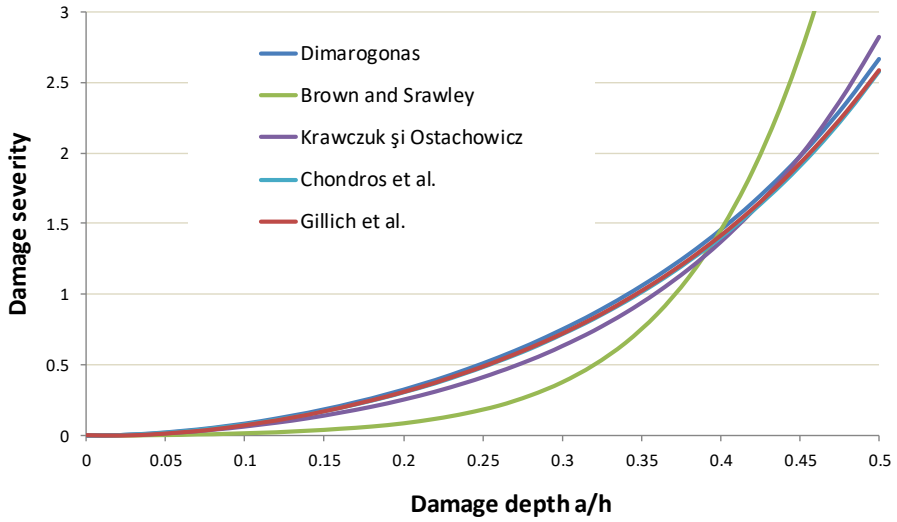


Figure 4. Comparison of different damage severity curves

As a second version of the damage severity curve, we plot the severity in function of the thickness ratio of the damaged and undamaged beam, namely $1 - \bar{a}$.

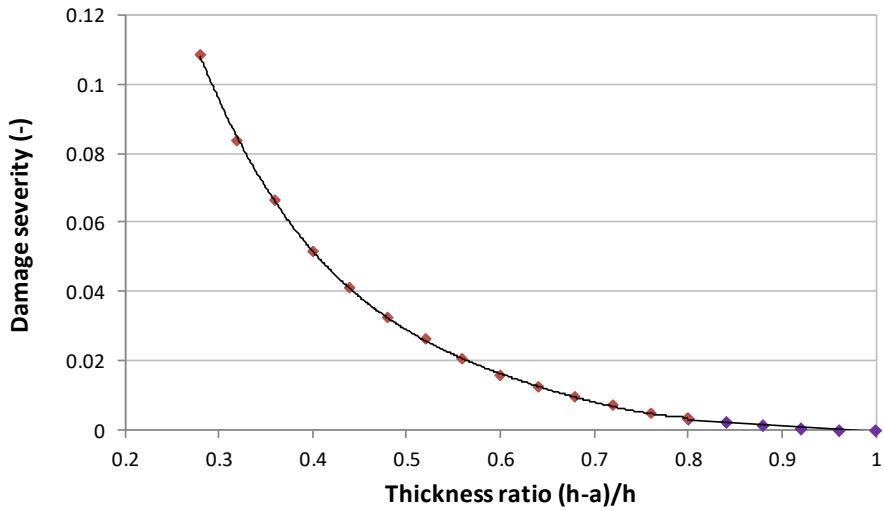


Figure 5. The evolution of the damage severity with the thickness ratio

For this curve, one can observe that two intervals for interpolation are necessary, one for a small crack and the second for a deeper crack.

4. Conclusion

The paper proposes a mathematical relation to calculate the severity of a crack with help of the deflection of the cantilever beam under dead load deduced for the intact and damaged beam, respectively. The severity increases with the damage depth, the relation being a fourth-order polynomial curve. We also found out that for the curve expressed in respect to the thickness ratio, two intervals of interpolation are requested: one for the incipient cracks and the second for serious damages.

Further research aims to find the damage severity curves for beams that have different cross-section, among which we mention the hexagonal, circular or elliptic shapes. In next research, we will also consider the cases of open and closed cross-sections as I- or T-beams or pipes.

References

- [1] Thomson W.J., Vibration of slender bars with discontinuities in stiffness, *Journal of Applied Mechanics*, 17, 1943, pp. 203-207.
- [2] Liebowitz H., Vanderveldt H., Harris DW., Carrying capacity of notched column, *International Journal of Solids and Structures*, 3(4), 1967, pp. 489-500.
- [3] Liebowitz H. Claus Jr. W.D.S., Failure of notched columns, *Engineering Fracture Mechanics*, 1(1), 1968, pp. 379-383.
- [4] Rizos P.F., Aspragathos N., Dimarogonas A.D., Identification of Crack Location and Magnitude in a Cantilever Beam from the Vibration Modes, *Journal of Sound and Vibration*, 138(3), 1990, pp. 381-388.
- [5] Dimarogonas A.D., Vibration of cracked structures - A state of the art review, *Engineering Fracture Mechanics*, 5, 1996, pp. 831-857.
- [6] Bilello C., *Theoretical and Experimental Investigation on Damaged Beams under Moving Systems*, Ph.D.Thesis, Universita` degli Studi di Palermo, Italy, 2001.
- [7] Ostachowicz W., Krawczuk M., *On modelling of structural stiffness loss due to damage*, in DAMAS 2001: 4th Int. Conf. Damage Assessment of Structures, Cardiff, UK, 2001, pp. 185-199
- [8] Chondros T.J., Dimarogonas A.D., Yao J., A continuous cracked beam vibration theory, *Journal of Sound and Vibration*, 215(1), 1998, pp. 17-34.
- [9] Gillich G.R., Tufoi M., Korca Z.I., Stanciu E., Petrica A., The Relations between Deflection, Stored Energy and Natural Frequencies, with Application in Damage Detection, *Romanian Journal of Acoustics and Vibration*, 13(2), 2016, pp. 87-93.

- [10] Praisach Z.I., Gillich G.R., Protocsil C., Muntean F., Evaluation of Crack Depth in Beams for known Damage Location based on Vibration Modes Analysis, *Applied Mechanics and Materials*, 430, 2013, pp. 90-94.
- [11] Gillich G.R., Praisach Z.I., Iancu V., Furdul H., Negru I., Natural Frequency Changes due to Severe Corrosion in Metallic Structures, *Strojniški vestnik - Journal of Mechanical Engineering*, 61(12), 2015, pp. 721-730.
- [12] Gillich G.R., Maia N., Mituletu I.C., Tufoi M., Iancu V., Korca Z., A new approach for severity estimation of transversal cracks in multi-layered beams, *Latin American Journal of Solids and Structures*, 13(8), 2016, pp. 1526-1544.
- [13] Negru I., Praisach Z.I., Gillich G.R., Vasile O., About the Neutral Axis Distortion due to Cracks and its Influence upon the Beams Natural Frequencies, *Romanian Journal of Acoustics and Vibration*, 12(1), 2015, pp. 35-38.
- [14] Gillich G.R., Praisach Z.I., Modal identification and damage detection in beam-like structures using the power spectrum and time-frequency analysis, *Signal Processing*, 96, 2014, pp. 29-44.

Addresses:

- PhD student Marius-Vasile Pop, Babeş-Bolyai University, Faculty of Engineering, Piaţa Traian Vuia, nr. 1-4, 320085, Reşiţa, marius.pop@student.uem.ro
- Prof. Dr. Eng. Gilbert-Rainer Gillich, Babeş-Bolyai University, Faculty of Engineering, Piaţa Traian Vuia, nr. 1-4, 320085, Reşiţa, gr.gillich@uem.ro (* *corresponding author*)
- PhD student Cristian Tufisi, Babeş-Bolyai University, Faculty of Engineering, Piaţa Traian Vuia, nr. 1-4, 320085, Reşiţa, cristiantufisi@yahoo.com
- Dr. Eng. Zeno-Iosif Praisach, Babeş-Bolyai University, Faculty of Engineering, Piaţa Traian Vuia, nr. 1-4, 320085, Reşiţa, zpraisach@yahoo.com
- Eng. Lucian Păun, Babeş-Bolyai University, Faculty of Engineering, Piaţa Traian Vuia, nr. 1-4, 320085, Reşiţa, lucian.paun@student.uem.ro

Deflection of a beam with a transverse crack under dead load

Marius-Vasile Pop, Zeno-Iosif Praisach, Gilbert-Rainer Gillich*,
Lucian Păun

This paper proposes an analytic relation for the deflection of a cantilever beam with a transverse crack subjected to dead load. The mathematical relation is deduced involving the decreased capacity of the beam to store energy, which is in direct relation with the crack position and depth. Eventually, the validity of the relation is proved by means of the finite element method.

Keywords: *cantilever beam, deflection, dead load, transverse crack*

1. Introduction

Cantilever beams are subject of dead weights and operational loads. Mathematical relations to calculate the free end deflection of such structures with constant cross-section [1]-[3] and even for the tapered beams [4] are known. The deflection is calculated by considering the distribution of the bending moment along the beam, respectively the equivalent bending moment for the tapered beams. An estimation of the deflection of stepped beams can be made involving relations proposed in [5]-[6], but the results accuracy is affected by the disturbance of the state of stress in the region where the cross-section changes suddenly [7]. The bigger the cross-section decrease, the bigger the error in estimating the free end deflection. The real deflection for stepped beams is always bigger as the calculation because a region of the beam in the proximity of the sudden cross-section increase or decrease does not contribute to the stiffness of the beam. Thus, from calculus, we always obtain an under-evaluated deflection.

As far as we know, there is no relation that allows calculating the deflection of a cantilever beam with transverse cracks. In this paper we propose a relation to calculate the deflection of a cantilever beam with a transverse crack, when the load consists of dead weight. The energy method is considered and a severity coefficient, similar to that found for the case of vibrating beams [8] is used. We prove by

means of the finite element method (FEM) that the proposed mathematical relation provides accurate results.

2. Analytical approach

The analysis is performed for a clamped beam (fig. 1) loaded with its own weight $p = \rho Ag$ [N/m], where g [m/s²] is the earth gravity. The beam is made of structural steel with density ρ [kg/m³], Young modulus E [N/m²] and having length L [m]. The beam is of rectangular section having area $A = bh$ [m²] and moment of inertia I_U [m⁴]. Under the action of its own mass, the maximum deflection of the beam at the free end is d [m].

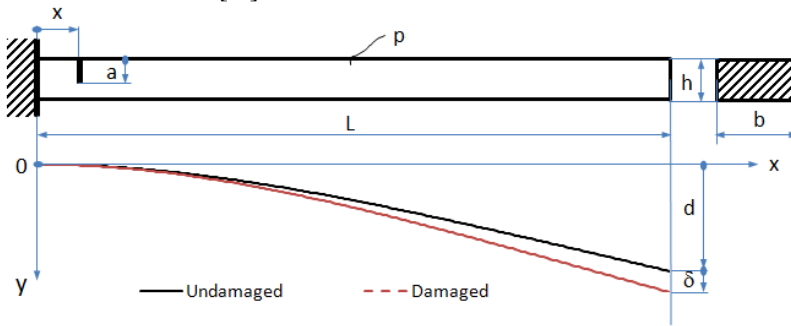


Figure 1. Clamped beam with transversal damage at the fixed end

From the strength of the materials it is known that the deflection at the free end of the beam can be determined with the relation:

$$d = \frac{pL^4}{8EI_U} \quad (1)$$

and the moment of inertia from relation (1) becomes:

$$I_U = \frac{pL^4}{8Ed} \quad (2)$$

Let's considering a crack near de clamped end (fig. 1) at the distance x [m]. The crack is along the whole width b [m] of the beam and has the depth a [m]. For this case, the moment of inertia of the equivalent beam (with reduced constant cross-section that exhibit the same free end deflection as the damaged beam) becomes I_{ech} [m⁴], and, consequently, the deflection of the beam with a crack can be written as:

$$d + \delta = \frac{\rho L^4}{8EI_{ech}} \quad (3)$$

From relation (3), the moment of inertia of the damaged beam becomes:

$$I_{ech} = \frac{\rho L^4}{8E(d + \delta)} \quad (4)$$

It is known that the fundamental natural frequencies of the beam with constant cross-section is computed with the relation:

$$f_U = \frac{\lambda^2}{2\pi} \sqrt{\frac{EI_U}{\rho AL^4}} = \frac{\lambda^2}{2\pi} \sqrt{\frac{E \frac{\rho L^4}{8Ed}}{\rho AL^4}} = \frac{\lambda^2}{2\pi} \sqrt{\frac{g}{8d}} \quad (5)$$

where, λ is the dimensionless wave number for the first vibration mode.

Taking into consideration relations (5) and (4), the natural frequency for the beam with a crack is:

$$f_D = \frac{\lambda^2}{2\pi} \sqrt{\frac{EI_{ech}}{\rho AL^4}} = \frac{\lambda^2}{2\pi} \sqrt{\frac{E \frac{\rho L^4}{8E(d + \delta)}}{\rho AL^4}} = \frac{\lambda^2}{2\pi} \sqrt{\frac{g}{8(d + \delta)}} \quad (6)$$

By dividing f_D to f_U it will be obtained:

$$\frac{f_D}{f_U} = \sqrt{\frac{d}{d + \delta}} \quad (7)$$

From the literature it is known that [9]:

$$\frac{f_D}{f_U} = 1 - \gamma(\bar{a}) \cdot [\bar{\phi}''(\bar{x})]^2 \quad (8)$$

In the relation (8), we denote with $\gamma(\bar{a})$ the severity of the crack that has the relative depth $\bar{a} = a/h$. We consider two beams, both having $h/L=1/200$, and the edges of the cross-section in the relation $h/b=1$ and $h/b=0.1$, respectively. The severity, according to [10], is:

$$\gamma(\bar{a}) = 0.4464(\bar{a})^4 - 0.2483(\bar{a})^3 + 0.1376(\bar{a})^2 - 0.0037(\bar{a}) \quad (9)$$

Alternatively, the values for the severity can be obtained from figure 2, by choosing the severity for a given damage depth [11].

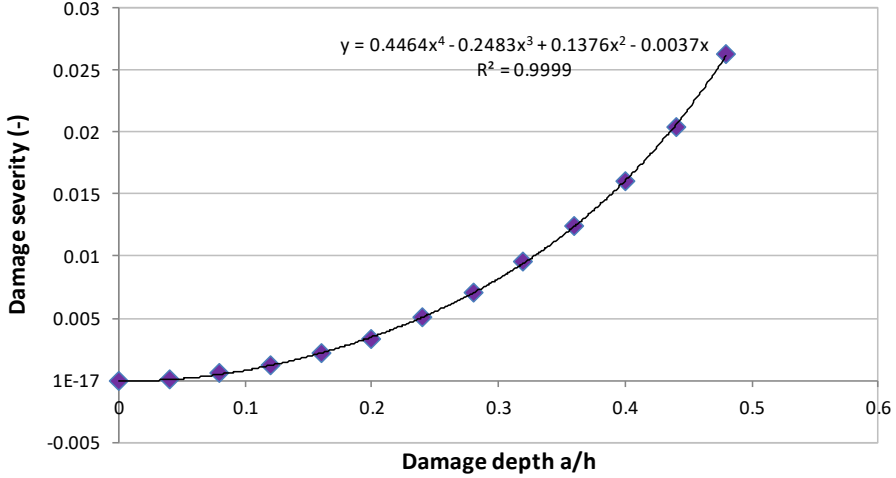


Figure 2. Values for the severity when the deep of the crack is between 0 and 0.5

One can observe in figure 2 that the severity does not depend on the dimensions of the rectangular cross-section of the beam, i.e. the ratio h/b .

The second term in the right part of relation (8), namely $\bar{\phi}''(\bar{x})$, represents the normalized bending moment or the normalized beam curvature at the normalized distance $\bar{x} = x/L$. The bending moment is calculated as the second derivative of the vibration mode shape of the beam. For the clamped beam, it is:

$$\bar{\phi}''(x) = \frac{1}{2} \left(\cos(\lambda x) + \cosh(\lambda x) - \frac{\cos(\lambda) + \cosh(\lambda)}{\sin(\lambda) + \sinh(\lambda)} [\sin(\lambda x) + \sinh(\lambda x)] \right) \quad (10)$$

From the mathematical relations (7) and (8), which both reflect the frequency ratio f_D/f_U , the deflection of the beam with a transverse crack results in:

$$(d + \delta) = \frac{1}{\left\{ 1 - \gamma(\bar{a}) [\bar{\phi}''(x)]^2 \right\}^2} \cdot d = \kappa \cdot d \quad (11)$$

Denoting the fraction in the right part of relation (11) as κ , and replacing the deflection of the beam with constant cross-section d with its expression defined in relation (1), we obtain the deflection of the cracked beam:

$$(d + \delta) = \frac{1}{\left\{ 1 - \gamma(\bar{a}) [\bar{\phi}''(x)]^2 \right\}^2} d = \kappa \cdot d = \kappa \frac{pL^4}{8EI_U} \quad (12)$$

We represent in figure 3 the evolution of the coefficient κ for two cases of the crack depth: $a/h=0.25$ and $a/h=0.50$. The crack is relocated along the whole length of the beam $x \in (0, L)$.

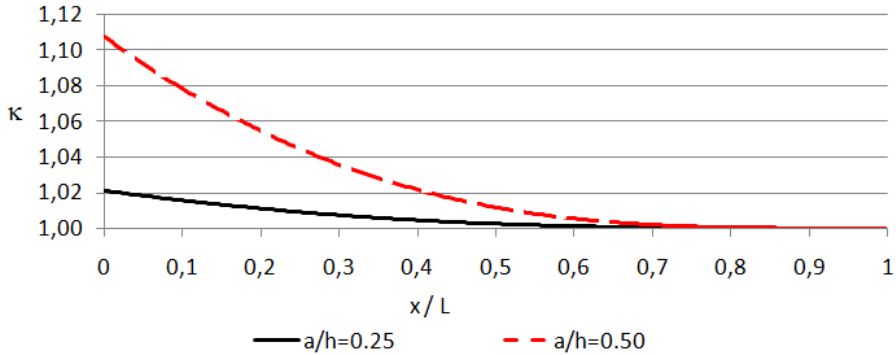


Figure 3. Deflection coefficient for $a/h=0.25$ and $a/h=0.50$ when crack is moving along the whole length of the beam

One can observe from figure 3 that the coefficient κ equals the unit at the free end of the beam. The proportionality between the amplitudes of the two curves, imposed by the crack depth is obvious.

3. Experimental research

In this section we prove that relation (12) derived for the deflection of a cracked beam works. To this aim, we involve the FEM and perform simulations for the beam with a uniform cross-section that has the dimensions and mechanical properties given in table 1.

Table 1. Properties of the beam with a uniform cross-section

Length L [mm]	Width b [mm]	Thickness h [mm]	Young modulus E [N/m ²]	Density ρ [kg/m ³]
1000	50	5	2×10^{11}	7850

The damaged beam has the same geometry as the healthy beam, but cracks with different positions and depths. The damage scenarios are described in table 2. For all cases, the crack width is $w=0.04$ mm. The analysis is performed with the ANSYS software, the beam getting a mesh with the maximum edge of the hexahedral elements 2 mm. In consequence, the beam with a constant cross-section is discretized with 37500 elements and 193282 nodes.

For the beams with discontinuities, the number of elements and nodes increase because around the discontinuity the mesh needs to be finer in order to make the transition from the constant cross-section to the reduced cross-section. The finest mesh is generated at the top of the crack.

Table 2. Damage scenarios

Scenario no.	Crack depth a [mm]	Crack position x [mm]	Curvature ϕ	Severity γ	Coefficient κ
S1	0.5	150	0.79377	0.000802	1.001011
S2	0.5	290	0.60417	0.000802	1.000586
S3	0.5	470	0.37493	0.000802	1.000225
S4	1	150	0.79377	0.003492	1.004414
S5	1	290	0.60417	0.003492	1.002554
S6	1	470	0.37493	0.003492	1.000982
S7	1.5	150	0.79377	0.008186	1.010395
S8	1.5	290	0.60417	0.008186	1.006002
S9	1.5	470	0.37493	0.008186	1.002305

In table 3, we compare the deflection obtained directly from Fem simulation with those calculated involving the deflection of the beam with uniform cross-section multiplied with the coefficient κ . One can observe in the mentioned table that the differences are extremely small, the error being less than 0.1%. even if the deflection increase is not big at all.

Table 3. Deflection achieved by calculus and simulation

Scenario no.	FEM	Calculus		FEM	Error ε [%]
	Deflection d [mm]	Coefficient κ	Deflection $d+\delta$ [mm]	Deflection $d+\delta$ [mm]	
S1	22.948	1.001011	22.97122	22.969	0.009662
S2	22.948	1.000586	22.96145	22.95959	0.008077
S3	22.948	1.000225	22.95318	22.95256	0.002671
S4	22.948	1.004414	23.04931	23.03289	0.071239
S5	22.948	1.002554	23.00661	22.99679	0.042704
S6	22.948	1.000982	22.97054	22.96793	0.011376
S7	22.948	1.010395	23.18656	23.14839	0.164593
S8	22.948	1.006002	23.08575	23.06658	0.083044
S9	22.948	1.002305	23.0009	22.99626	0.020181

An overview of the results presented in table 3 is given in figure 4. One can again observe the good fit of the results achieved by simulation and calculus.

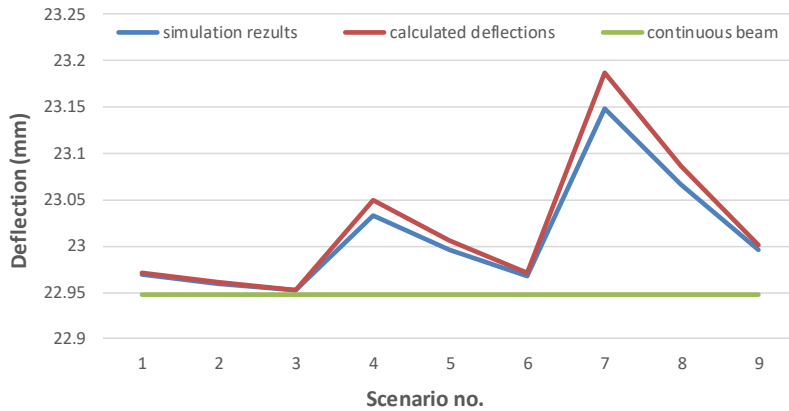


Figure 4. Deflection of the beam for the considered damage scenarios

Since we considered numerous damage scenarios, chosen randomly, for which the calculated deflections fit these obtained by simulation, we can conclude that relation (12) is precise and can be used to determine the deflection of cracks with discontinuities. Note that, this mathematical relation base on the capacity of the cracked beam to store energy, but does not use the equivalent bending moment [12] because the interval on which the cross-section is reduced is zero or infinitesimally small.

4. Conclusion

We introduce a mathematical relation to calculate the deflection of cantilever beams discontinuities of the cross-section under dead load. The relation involves a severity coefficient deduced for the crack at the fixed end, which is adjusted with the local effect when it is located elsewhere. The local effect considers the bending moment at the crack location, which is proportional with the energy stored at that location. Further research will focus on extending the theory to beams that have cross-sections with a different shape, and will also consider the cases of the beams with other support types and/or multiple cracks.

References

- [1] Bejan M., *Rezistența materialelor 2*, Editura AGIR, Bucuresti, 2009.
- [2] Udeyo F., *Structural Analysis*, California State University Affordable Learning Solutions Program, available at [https://eng.libretexts.org/Bookshelves/Civil_Engineering/Book%3A_Structural_Analysis_\(Udeoyo\)](https://eng.libretexts.org/Bookshelves/Civil_Engineering/Book%3A_Structural_Analysis_(Udeoyo))
- [3] Engineering ToolBox, *Cantilever Beams - Moments and Deflections*, available at: https://www.engineeringtoolbox.com/cantilever-beams-d_1848.html.

- [4] Babeu T., *Teoria elementara a rezistentei materialelor*, Editura Mirton, Timisoara, 1998.
- [5] Cheng P., Davila C., Hou G., Static, Vibration Analysis and Sensitivity Analysis of Stepped Beams Using Singularity Functions, *Journal of Structures*, Vol. 2014, Article ID 234085, 2014.
- [6] Gillich G.R., Praisach Z.I., Iancu V., Furdul H., Negru I., Natural Frequency Changes due to Severe Corrosion in Metallic Structures, *Strojniški vestnik - Journal of Mechanical Engineering*, 61(12), 2015, pp. 721-730.
- [7] Negru I., Praisach Z.I., Gillich G.R., Vasile O., About the Neutral Axis Distortion due to Cracks and its Influence upon the Beams Natural Frequencies, *Romanian Journal of Acoustics and Vibration*, 12(1), 2015, pp. 35-38.
- [8] Gillich G.R., Tufoi M., Korka Z.I., Stanciu E., Petrica A., The Relations between Deflection, Stored Energy and Natural Frequencies, with Application in Damage Detection, *Romanian Journal of Acoustics and Vibration*, 13(2), 2016, pp. 87-93.
- [9] Gillich G.R., Praisach Z.I., Modal identification and damage detection in beam-like structures using the power spectrum and time-frequency analysis, *Signal Processing*, 96, 2014, pp. 29-44.
- [10] Praisach Z.I., Gillich G.R., Protocsil C., Muntean F., Evaluation of Crack Depth in Beams for known Damage Location based on Vibration Modes Analysis, *Applied Mechanics and Materials*, 430, 2013, pp. 90-94.
- [11] Gillich G.R., Praisach Z.I., Detection and Quantitative Assessment of Damages in Beam Structures using Frequency and Stiffness Changes, *Key Engineering Materials*, 569-570, 2013, pp. 1013-1020.
- [12] Tripa P., *Rezistentă materialelor - Solicitari simple și teoria elasticității*, Editura Mirton, Timisoara, 1999.

Addresses:

- PhD student Marius-Vasile Pop, Babeș-Bolyai University, Faculty of Engineering, Piața Traian Vuia, nr. 1-4, 320085, Reșița, marius.pop@student.uem.ro
- Dr. Eng. Zeno-Iosif Praisach, Babeș-Bolyai University, Faculty of Engineering, Piața Traian Vuia, nr. 1-4, 320085, Reșița, zpraisach@yahoo.com
- Prof. Dr. Eng. Gilbert-Rainer Gillich, Babeș-Bolyai University, Faculty of Engineering, Piața Traian Vuia, nr. 1-4, 320085, Reșița, gr.gillich@uem.ro
(* *corresponding author*)
- Eng. Lucian Păun, “Eftimie Murgu” University of Reșița, Piața Traian Vuia, nr. 1-4, 320085, Reșița, lucian.paun@student.uem.ro

Prediction of power cables failures using a software application

Marius Florian Preduş, Elisabeta Spunei*, Monica Roşu

This paper analyses the electrical performance of power supply cables in operation by investigating previous faults and forecasting faults using the Easyfit Professional 5.6 software program. The calculation of the maximum operating time until the first fault occurs is based on an algorithm for estimating the parameters entered in the application, respectively the intervals of good operation time between two successive faults. The case study presented in the paper analyses the probability of failure of a medium voltage power line, under the administration of a distribution operator, based on information collected during maintenance work on medium and low voltage installations in the analysed area.

Keywords: prediction, cables, failure, software

1. Introduction

During operation, an electrical system is subjected to a series of factors of a mechanical, electrical, thermal, atmospheric natural, etc., which can cause defects. The analysis of the causes of the defects, the determination of the solutions to reduce them, the estimation of the time until the next defect, respectively the improvement of the system performances, constitute the main objectives of the increase of the reliability [1], [2], [3].

Very often, the defects of the power supply cables determine the non-observance of the quality conditions regarding the supply of the consumers [4], [5].

In practice, the determination of reliability is based on the application of probability theory, considering both the history of defects prior to the monitoring period and that of the defects during the monitoring period.

This complex analysis is currently carried out on the basis of specific mathematical models [2], [3] which take into account the mechanical, electrical, thermal and environmental requirements to which electrical systems are subjected during operation.

In the case of electricity cables, mathematical models evaluate the electrical performance by monitoring the number of faults, information that is usually obtained from electricity suppliers.

In order to prevent reliability calculation errors and reduce the analysis time, which requires a large workload, the prediction of faults in the power cables is currently made by using software programs dedicated to forecasting [1], [2], [3]. These software programs have the advantage of processing a large number of input variables, speed and accuracy in calculation, along with a user-friendly interface, which makes it easy to use ed qualified personnel in the field.

2. Brief description of the EasyFit Profesional 5.6 software

EasyFit Profesional 5.6 is a data analysis and simulation software program, used successfully in many fields of activity, including electrical engineering, in order to determine the probability of failure, and to ensure the safe operation of electrical systems [6], [7]. This simulation software is open-source and can be used in various applications. Based on the input data, which represents the period of the analysed defects, the software application allows framing the probability distributions in order to sample them, select the best model and use the results in order to find solutions to ensure prevention activities.

The software is designed by Mathware Technologies based on an algorithm meant for estimating the input variables entered in the calculation, starting from the experimental data and selecting the distribution that best suits them. The lesson is made from the 55 distributions of continuous and discrete functions in the library as its own [7].

Probability function histograms can be displayed simultaneously on a single chart for comparison. The main histograms displayed are [3]: the graph of the reliability function $S(x)$; the graph of the cumulative (defective) distribution function $F(x)$ - CDF; probability density graph $f(x)$ - PDF; Graph of failure intensity $h(x)$; the graph of the cumulative risk function $H(x)$.

The use of the software program involves the following steps:

- entering the data in a table similar to the tables in Excel;
- selecting the button that chooses the appropriate distribution;
- reading and interpreting the results processed based on the algorithm.

The choice of a distribution law appropriate to each situation is based on the existence of a correlation between the mathematical model used and the experimental results obtained from the measurements performed on the monitored system, .in a certain time interval.

In the event of defects due to fatigue (degradation) over time, a situation often encountered in power supply cables, it is recommended to use Weibull's law of distribution, also called cumulative distribution function, with mathematical expression:

$$F(t) = 1 - e^{-\left(\frac{t}{\beta}\right)^\alpha} \quad (0 \leq t \leq +\infty) \quad (1)$$

where α is the shape parameter by which the degradation level is indicated and β is the characteristic position or life parameter.

In the case of the three-parametric Weibull function, the parameter y is also introduced, which is a scale parameter, and the mathematical expression is:

$$F(t) = 1 - e^{-\left(\frac{t-y}{\beta}\right)^\alpha} \quad (2)$$

3. Case Study - Estimating the maximum operating time based on the operating times between two faults

The supply of electricity to domestic consumers is achieved through TP (transformation points) substations and UEL (underground power lines) or AEL (aerial power lines). Ensuring continuity in the supply of electricity to consumers is a quality condition that must be respected. Thus, special attention must be paid to the number of defects in consumer power cords. The number of faults is carefully monitored based on the history of events, in order to analyse the causes of failure and to establish their duration of operation between two faults [7], [8], [9]

The case study presented is performed on a 20 kV SLE, posed between two substations, noted in the paper TP 1 and TP PT 2, with an approximate length of 450 m. The electric cable is part of the medium voltage distribution network -one, administered by an electricity distribution operator [10].

Data on the number of events, causes of failure, as well as periods of malfunction between faults, were collected on the basis of test reports (BI), issued after defects were detected and remedied [10]. These test bubbles contain information about the measured values of the R_{iz} insulation resistances, the I_c conduction currents, as well as how to repair the defect. All this information formed the basis of the construction of the event data table (Table 1).

Table 1. Event at UEL 20kV (TP 1 →TP 2), cable type: NA2XS2Y, 3x1x150 mm², l=~450 m

Date of defect occurrence acc.to BI	Cause of failure	Remarks
Report no. 182/20.07.2015	- T-phase defect (insulation breakthrough) at 247 m from PT 1	- High humidity in PT 1; -Phase T-sleeve was performed at the fault location and R, S, T phases were tested with increased voltage;

Date of defect occurrence acc.to BI	Cause of failure	Remarks
Report no. 235/ 07.10.2015	- Defective phase R (insulation breakthrough) at 200 m from PT 1 - Defective terminal heads in PT 1	- Defects were remedied by slewing the R phase at the fault site and replacing the end heads in cell MT-PT 1;
Report no. 97/ 19.06.2016	Defective phase T (insulation breakthrough) at 3 m from PT 1	- The value of R_{ins} , I_c asymmetry of the phases calculated after remediation of the defect did not fall within the allowed limits;
Report no. 99/ 22.06.2016	Defective phase T (pierced sleeve) at 250 m from PT 1	- The value of the R_{ins} , I_c asymmetry of the phases calculated after the defect was remedied did not fall within the allowed limits;
Report no. 154/ 09.08.2016	Phase R fault (insulation breakthrough) at 300 m from PT 1	- After mounting the sleeve, the tests were performed with increased voltage and the UEL was re-powered.;
Report no. 161/ 20.08.2016	T-phase defect (pierced sleeve) at 180 m from PT 1	- After replacing the sleeve and testing with increased, the UEL was re-energized;
Report no. 23/ 23.02.2017	- T-phase defect (insulation overflow on a 1 m section) at 230 m PT 1; - Defective terminal heads in PT1.	- The cable insulation was restored by mounting two sleeves and 2 m of cable -High degree of humidity in the 20 kV cell of PT 1;

The analysis of the data in Table 1 showed the following periods of good operation:

- 20.07.2015 ÷ 07.10.2015 = 79 days;
- 07.10.2015 ÷ 19.06.2016 = 256 days;
- 19.06.2016 ÷ 22.06.2016 = 3 days;
- 22.06.2016 ÷ 09.08.2016 = 48 days;
- 09.08.2016 ÷ 20.08.2016 = 11 days;
- 20.08.2016 ÷ 23.02.2017 = 187 days.

The time intervals, calculated in days, were entered in the data table of the "EasyFit" calculation software (Fig.1). After entering the data, the calculation software indicated the bi-parametric "Lognormal" and "Weibull" functions as the most appropriate distributions. (Fig.2).

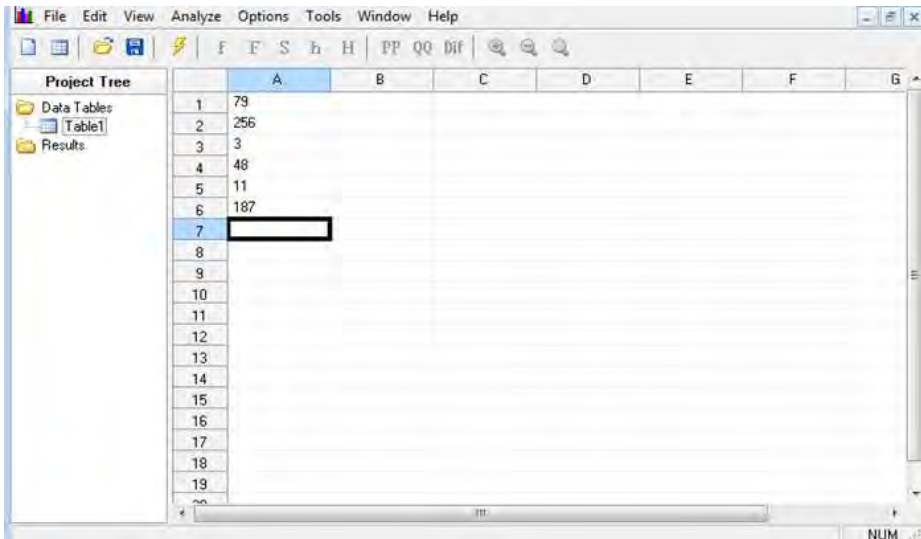


Figure 1. Operating times between two faults introduced in the program

By overlapping the graphs of the function $f(x)$, small differences of the variation curves of the two distributions were observed and the "Weibull" distribution was chosen, which is the most appropriate in the estimates of the entities where effects of some phenomena of wear or aging, as in the case of power cables [3], [5], [6], [7].

The calculated percentage values (Fig.2) indicate for operating days of 100 days, a probability of failure of 70.1%, a relatively high value given the relatively short time interval. For longer time intervals, the probability of failure increases substantially, reaching 82.6% and 88.6% for operating times of 200 and 300 days, respectively.

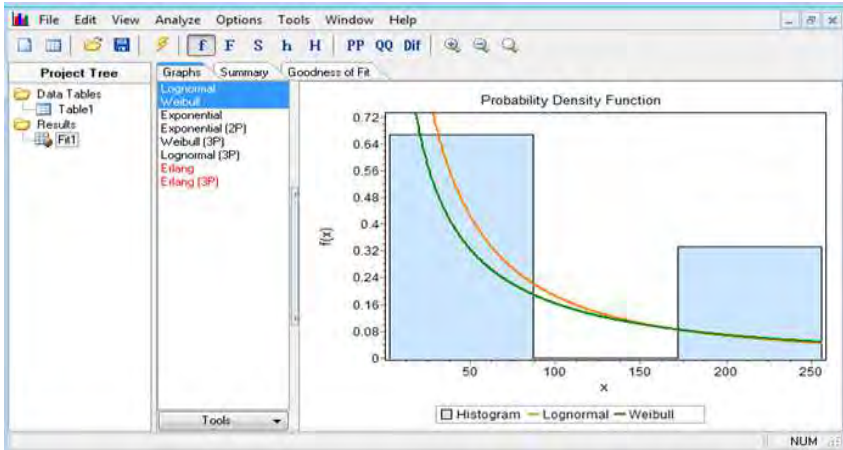


Figure 2. Automatic selection of the best distributions

The calculated percentage values (Fig. 3) indicate for operating days of 100 days, a probability of failure of 70.1%, a relatively high value given the relatively short time interval. For longer time intervals, the probability of failure increases substantially, reaching 82.6% and 88.6%, respectively, for operating times of 200 and 300 days (Fig. 4 and Fig. 5).

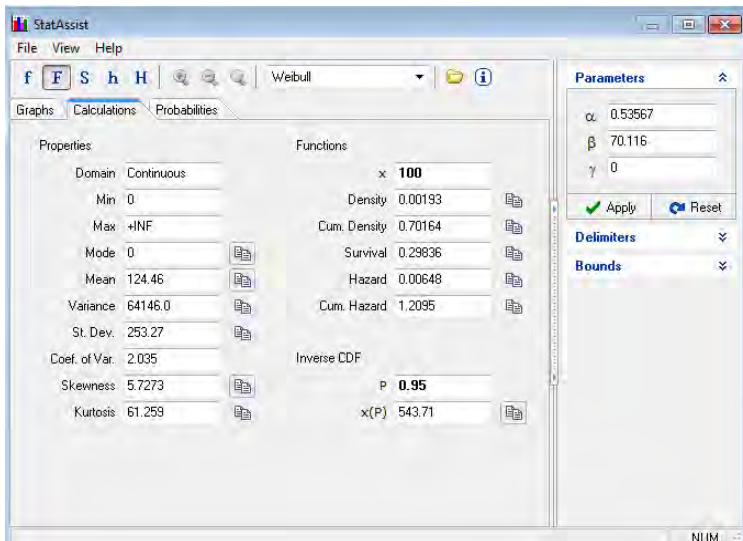


Figure 3. Calculation of the probability of failure and operation over a period of 100 days

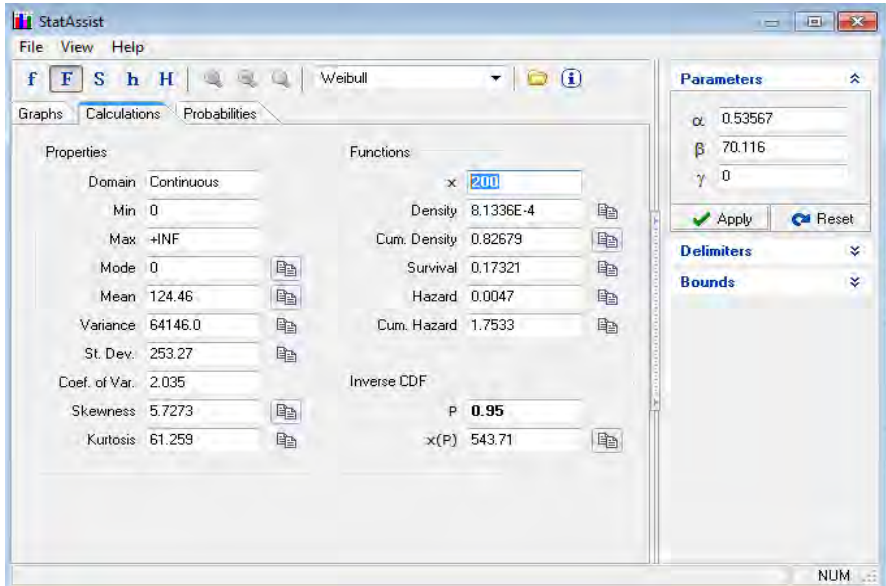


Figure 4. Calculation of the probability of failure and operation over a period of 200 days

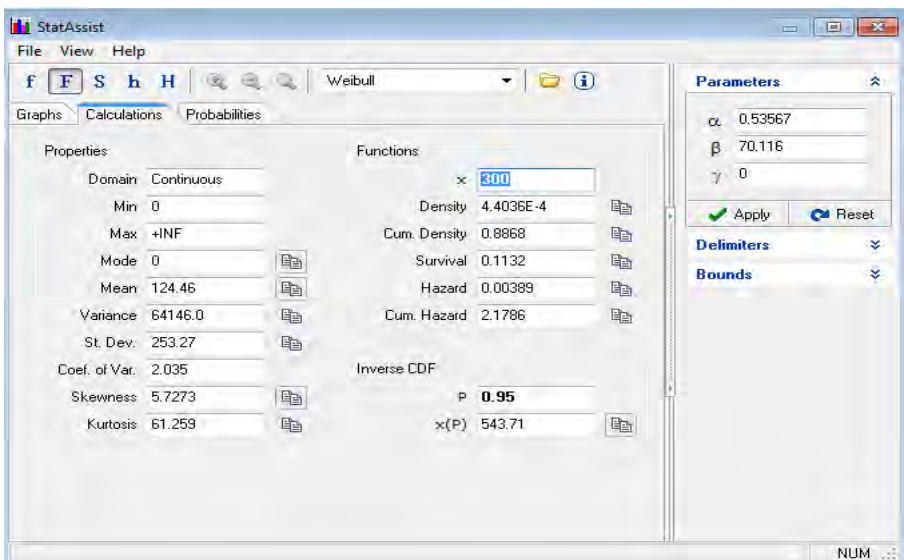


Figure 5. Calculation of the probability of failure and operation over a period of 300 days

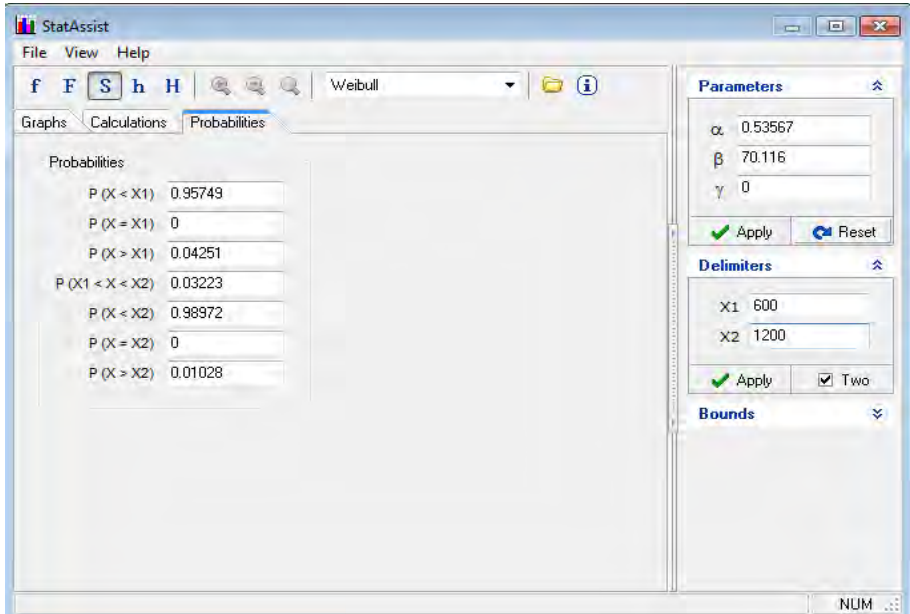


Figure 6. Calculation of the probability of failure and operation within 600 ÷ 1200 days

The probability of failure and that of operation were also calculated for longer time intervals: $X1 = 600$ days, and $X2 = 1200$ days, respectively. The probability of failure is for the range $X1$ of 95.74%, for $X2$ of 98.97% respectively. Thus it turns out that the probability of trouble-free operation for the $X2$ range is about 1%, which is very small. The obtained results are presented in Figs. 6.

3. Conclusions

The validation of the accuracy of the results obtained by simulation was made by comparing them with the real statistics of the failures [8], resulting from the incidents produced in the exploitation of the analysed SLE. The analysis concluded the following conclusions:

- The cable operated without interruption for 198 days, between 23.02.2017-09.09.2017 (BI no.231 / 09.09.2017), failing within 200 days, for which the probability of failure predicted by calculation was approximately 83%;
- The following incident took place after a period of 286 days (maximum duration of operation of the cable in operation from the moment of monitoring), on 22.06.2018 (BI no.130 / 22.06.2018), so within the interval of 300 days, for which the calculated probability of failure was 89%;

- For all the analysed cases a value higher than 0.53 resulted for the coefficient α , which indicates that there is a serious degradation of the cable, and the coefficient β had a value higher than 70, which suggests that the moral wear of cable is quite accentuated;

- From the analysis of the events presented, one can remark that the real incidents took place after time intervals for which the calculated failure probability was higher than 80%, validating the correctness of the simulations.

It results that the use of EasyFit Professional 5.6. it is a useful method of estimating the service life of power cables between two faults and allows in operation, allowing to establish the opportune moment regarding the replacement of morally used cables. Thus, due to the low operational reliability of the LES 12 / 20kV cable, it has been completely replaced with a new cable, in order to avoid the high maintenance costs that would have resulted and the interruption of electrical consumers.

References

- [1] Munteanu T., Gurguiatu G., Bălănuță C., *Fiabilitate și calitate în ingineria electrică: Aplicații*, Galati University Press, 2009.
- [2] Ciobanu L., *Fiabilitate, diagnoză și elemente de calimetrie*, Editura Universitatea Tehnica "Gheorghe Asachi" Iași, 2015.
- [3] Panaite V., Popescu M.O., *Calitatea produselor și fiabilitate*, Editura Matrixrom, București.
- [4] Preduș M.F., Spunei E., Piroi I., A Study on Failure Diagnosis Methods in Power Cables and Their Applications, *International Conference on Applied and Theoretical Electricity (ICATE)*, Craiova, 6-8 Oct. 2016.
- [5] Preduș M.F., Spunei E., Roșu M., Diagnostic of Defects at Electric Lines in Cable, *Proceedings of the 10th International Conference on Electromechanical and Power Systems SIELMEN 2015*, Chișinău, 8-9 Oct., 2015.
- [6] Popescu M.O., Popescu C.L., Gheorghe S., Ghiță C., Sisteme expert pentru diagnoza echipamentelor electrice, *Editura Electra*, București, 2002.
- [7] <https://www.mathwave.com> EasyFit Profesional 5.6.- Analysis and simulation software
- [8] Termoelectrica S.A, NTE 004/05/00 - Normativ pentru analiza si evidenta evenimentelor accidentale din instalatiile de productie, transport si distributie a energiei electrice si termice.
- [9] Sărăcin C.G., *Instalații electrice*, Editura Matrixrom, București, 2009.
- [10] EEI - Electroechipament Industrial Reșița - Executarea lucrărilor de mentenanță la instalațiile de medie și joasă tensiune, 2013-2020.

Addresses:

- Drd. Eng. Marius Florian Preduş, University Politehnica of Bucharest, Faculty of Electrical Engineering, Splaiul Independentei, nr. 313, sector 6, Bucureşti, code 060042, marius.predus@eei.ro
- Ş.l. Dr. Eng. Elisabeta Spunei, Babeş-Bolyai University, Faculty of Engineering, Piaţa Traian Vuia, nr. 1-4, 320085, Reşiţa, e.spunei@uem.ro
(* *corresponding author*)
- Lect. Dr. Monica Roşu, Babeş-Bolyai University, Piaţa Traian Vuia, nr. 1-4, 320085, Reşiţa, m.roşu@uem.ro

Model of microprocessor centrifugal equipment for honey extraction

Eugen Răduca, Mihaela Molnar*, Nicolae Titu Fara

The paper presents a model of centrifugal equipment for extracting honey made around an ATmega 328 processor, with which the Arduino Uno module is equipped. The created model is functional, being tested, and the practical results obtained would allow the transition to prototype equipment. The created model is flexible, allowing to obtain flexible operating cycles, with variable speeds, soft settable, in both directions of rotation. The number of frames from which the bee honey can be extracted is variable depending on the juicer itself, which is driven by the motor.

Keywords: *model, extraction, honey, microprocessor*

1. Introduction

Honey is a natural product of honey bees, with remarkable properties, recognized and certified, used both in direct feed and in other areas of human importance, such as: food industry, curative medicine, aesthetic medicine, etc.

Honey is a bee product obtained by processing and processing nectar by bees and stored in honeycomb cells to feed the hive population. Obtaining honey is the main purpose of beekeeping today and in the past. Depending on the origin, the honey can be:

Flower honey - it is also called floral honey, which is made by bees by processing nectar and pollen from flowers;

Manna honey - also called extra floral honey or forest honey, is made from other substances derived from plants (sap from the leaves of trees such as pine, spruce or oak). It is darker in colour than flower honey, having strong antiseptic properties.

After the flowers from which the nectar was collected, in our country it is obtained:

Acacia honey; Linden honey; Rapeseed honey; Sunflower honey; Polyfloral honey (sometimes also called wildflower honey).

Regardless of the origin of the honey, it can be extracted by several techniques: Extraction of honeycomb pieces; Free flow from the honeycomb; Extraction by centrifugation; Honeycomb pressing; Melting honeycombs with honey.

Of these techniques, centrifugal extraction is the most widely used due to its advantages.

Extraction of honey, using centrifugal force, involves the introduction of honeycomb frames into a container of equipment, which rotates in both directions, with controlled speed and duration, depending on the characteristics of honey and environmental conditions (temperature). The rotation of the container can be done mechanically, manually, through a reducer, or electrically, using a drive motor. The container in which the honeycombs are deposited is usually made of stainless steel. In the container can be deposited 3-4 honeycombs with honey. The honeycombs in the hive have different sizes being in accordance with the type of hive used by the beekeeper. Depending on how the combs are positioned in the container, it can be radial or tangential. In Figure.1 are given two industrially produced equipments.



Figure 1. Industrially produced honey extraction equipment
a) manual b) electric

2. Model of microprocessor centrifugal equipment for bee extract

2.1. Block diagram of the model made

The block diagram of the equipment designed and made practically (of the model) is given in Figure 2, being composed of the following blocks:

BAI - Power supply unit

BCC - Command and control block

BAC - Drive block

BAf - Display block

REM - Honey extractor container

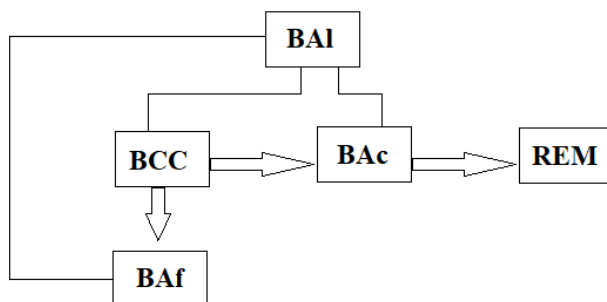


Figure 2. Block diagram of the model made

2.1.1. Power supply unit

The equipment is supplied in single phase from the national electricity network. In essence, the power supply is composed of a low-voltage transformer with several secondary windings that supply the voltages, subsequently rectified and filtered [1] used for the command and control, actuation and display blocks, respectively.

2.1.2. Command and control block

The command and control block is implemented with an Arduino Uno card [2], having as central unit the ATmega 328 P processor, is given in Figure 3. The program based on which the necessary functions and commands are performed is presented in [3], and the meaning of the Arduino Uno card pins this module is connected to the other blocks in the equipment is given in Figure.4, details being presented in [4].

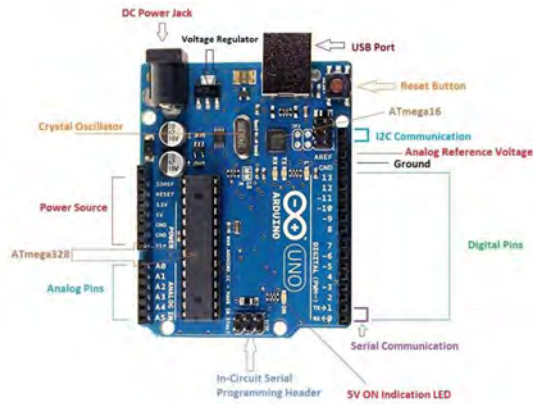


Figure 3. Arduino Uno card

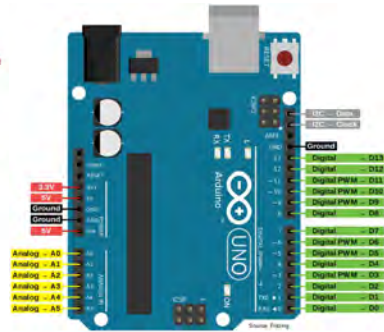


Figure 4. Arduino Uno card pins

2.1.3. Drive block

The drive block is a direct current unit having as load a direct current motor coupled to the vertical axis of the honey extractor container.

The drive block has variable voltage up to 30V, current up to 15 A and 400 W power for DC power supply is obtained through a PWM module (Figure.5) compatible with the Arduino system, equipped with two MOS transistors type BA7U2 [5].

The polarity change at the terminals of the DC motor is done by a module containing two independent relays (Figure.6), provided with protection diodes connected in antiparallel with the coils that can be controlled by optocouplers, for galvanic isolation from the control device (Arduino Uno board). Since the coils are supplied via a control circuit, the mode needs a supply voltage for it (5V). The actuation of a relay is signalled by the lighting of the corresponding LED.

Each relay has a normally closed contact (NC) and a normally open contact (NO) with respect to the common point (COM) and by properly connecting them in the circuit the reversal of the polarity of the supply voltage of the electric motor is obtained. Only one relay will be ordered for each direction of rotation [6].

Given the 400 W power at the output of the PWM module and the current on the 10A relay contacts, no changes in the wiring diagram are required when operating a normal-sized container, except for the DC motor to be chosen according to the load on which must drive it (normal size container).



Figure 5. PWM module



Figure 6. Two-relay module

2.1.4. Display block

An LCD1602 [7] display is used to display the messages generated by the Arduino Uno card, referring to the state of the installation according to the stages of the program installed in the memory (Figure 7). The adaptation between the Arduino Uno card and the display [8] is done through the I2C adapter module (Figure 8).



Figure 7. Display type LCD1602



Figure 8. I2C LCD1602 adapter

2.1.5. Honey extractor container

The radial honey extractor container, for 4 frames, is made of sheet metal on a small scale of 5: 1, and can be seen in Figure 9.



Figure 9. Model of centrifuge container made

2.2. Model of centrifugal equipment with microprocessor for bee honey extract made

The realized model is in Figure.10, where it can be observed that on a support plate are arranged the modules indicated in block diagrams from Figure.2. In addition, a series of clamps for connections between blocks can be seen. The electric DC drive motor is not directly visible as it is located under the extractor container.



Figure 10. Model of centrifugal equipment with microprocessor for bee honey extract made

3. Tests and experiments

Given the existing experience in the field as well as the experience of the authors, it was established that the proposed model should carry out the process of extracting honey in three stages: in the first and third stage it rotates directly for 15 seconds and in the stage of the second centrifuge rotates counter clockwise for 20 seconds. As specified the speed can be adjusted in each of the 3 stages.

The maximum measured speeds obtained were 144 rpm for the direct rotation situation and 180 rpm for the reverse engine rotation.

4. Conclusions

The model will be used to make a 1: 1 scale installation, when a larger container driven by a suitable power motor will be used.

Instead of the container for 4 radial frames, one for 3 frames or a tangential extraction container can be used. Of course, if the type of container used is replaced, its maximum rotational speeds will be adjusted, the change being more significant only when switching: radial type - tangential type.

The mechanical reducer, used in the case of manual juicers, can be removed. The equipment is flexible, programmable and does not significantly charge the cost price compared to an existing electric extractors. The equipment has the technical characteristics in accordance with the legislative ones.

References

- [1] Răduca E., *Electronică aplicativă*, Editura Orizonturi Universitare, Timisoara, 2010.
- [2] <https://www.theengineeringprojects.com/wp-content/uploads/2018/06/Introduction-to-Arduino-UNO.jpg> (downloaded at 2020).
- [3] Fara N.T., *Model de automatizare a unei centrifuge de stors miere*, Dissertation Paper, “Eftimie Murgu” University of Reșița, 2020, pp. 44-50.
- [4] <https://diyi0t.com/arduino-uno-tutorial/> (downloaded at 2020).
- [5] https://ardushop.ro/2506-thickbox_default/modul-comutator-pwm-deputere.jpg (downloaded at 2020).
- [6] https://ardushop.ro/158-thickbox_default/modul-releu-2-canale.jpg (downloaded at 2020).
- [7] https://ardushop.ro/134-thickbox_default/lcd-1602.jpg (downloaded at 2020).
- [8] https://ardushop.ro/226-thickbox_default/modul-i2c.jpg (downloaded at 2020).

Addresses:

- Prof. Dr. Eng. Eugen Răduca, Babeş-Bolyai University, Faculty of Engineering, Piaţa Traian Vuia, nr. 1-4, 320085, Reşiţa, e.raduca@uem.ro
- Assist. Prof. Dr. Eng. Mihaela Molnar, Babeş-Bolyai University, Faculty of Engineering, Piaţa Traian Vuia, nr. 1-4, 320085, Reşiţa, m.molnar@uem.ro
(* *corresponding author*)
- Eng. Nicolae Titu Fara, TMK Reşiţa, Str. Lalescu Traian, 36, Resita, fara.nicolaetitu@yahoo.com

Technical performance analysis of a 40 kW photovoltaic installation

Elisabeta Spunei*, Ion Piroi, Florina Piroi

To reduce the consumption of classically produced electric energy, which is an important green gas pollution factor, various renewable energy sources are now implemented on larger and larger scale. Both industrial and household consumers make use of such renewable energy sources. This work presents the characteristics and performance of a 40 kW photovoltaic installation mounted on the roof of an industrial production hall. The design and the implementation of the photovoltaic installation allows it to function while connected to the local power grid. On-site measurements have shown that the installation ensures symmetric voltages and currents, functioning at the planned parameters.

Keywords: *Photovoltaic installation, technical performances, measurements, efficiency, harmonics*

1. Introduction

Following the European directives [1] until 2020, 20% of the consumed energy in the European Union must come from renewable sources, with 10% used by the transport industry. By 2030, the current European directives [2] indicate that the at least 27% of the consumed energy must originate from renewable resources, with the goal of increasing this percentage to 32%.

Motivated by the mentioned European directives, quite a considerable number of projects have been started that focus on producing energy from renewable sources (solar, wind, hydraulic), with more and more certified energy producers. Thus, at the end of 2019, the National Energy Regulatory Authority (ANRE)¹ certified 573 economic entities with 635 energy production units in photovoltaic power

¹ Acronyms reflect the Romanian denominations.

plants. The installed capacity for these photovoltaic power plants is between 0,002 MW and 56.112 MW, while the total installed power was of 1.258.434 MW [3].

On September 5, 2020, at 1pm, we saw a record of photovoltaic energy produced by installations connected to the National Energetic System (SEN), the generated power of 774 MW representing 9,9% of the totally produced power in Romania at that time [4].

Figure 1 presents the energy production and consumption curves for a three-day period, from September 4 to September 6, 2020, where the maximum of electrical power produced by photovoltaic power plants can be observed.

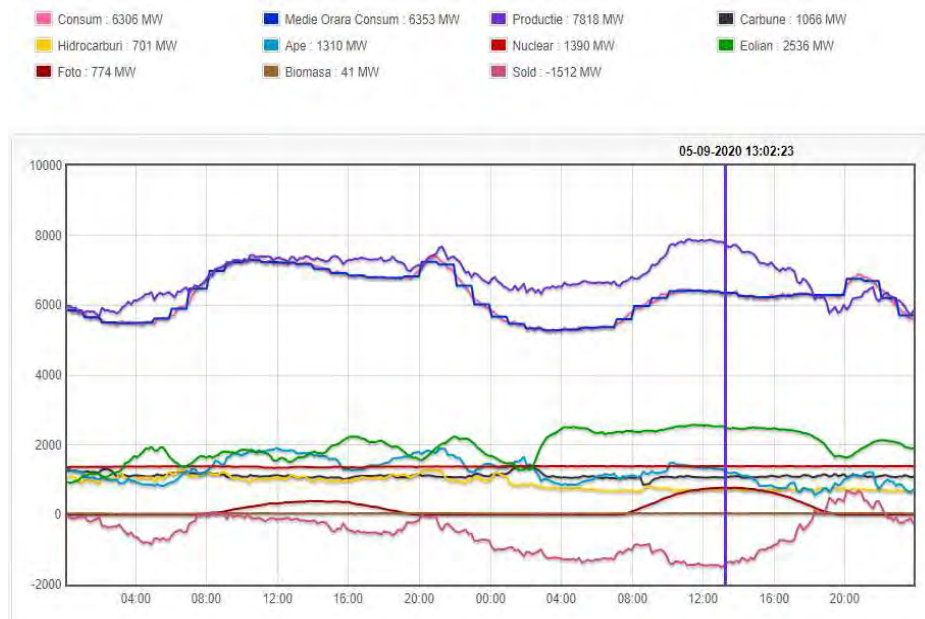


Figure 1. Electricity production and consumption curves [4]

We find in the literature various studies and applications where photovoltaic installations are used to power various consumers, including industrial and transportation consumers [5-9].

Various operational programs and funding granted by the Romanian Ministry of Environment support companies and individuals in their efforts to invest in the production of photovoltaic energy. In this context larger numbers of investors and individuals have assembled such photovoltaic installations and mounted them on buildings, becoming energy producers, either connected to the National Energetic System or operating in islands.

In this work we present our analysis of a 40 kW photovoltaic power plant. We look at the voltage and current waveforms, at the harmonic and distortion levels, and at the installation's capacity to supply the necessary energy.

2. Technical Details of the Studied Photovoltaic Installation

The 40 kW photovoltaic plant we analyse in this work has 160 photovoltaic panels of 270 W, two invertors, a Smart Power Sensor, measurement instruments, connecting appliances, and protective installations.

The photovoltaic installation schema the most important element is the MPPT solar controller (Maximum Power Point Tracking) which plays a critical role in obtaining the maximum power out of the solar energy, and the efficient use of the panels.

The technical characteristics of the photovoltaic panel are presented in [10].

Figure 2 presents the current variation curves depending on voltages, for the various incident radiations. The figure also marks the maximum power values P_{mpp} .

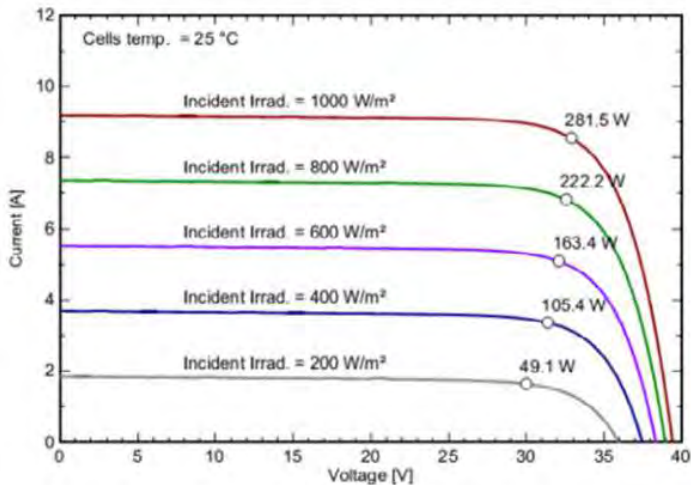


Figure 2. Current-Voltage variation curves [10].

Further, for the same $1,000 W/m^2$ incident radiation, we find different maximum power values, depending on the photovoltaic cell temperatures (Figure 3). We see that the optimal cell temperature should be of $25^\circ C$, which requires a cell cooling installation in the days with high temperatures.

The 160 panels installed on an industrial hall roof are divided into two groups, 80 for each inverter. In turn, the 80 panels in each group are arranged into four rows of 20 panels. The 8 ends of the rows are connected with safeties to a direct current box switch.

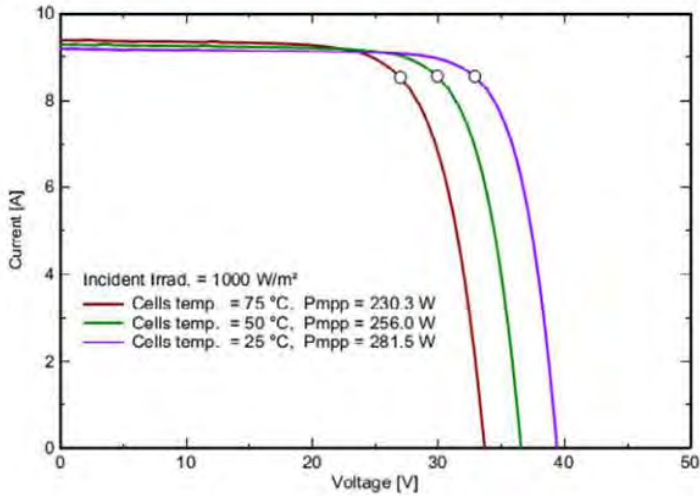


Figure 3. Current-Voltage curves for different photovoltaic cell temperature values [10].

The main technical parameters of the analysed invertors are presented in [11]. We present in Figure 4 the connection schema for the two invertors, connection that is realised by self-synchronisation.

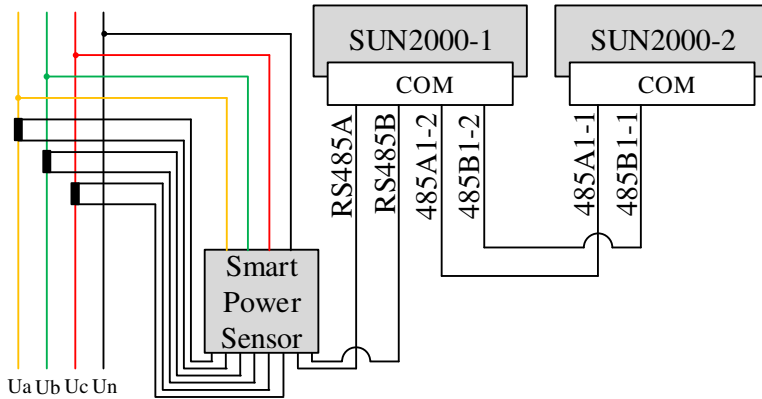


Figure 4. Invertor connection to the grid schema

The schema in Figure 4 makes clear that the invertors can only connect to the power grid when the Smart Power Sensor detects the grid voltage and sends impulses to synchronize the invertors with the power network. This is advantageous

to the installation as it allows the photovoltaic installation to avoid an insular functioning as well as eliminating the possibility of supplying with energy appliances that do not belong to the installation's owner.

3. Testing the Photovoltaic Installation

We describe here the measurements taken during February 2020, after 15:00 when the illumination levels were above 20.000 lx. We measured surface luminancies, obtaining the following values:

- $L_s = 3.200 \text{ cd/m}^2$, at ground level, on light grey pavels;
- $L_{th} = 2.554 \text{ cd/m}^2$, on the industrial hall metal sheet, with a shiny light grey coating;
- $L_{ta} = 906,6 \text{ cd/m}^2$, on the blue metal sheet adjacent to the photovoltaic panel;
- $L_{PV} = 697,4 \text{ cd/m}^2$, on the panel's dark surface.

Considering that the incident radiation on the photovoltaic panels has the same values as on the ground level, we obtain the panels' reflection coefficient, k_r :

$$k_r = \frac{L_s - L_{PV}}{L_s} \cdot 100 \quad [\%] \quad (1)$$

That is:

$$k_r = \frac{3200 - 698}{3200} \cdot 100 \cong 78 \quad [\%] \quad (2)$$

The panels' absorption coefficient, k_a , for the time of the measurements was:

$$k_a = 1 - k_r = 22 \quad [\%] \quad (3)$$

We also measured:

- The power supplied by the photovoltaic power plant (Figure 5): 14,25 kW;
- The reactive power: 0,13 kVAR;
- The apparent output: 14,25 kVA;
- The power factor: 1;
- Frequency: 50,01 Hz.
- The circuit voltages supplied by the installation's inverters, connected to the power grid, have almost the same values, and have a sinusoidal shape (Figure 6);
- The currents on the three phases, from the inverter to the network are almost equal in values, and have a sinusoidal shape (Figure 7);
- The Total Harmonic Distortions of each phase's currents and voltages (Figure 8).



Figure 5. Measured power and power factor values for the photovoltaic installation

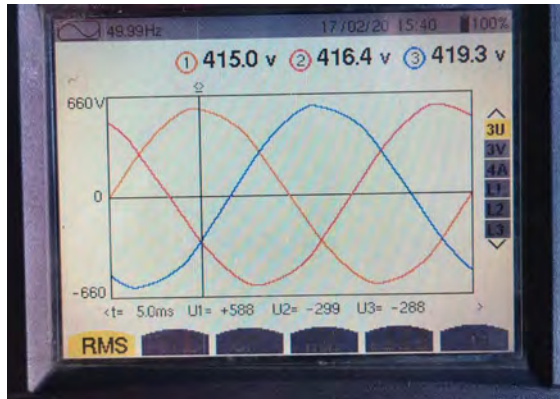


Figure 6. Circuit voltages for the photovoltaic installation



Figure 7. Current values on the three phases

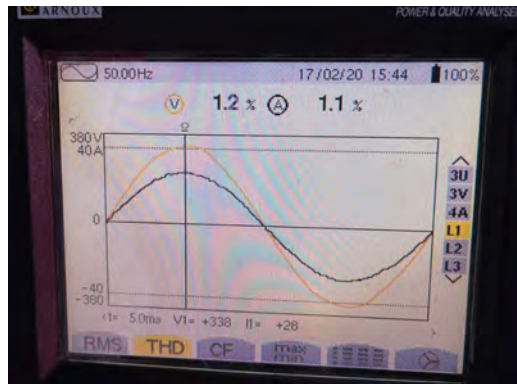


Figure 8. Voltage and Current superior harmonics

4. Conclusion

Although the solar radiation did not have maximum values during the measurement taking, the power supplied by the photovoltaic installation represented 35,63%. The current and voltage wave shapes are very close to a sinusoidal shape, the amount of superior harmonics being very low (1,2%):

The panels' positioning angle is of 10% to the ground, which is too low. We recommend, therefore, that the panels are position at an approximately 35° from the horizontal. For an increased efficiency, we see the need of a sun tracking system. Furthermore, to allow the use of the produced energy also during the night, it is needed to install a batteries storage system.

As the consumer's installed capacity is of 140 kW while the photovoltaic installation supplied power is of 40 kW, the photovoltaic panels can only ensure a 28,7% of the necessary electric energy. The company that has installed the photovoltaic panels, however, owns three further industrial halls, on each of which further photovoltaic panels are to be installed. If this happens, the consumer will become energy independent, as the installed capacity of the enlarged photovoltaic system will surpass the consumer's installed power.

References

- [1] Directive 2009/28/EC of the European Parliament and of the Council of 23 April 2009 on the promotion of the use of energy from renewable sources and amending and subsequently repealing Directives 2001/77/EC and 2003/30/EC eur-lex.europa.eu/legal-content/RO/TXT/PDF/?uri=CELEX:32009L0028 (accessed 07.09.2020).

- [2] Directive (UE) 2018/2001 of the European Parliament and of the Council of 11 December 2018 on the promotion of the use of energy from renewable sources (recast), (accessed la 07.09.2020), eur-lex.europa.eu/legal-content/EN/TXT/PDF/?uri=CELEX:32018L2001.
- [3] List of certified producers and of power plants producing energy from renewable sources. Last updated on 31 December 2019, (accessed 07.09.2020) www.anre.ro/download.php?f=fqZ/g6c=&t=vdeyut7dlcecrLbbvbY=.
- [4] Grafic producția, consumul și soldul SEN, (accessed 07.09.2020) www.transelectrica.ro/widget/web/tel/sen-grafic/-/SENGrafic_WAR_SENGraficportlet?display=APE
- [5] Spunei E., Protea B., Piroi I., Navrapescu V., Piroi F., Use of Renewable Energy Sources to Power Railroad Traffic Safety Installations, *11th International Symposium on Advanced Topics in Electrical Engineering (ATEE)*, Bucharest, Romania, Mar. 28-30, 2019.
- [6] D'Arco S., Piegari L., Tricoli P., Comparative Analysis of Topologies to Integrate Photovoltaic Sources in the Feeder Stations of AC Railways, *IEEE Transactions on Transportation Electrification*, 4(4), 2018, pp. 951-960.
- [7] Wu M.L., Wang W.Y., Deng W.L., Chen H.B., Dai C.H., Chen W.R., Back-to-Back PV Generation System for Electrified Railway and its Control Strategy, *IEEE Asia-Pacific Transportation Electrification Conference and Expo (ITEC Asia-Pacific)*, Harbin, Peoples R China, Aug. 7-10, 2017.
- [8] Lori L., Redi P., Ruzinsky M., Grid Connected Photovoltaic Supply Units for Railway Applications, *Fuji Electric Review*, 49(2), 2003, pp. 53-59.
- [9] Senda K., Makino Y., Application of Solar Cell Integrated Roofing Material at Railway Stations, *25th IEEE Photovoltaic Specialists Conference*, Washington, DC, May 13-17, 1996.
- [10] Altius, altius-solar.com/wp-content/uploads/2019/09/Policristalin-60celule-270W.pdf, (accessed la 07.09.2020)
- [11] Smart String Inverter, solar.huawei.com/en/download?p=-/media/Solar/Fattachment/pdf/eu/datasheet/SUN2000-12-20KTL-M0.pdf (accessed 07.09.2020).

Addresses:

- Ș.I. Dr. eng. Elisabeta Spunei, Babeș-Bolyai University, Faculty of Engineering, Piața Traian Vuia, nr. 1-4, 320085, Reșița, e.spunei@uem.ro (* corresponding author)
- Prof. Dr. Eng. Ion Piroi, Babeș-Bolyai University, Faculty of Engineering, Piața Traian Vuia, nr. 1-4, 320085, Reșița, i.piroi@uem.ro
- Tech. Dr. Florina Piroi, Technische Universität Wien, piroi@ifs.tuwien.ac.at

Virtual instrument designed for data acquisition

Mihaela Dorica Stroia, Cornel Hațiegan*, Cristinel Popescu

Current software development directions open up a world of possibilities, especially in the engineering field. Present paper is meant to highlight the advantages and in particular the ease of using virtual instrumentation facilities, with a proper and adequate design and implementation of desired instrument. In this idea we bring into discussion a design for virtual instrument which can be used for data acquisition that can be stored for further simulations according to the needs required by the process in discussion.

Keywords: *virtual, instrument, signal, acquisition*

1. Virtual instrument-architecture and functions.

The concept of Virtual Instrumentation was introduced about thirty years ago out of a desire to use the electronic computer for building a measuring instrument. Nowadays, virtual instrumentation is mainly used for complex applications, where simultaneous measurements at thousands of control points are required, or processing of a large amount of measurement information and access to remote information is imposed.

Development of digital instruments equipped with communication interfaces makes it possible to control real measuring instruments not only manually, but also by means of the computer. Various combinations of numerical, programmable, stand-alone, computer-controlled tools with different built-in tools can be used by using additional data acquisition cards and appropriate software [1, 4].

In order to communicate with the process subjected to parametric measurements, computer must be equipped with an additional hardware interface device which plays the role of converting input analog signal into output numerical signal on a certain number of bits, based on the analog-to-digital conversion [8, 12].

So, the hardware virtual instrument interface should include an analog to digital converter. In addition, the interface can contain multiplexers, amplifiers and sampling-data storage circuits [6].

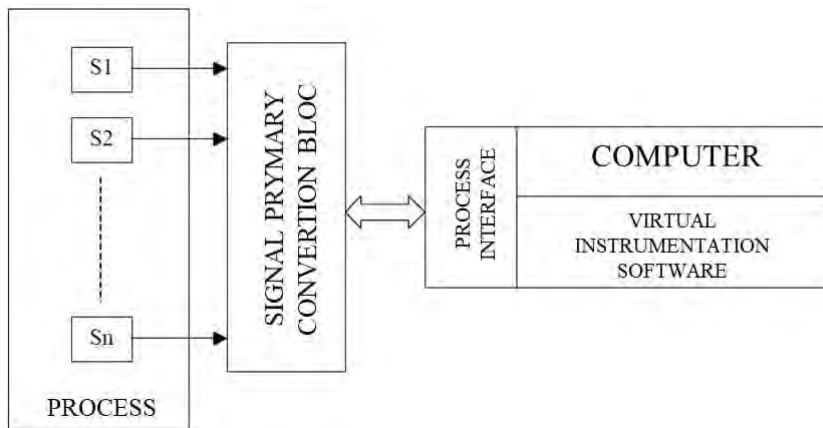


Figure 1. Basic structure of a virtual instrument

The data word transmission to the computer can be done either directly through the computer's bus, usually using DMA protocol, either through other serial and parallel communication interfaces. There is a wide range of devices on the market specialized in converting analog measurement quantities into digital signals such as: data acquisition cards, digitizers, built-in multi-meters, individual modules for distributed measurements, PXI type modules, etc. [5]. All are built with a greater or lesser autonomy in relation to computer, but all have common feature of converting analog signals from the real process, in particular those received from primary signal processing block, into digital signals, with the best possible accuracy [10].

Using digitized signals, the virtual instrumentation program controls and supervises the acquisition, processing, storage, display and remote transmission of measurement information, the software for making virtual instruments usually opting for graphical programming, easy to use. One of the basic functions that can be developed in the structure of a virtual instrument is automatic acquisition of signals obtained from sensors which carry electrical and non-electrical measuring quantities in a process, according to structure and configuration of an application [3, 7, 9].

2. Designing data acquisition virtual instrument

As earlier mentioned, a virtual instrument is the generic name used for simulating behavior of a measurement instrument or an automation, by means of a dedi-

cated software and specific hardware interface which contains signal processing modules and data acquisition boards. For designing and testing a data acquisition virtual instrument we used a well-known simulation software, LabView. As source signal we also used LabView facilities, generating a sinusoidal waveform by means of *Simulate Signal Sine* option. Measured data are recorded and saved on computer in specific files with *.lvm extension, thus data are available for further analysis. This tool is able to display in real time information about generated signal by the indicators, and in addition, it can simultaneously record signal data.

Figure 2 shows bloc diagram of virtual instrument used for data acquisition. the Simulate Signal Sine function is used to generate the sinusoidal signal. The simulated signal is transmitted to *Write to Measurement File* tool which, when running the program, will generate and save files to hard disk containing data measurements.

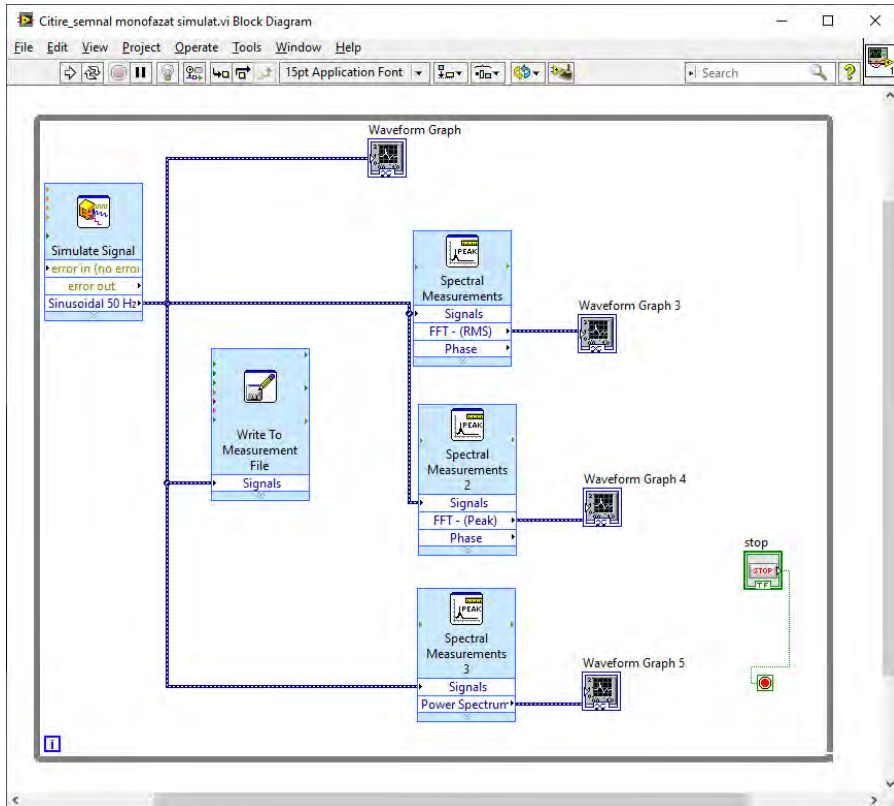


Figure 2. Bloc diagram of virtual instrument

File type, number of columns per channel, delimitation between columns, disk save path, and other characteristics of the files that will be generated and saved are defined in the *Write to Measurement File* tool window by selecting these parameters, as it can be seen in figure 3.

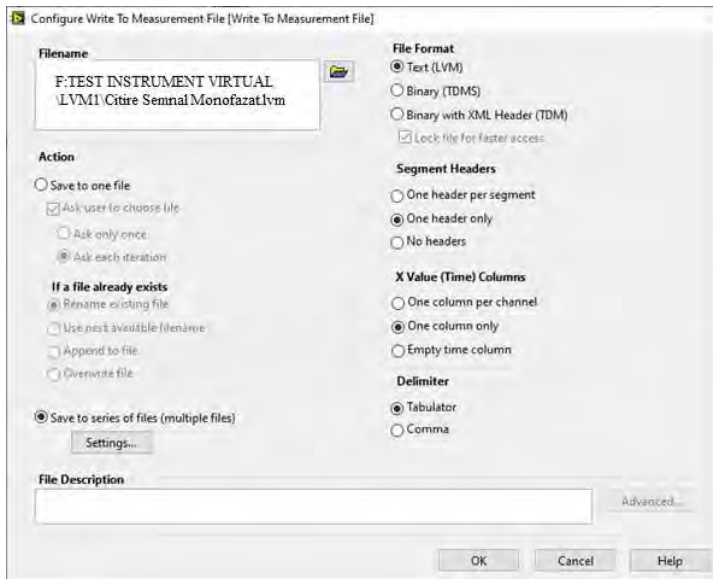


Figure 3. Parametric setup for generating data measurement files

The sinusoidal voltage signal is applied simultaneously to the Spectral Measurements instruments, which calculate and display in frequency range the average value (RMS), peak-to-peak value (Peak) and power spectrum of the simulated signal. These three values are displayed with the WaveForm Graph indicators 3, 4 and 5.

3. Simulating virtual instrument functioning and displaying results

After building up virtual instrument for data acquisition and setting up proper parametric values, front panel of the instrument will be used for simulation [11]. We have chosen two signals configured in *Simulate Signal* window: signal 1 with amplitude of 325, frequency of 50Hz and a phase Φ of 0° and signal 2 with amplitude of 20, frequency of 20Hz and a phase Φ of 0° .

The program is executed by pushing START button. While the program is running, * .lvm files containing discrete values of time on the X axis and discrete values of amplitude on the Y axis will be saved on the hard disk. The values are delimited

with tab and the files have been set not to exceed 3Kb [2]. Obtained results are presented in figure 4.

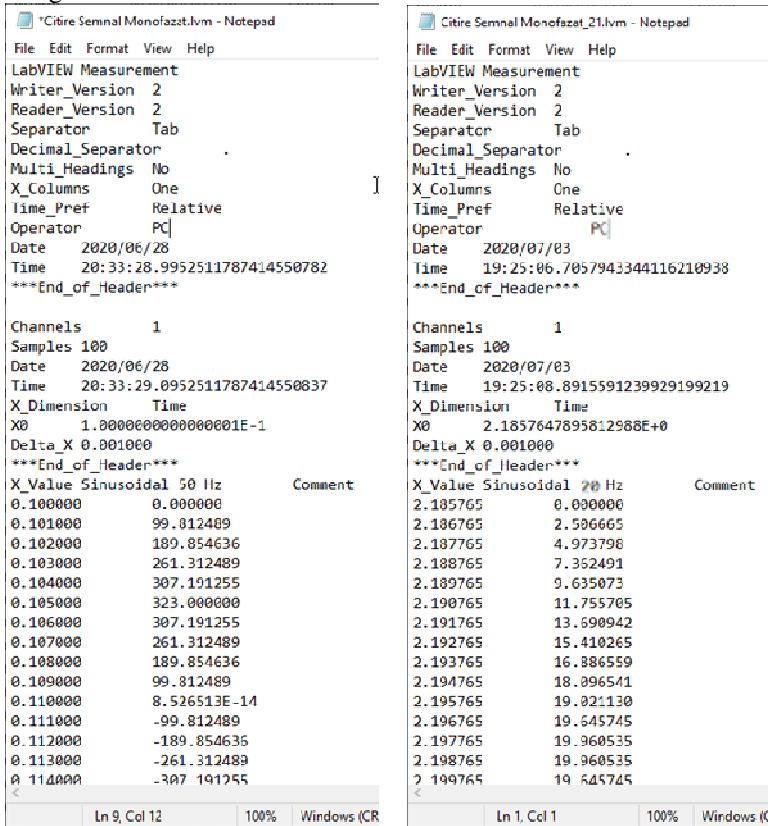


Figure 4. Generated files content for defined signals

Measured data saved in files can be further processed. By using control buttons we can vary the values of frequency, amplitude and phase for each signal, thus changing the peak values, averages and power spectrum of the sinusoidal signal. Using WaveForm Graph 3, 4 and 5 we can display RMS, PEAK and Power Spectrum and the waveform of the input sinusoidal signal. Results for simulated signals are depicted in figure 5 and 6.

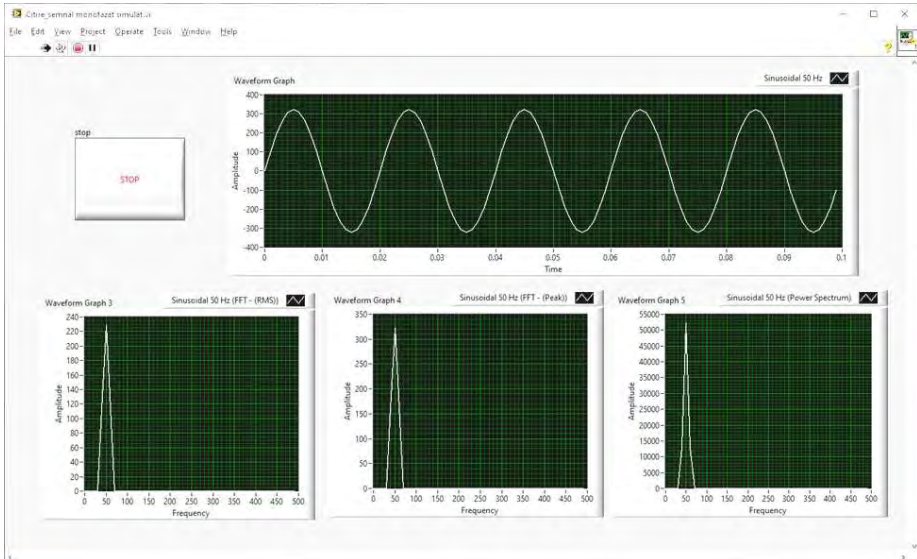


Figure 5. Simulation results for 50Hz frequency and 325 amplitude signal

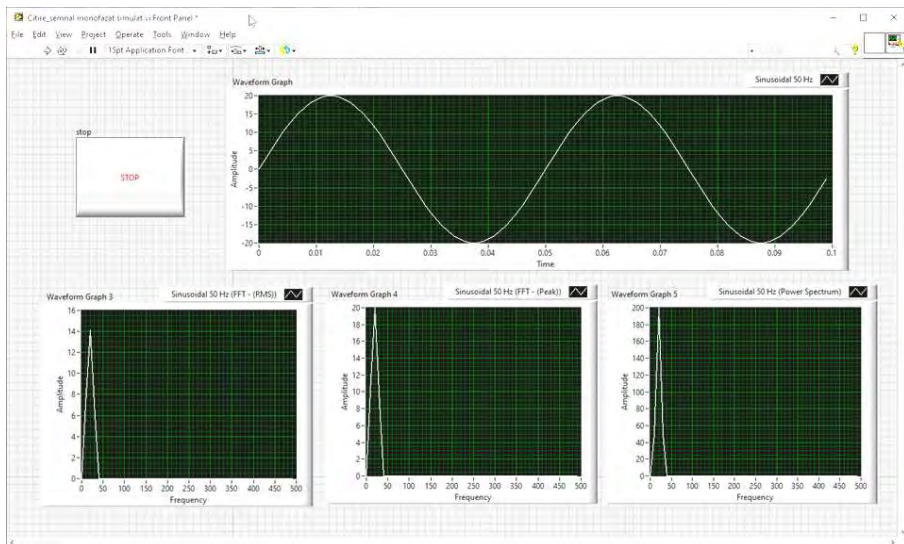


Figure 6. Simulation results for 20Hz frequency and 20 amplitude signal

4. Conclusion

Virtual instrument described in present paper is a basic tool designed for data acquisition. Due to a variety of advantages offered by virtual instrumentation, as expandability, high precision, flexibility, and the tools involved in this area we can extend designed instrument according to different applications which require data acquisition. For this case we generated data by means of virtual instrument but, with proper equipment, data can be saved in situ. However, latter solution has its disadvantages implying costs and frequency band limitations due to analog to digital conversion technology.

References

- [1] Stroia M.D., Derbac D., Hațiegan C., Cîndea L., Thermostat model with Arduino Uno board for controlling a cooling system, *Analele Universității "Constantin Brâncuși" din Târgu Jiu*, nov. 2018.
- [2] Kehtarnavaz N., *LabVIEW Graphical Programming Environment* - chapter 2, Digital Signal Processing System Design (Second Edition), Pag. 5-56, 2008.
- [3] Wang Lixin; Li Rongting, Design of engine test-bed experiment data acquisition system based on virtual instrument LabVIEW, *Journal of Hebei University of Science & Technology*, 35(2), pp. 109-117, 2014.
- [4] Tufoi M., Vela I., Marta C., Stroia M.D., Microcontroller's Application in Driving of Industrial Robots, *Analele Universitatii „Eftimie Murgu“ Resita, Fascicula de Inginerie*, 17(2), 2010.
- [5] Raduca E., Ungureanu-Anghel D., Pop N., Florea F., Raduca M., Hatiegan C., Ayaz Ahmad M., Determination of prime implicants of a logic function through the implementation of Quine McCluskey method in LabVIEW, *Advances in Environmental Biology*, 10(3) 2016, pp.186-191.
- [6] Ling Gang Liu, Jun Hui Li, Ling Gang Liu, Design of Data Acquisition System Based on LabVIEW, *Advanced Materials Research*, 569, 2012, pp. 808-813.
- [7] Shujiao Ji, Yanmin Lei, Wanli Zhang, *The design of data acquisition system based on virtual instrument*, Proceedings of 2nd International Conference on Computer Science and Network Technology, Dec. 29-31, Changchun, China, 2012.
- [8] Stroia M.D., Moșteanu D., Răduca E., Popescu C., Hațiegan C., *Case Studies for automotive components using CAD and CAE techniques*, International Conference on applied sciences, ICAS2019, May 9-11, 2019, Hunedoara, Romania.
- [9] Kun Yang, Chenguang Wu, Yixing Yuan, Jingyang Yu, *Application of Virtual Instrument Technique in Data Acquisition of Gas-Water Pulse Pipe Cleaning*

- Experiment*, Proceedings of 2nd International Congress on Computer Applications and Computational Science, 144, 2012, pp 465-470.
- [10] Quonan Ming Ji, Guo-ping Yang, *Design of remote data acquisition system for hydraulic impactor based on virtual instrument*, 3rd International Conference on Electronic Information Technology and Computer Engineering EITCE, 18-20 Oct., 2019, Xiamen, China.
- [11] Bigeng Zheng, Xinrui Chen, *Design of Multi-channel data acquisition system based on single Chip computer and LabVIEW*, Journal of Physics: Conference Series, CISAT 2019, 1345(6), 2019.
- [12] Stroia M.D., Anghel D., Moșteanu D.E., Hațiegan C., *Communication Interface Prototype Used for Data Transmission at Electric Systems*, International Conference Knowledge-Based Organization, 25(3), 2019, pp. 63-68.

Addresses:

- Lect. Dr. Eng. Mihaela Dorica Stroia, Babeș-Bolyai University, Faculty of Engineering, Piața Traian Vuia, nr. 1-4, 320085, Reșița, m.stroia@uem.ro
- Lect. Dr. Phiz. Cornel Hațiegan, Babeș-Bolyai University, Faculty of Engineering, Piața Traian Vuia, nr. 1-4, 320085, Reșița, c.hatiegan@uem.ro (* *corresponding author*)
- Assoc. Prof. Dr. Eng. Cristinel Popescu, University „Constantin Brâncuși” of Târgu-Jiu, Calea Eroilor, Nr.30, Târgu-Jiu, popescu.cristinel67@gmail.com